STUDY OF SULFIDE MINERALS OXIDATION SUPPRESSION USING SILICON-CATECHOL COMPLEX

ユニアティ, ムティア デウィ

https://doi.org/10.15017/1543962

STUDY OF SULFIDE MINERALS OXIDATION SUPPRESSION USING SILICON-CATECHOL COMPLEX

Mutia Dewi Yuniati

September 2015

STUDY OF SULFIDE MINERALS OXIDATION SUPPRESSION USING SILICON-CATECHOL COMPLEX

by

Mutia Dewi Yuniati

A thesis submitted to the
Department of Earth Resources Engineering
Graduate School of Engineering
Kyushu University
Fukuoka, Japan

As partial fulfillment of the requirements for the degree of
DOCTOR OF ENGINEERING

September 2015

Abstract

Acid mine drainage (AMD) resulting from the oxidation of pyrite and other sulfide minerals has caused significant environmental problems, including the acidification of rivers and streams, and the leaching of toxic metals. Once exposed to water and oxygen during mining and mineral processing, sulfide minerals become immediately susceptible to chemical and biochemical oxidation. Passivation of sulfide minerals involving formation of a surface barrier through formation of a coating layer is a potential way to control AMD generation.

In this study, the promising method of carrier microencapsulation (CME) using a silicon–catechol complex to suppress sulfide minerals oxidation was investigated. To reveal the mechanism and coating layer properties, dissolution tests, and morphological and electrochemical analyses were performed. In addition, samples were characterized by surface-sensitive X-ray photoelectron spectroscopy (XPS), atomic force microscopy (AFM), and dynamic force microscopy (DFM).

This thesis consists of six chapters. **Chapter 1** presents the background and objectives of this study. In addition, an overview of AMD and its prevention are presented to provide a basic understanding of pyrite oxidation suppression. Previous studies related to the present study are also discussed in this chapter.

In **Chapter 2**, pyrite oxidation suppression by CME with silicon (Si) and an organic carrier is presented. It was found that waste water collected from hydrothermal treatment (HT) of low-rank coal contains organic carbon compounds, such as phenol and catechol. The use of HT liquid (HTL) produced from low-rank coal as a carrier in CME was investigated. In dissolution tests for 51 days with pyrite and iron-oxidizing bacteria, treatment with a mixture of HTL and a silicon reagent (Si–HTL) lowered the ferric ion concentration and limited bacterial attachment compared with untreated pyrite. These results indicate that pyrite oxidation can be suppressed simply by pretreating with Si–HTL for 1 h. This might be caused by catechol present in the HTL. A mixture of catechol and a silicon reagent (Si–Cat) was also used, and the coatings obtained using Si–HTL and Si–Cat were compared. Based on dissolution tests, the Si–HTL coating layer showed better barrier properties than the Si–Cat coating layer. Microscopic observations showed a silica-rich deposit on the surface of the treated pyrite. Fourier-transform infrared (FTIR) spectroscopy indicated that a quinone compound adsorbed on the treated pyrite surface. These results showed that silica and quinone were both adsorbed on the pyrite surface in a silica–quinone layer, which can suppress pyrite oxidation.

In **Chapter 3**, three different electrochemical methods, namely, potential polarization, chronoamperometry, and electrochemical impedance spectroscopy (EIS), were used to investigate the electrochemical behavior of pyrite oxidation suppression in the presence of a silicate coating. Anodic current peaks corresponding to oxidative decomposition of the Si–Cat complex on the pyrite surface were observed at 550 mV in the presence of Si–Cat, and at 690 mV in the presence of Si–

HTL. The anodic currents of the treated pyrite samples (Si–Cat pyrite and Si–HTL pyrite) were lower than that of the untreated pyrite. Because the anodic current represents the oxidation rate, the lower anodic currents of the treated pyrite samples mean that the oxidation rates of these treated samples are lower than that of the untreated pyrite. The two flat semi-circular curves in the Nyquist plots showed that the total impedances of the treated pyrite samples increased. It is suggested that this is a silica–quinone coating, which can decrease the pyrite oxidation rate. It also showed that the coating resistance produced by Si–HTL treatment is higher than that produced by Si–Cat. Bode plots showed the shift of the phase angle of the time constant of Si–Cat-treated pyrite to lower frequencies, indicating electrolyte diffusion occurs through the coating layer. This indicates that the coating layer produced by Si–HTL treatment has better barrier properties than that produced by Si–Cat and confirms the results of the dissolution tests and chronoamperometric measurements.

In **Chapter 4**, a more systematic investigation of the silica–quinone coating layer is presented. Furthermore, the mechanism involved in this coating treatment is proposed. Pyrite treatment using Si–Cat under different conditions resulted in differences in the suppression of pyrite oxidation. The electrochemical behavior of treated pyrite samples showed that Si–Cat treatment for 6 h with initial pH 9.5 gave better barrier properties and a higher suppression effect than that of other treatment conditions. FTIR and XPS analyses demonstrated that the coating layers on the treated pyrite samples consisted of a network of Fe–O–Si and Si–O–Si units on the pyrite surface. The Si–O–C asymmetric stretching mode is also present in the FTIR spectra. These results confirm that silicate polymerization in the silica–quinone layer on the treated pyrite samples suppressed pyrite oxidation.

In **Chapter 5**, pyrite oxidation suppression by the Si–Cat complex was applied to other sulfide mineral samples: chalcopyrite ($CuFeS_2$), molybdenite (MoS_2), and arsenopyrite (FeAsS). Similar to pyrite, the results indicate the formation of a coating layer on the treated sulfide mineral samples that lowered the oxidation rate. The Si–Cat complex showed a better suppression effect for chalcopyrite than for molybdenite and arsenopyrite.

Chapter 6 summarizes the conclusions of this study and provides recommendations for further study.

List of Contents

Cover
Abstract i
List of Contents iii
List of Tables vi
List of Figures vii

Chapter 1
Introduction 1
1.1. Theoretical background 2
1.1.1. Acid mine drainage 2
1.1.2. Sulfide minerals 8
1.1.3. Pyrite 9
1.1.4. Mechanism and chemistry of pyrite oxidation 10
1.1.5. Acid mine drainage controlling methods 13
1.1.5.1. Flooding/sealing of underground mines 14
1.1.5.2. Underwater storage of mine tailings 15
1.1.5.3. Land-based storage in sealed waste heaps 15
1.1.5.4. Blending of mineral wastes 15
1.1.5.5. Total solidification of tailings 16
1.1.5.6. Application of anionic surfactants (Biocides) 16
1.1.5.7. Bioelectrochemical treatment 17
1.1.5.8. Microencapsulation 17
1.2. Objective of the thesis 21
1.3. Structure of the thesis 22
References 24

Chapter 2
Suppression of Pyrite Oxidation by Carrier Microencapsulation using Si–HTL and Si–Cat 32
2.1. Introduction 33
2.2 Materials and methods 34
2.2.1. Materials 34
2.2.1.1. Pyrite 34
2.2.1.2. Liquid product from hydrothermal treatment of LRC 36
2.2.2. Methods 37
2.2.2.1. Pretreatment of pyrite and dissolution tests 37

2.2.2.2. Surface characteristics of coating layer on pyrite 38
2.3 Results and discussion 39
2.3.1. Dissolution tests 39
2.3.2. Surface characteristics of coating layer on pyrite 45
2.4. Conclusions 51
References 52

Chapter 3
Electrochemical Behavior of Resultant Encapsulating Layer of Silicate Coating 55
3.1. Introduction 56
3.1.1. Potential polarization 57
3.1.2. Chronoamperometry 57
3.1.3. Electrochemical impedance spectroscopy 57
3.1.3.1. Circuit elements 60
3.1.3.2. Nyquist plot 62
3.1.3.3. Bode plot 64
3.1.3.4. EIS of coated metals 65
3.2. Material and methods 66
3.2.1. Material 66
3.2.2 Methods 67
3.3. Results and discussion 68
3.4 Conclusions 78
References 79

Chapter 4
Mechanism of Pyrite Oxidation Suppression using Silicon–catechol Complex 84
4.1. Introduction 85
4.2. Materials and methods 85
4.2.1. Materials 85
4.2.1.1. Pyrite 85
4.2.1.2. Si–Cat solution 87
4.2.2 Methods 87
4.2.2.1. Pretreatment of pyrite and electrochemical analysis 87
4.2.2.2 Pretreatment of pyrite and surface characteristics 88
4.3. Results and discussion 89
4.3.1. Effect of treatment time by silicate coating on pyrite oxidation suppression 89
4.3.2. Effect of pH in silicate coating on pyrite oxidation 91

suppression
4.4. Conclusions 107
References 108

Chapter 5
Application of a Silicate Coating on Chalcopyrite, Molybdenite, and Arsenopyrite 112
5.1. Introduction 113
5.2. Materials and methods 114
5.2.1. Materials 114
5.2.1.1. Chalcopyrite, molybdenite, and arsenopyrite 114
5.2.1.2. Si–Cat solution 115
5.2.2. Methods 115
5.2.2.1. Pretreatment of chalcopyrite, molybdenite, and arsenopyrite 115
5.2.2.2. Surface characteristics of coating layer on chalcopyrite, molybdenite, and arsenopyrite 116
5.2.2.3. Pretreatment and electrochemical analysis of chalcopyrite, molybdenite, and arsenopyrite. 116
5.3. Results and discussion 117
5.3.1. Surface characteristics of coating layer on chalcopyrite, molybdenite, and arsenopyrite 117
5.3.2. Electrochemical analysis 121
5.4. Conclusions 130
References 130

Chapter 6
Conclusions and Recommendations 133
6.1. Conclusions 134
6.2. Recommendations 137

Acknowledgments 139

List of Tables

Table 1.1.	Sources of acid mine drainage (Akcil and Koldas, 2006).	7
Table 2.1.	Elemental compositions of pyrite sample from Saimoku mine, determined using ICP-AES.	35
Table 2.2.	Proximate and ultimate analyses of Loy Yang Coal.	36
Table 2.3.	Concentrations of selected typical organic compounds in HTL of LRC, determined using GC-MS.	37
Table 2.4.	Average surface roughness calculated from Fig. 2.12.	50
Table 3.1.	Circuit elements	62
Table 3.2.	EC element parameters obtained by fitting experimental impedance data for untreated and treated pyrite samples with EC models shown in inset in Fig. 3.8.	74
Table 4.1.	Elemental compositions of pyrite sample from Victoria mine, determined using XRF.	86
Table 4.2.	EC element parameters obtained by fitting experimental impedance data for untreated and 6 h Si–Cat-treated pyrite samples with EC model shown in Fig. 4.4.	94
Table 4.3.	Comprehensive atomic allocation based on the measurement of narrow scan of Fe, S, O, and Si spectra of untreated and 6 h Si–Cat-treated pyrite samples.	104
Table 5.1.	Anodic currents of untreated and Si–Cat-treated sulfide minerals calculated from Fig. 5.5.	126
Table 5.2.	EC element parameters obtained by fitting experimental impedance data for untreated and Si–Cat-treated sulfide minerals with EC models shown in Fig. 5.7.	129

List of Figures

Figure 1.1.	AMD-affected water at Upper Daisy Creek, Montana (Reprinted from: USGS, 2014).	6
Figure 1.2.	The unit cell of pyrite FeS_2. Red atoms correspond to Fe^{2+} and grey ones to S_2^{2-}, respectively. Every iron ion is surrounded by six sulfur ions. S_2 dumb-bells are parallel with space diagonals. Sulfur ion has one S neighbour and three Fe neighbours (Reprintred from: Leiro et al., 2003).	10
Figure 1.3.	Schematic representation of some of the possible reactions describing different pathways for pyrite oxidation. To the right is the thiosulfate pathway (Path 1A) where thiosulfate detaches and reacts, while to the left is the thiosulfate pathway where the Fe-S bond does not break; rather the S-S bond breaks, releasing sulfite which oxidizes to sulfate (Path 1B). To the bottom of the figure we represent the sulfide-polysulfide-elemental sulfur pathway (Path 2) and at the top is the defect/photochemically-driven pathway where holes or radicals react and drive S oxidation to sulfate (Path 3) (Druschel and Borda, 2006).	12
Figure 1.4.	Schematic illustration of carrier microencapsulation using Si–Cat complex.	19
Figure 2.1.	XRD patterns of pyrite sample from Saimoku mine.	35
Figure 2.2	Changes in cells number with time.	40
Figure 2.3.	Changes in ferric ion concentration with time.	40
Figure 2.4.	Changes in total iron concentration with time.	41
Figure 2.5.	Changes in pH with time.	41
Figure 2.6.	Changes in ORP with time.	42
Figure 2.7.	SEM images of pyrite samples: (a) untreated pyrite/sterilized, (b) untreated pyrite/bacteria, (c) Si–Cat pyrite/bacteria, and (d) Si–HTL pyrite/bacteria.	44
Figure 2.8.	SEM-EDX element mapping of untreated pyrite.	45
Figure 2.9.	SEM-EDX element mapping of pyrite in presence of Si–Cat (Si–Cat pyrite).	45
Figure 2.10.	SEM-EDX element mapping of pyrite in presence of Si–HTL (Si–HTL pyrite).	46
Figure 2.11.	FTIR spectra of untreated and Si–Cat-treated pyrite samples.	48
Figure 2.12.	AFM images of untreated and Si–Cat pyrite.	49
Figure 2.13.	DFM (topography and phase) images of untreated and Si–Cat pyrite.	50

Figure 3.1.	Current response to a sinusoidal voltage input at a given frequency (Lvovich, 2012).	59
Figure 3.2.	Nyquist plot for $R\|\|C$ circuit showing impedance vector and other major features (Gamry Instrument).	63
Figure 3.3.	Nyquist plot for an ideal coating (Gamry Instrument).	64
Figure 3.4.	Bode plot of an ideal coating (Gamry Instrument).	65
Figure 3.5.	Equivalent circuit model for coated metal (Bonora et al., 1996).	65
Figure 3.6.	Polarization curves of pyrite electrode in silicate and/or catechol solution: (a) Si–Cat addition, and (b) Si–HTL addition.	69
Figure 3.7.	Chronoamperometric curves of untreated pyrite, Si–Cat pyrite, and Si–HTL pyrite in 0.1 M H_2SO_4.	70
Figure 3.8.	EI spectra of (a) untreated pyrite, (b) Si–Cat pyrite, and (c) Si–HTL pyrite. These Nyquist plots show curves for three types of data: experimental, fitting, and simulation results. Experimental results (black symbols) represent the original data from the EIS measurements. The observed EI spectra were analyzed by fitting to an EC model; the EC models are shown inside the Nyquist plot. The results of fitting to the EC models (solid red lines) were used to simulate the ideal circuit (black dashed lines).	72
Figure 3.9.	Schematic figure of pyrite passivation film.	76
Figure 3.10.	Bode plots of untreated pyrite, Si–Cat pyrite, and Si–HTL pyrite showing system responses as function of frequency: (a) magnitude in ohms, and (b) phase in degrees. These plots show curves for two types of data: experimental results (black symbols) and the results of fitting to the EC models shown inside the Nyquist plots (solid red lines).	77
Figure 4.1.	XRD patterns of pyrite sample from Victoria mine.	86
Figure 4.2.	Chronoamperometric curves of untreated and Si–Cat-treated pyrite samples initially pH 9.5 with different treatment time in 0.1 M H_2SO_4.	90
Figure 4.3.	EI spectra of Si–Cat-treated pyrite samples initially pH 3, 7, and 9.5; compared with untreated pyrite.	92
Figure 4.4.	EC models of (a) untreated pyrite, and (b) Si–Cat pyrite.	93
Figure 4.5.	SEM-EDX element mapping of (a) untreated pyrite; 6 hr Si–Cat-treated pyrite initially pH (b) 3, (c) 7, (d) 9.5.	95
Figure 4.6.	ATR-FTIR spectra of untreated and 6 h Si–Cat-treated pyrite samples.	97
Figure 4.7.	XP spectra of untreated and 6 h Si–Cat-treated pyrite samples with Fe 2p peaks	98

a: 707.6 eV pyrite (Nesbitt et al., 1998)
b: 710.2 eV iron oxyhydroxide (Grosvenor et al., 2004)
c: 711.3 eV iron/silicon dioxide (Gettings and Kinloch, 1977)
d: 713.25 eV $Fe_2(SO_4)_3$ (Descostes et al., 2000)

Figure 4.8. XP spectra of untreated and 6 h Si–Cat-treated pyrite samples with S 2p peaks 100
a1: $2p_{3/2}$ 161.65 eV, a2: $2p_{1/2}$ 162.83 eV S^{2-} (Nesbit and Muir, 1994)
b1: $2p_{3/2}$ 162.9 eV, b2: $2p_{1/2}$ 163.78 eV S_2^{2-} (Brion, 1980)
c1: $2p_{3/2}$ 168.25 eV, c2: $2p_{1/2}$ 169.43 eV SO_4^{2-} (Nesbit and Muir, 1994)

Figure 4.9. XP spectra of untreated and 6 h Si–Cat-treated pyrite samples with O 1s peaks 101
a: 532.0 eV $Fe_2(SO_4)_3$ (Brion, 1980)
b: 533.5 eV iron/silicon dioxide

Figure 4.10. XP spectra of untreated and 6 h Si–Cat-treated pyrite samples with Si 2p peaks. 103

Figure 4.11. Proposed mechanism of pyrite oxidation suppression by Si–Cat complex. 106

Figure 5.1. SEM-EDX element mapping of untreated and Si–Cat chalcopyrite. 118

Figure 5.2. SEM-EDX element mapping of untreated and Si–Cat molybdenite. 119

Figure 5.3. SEM-EDX element mapping of untreated and Si–Cat arsenopyrite. 120

Figure 5.4. Polarization curves of minerals working electrode in silicate and/or catechol solution for (a) chalcopyrite, (b) molybdenite, and (c) arsenopyrite. 122

Figure 5.5. Chronoamperometric curves of untreated and Si-Cat-treated minerals in 0.1 M H_2SO_4 for (a) chalcopyrite, (b) molybdenite, (c) arsenopyrite. 125

Figure 5.6. EI spectra of untreated and Si–Cat-treated minerals for (a) chalcopyrite, (b) molybdenite, and (c) arsenopyrite. 127

Figure 5.7. EC models of (a) untreated sulfide minerals, and (b) Si–Cat-treated sulfide minerals. 128

CHAPTER 1

Introduction

This chapter introduces the conducted study. Background and objectives of the study are presented as well as how this thesis is structured. Mining industry faces the most serious environmental problem caused by acid mine drainage (AMD). Once the AMD effluents have been released into the environment, the contaminations they cause affect the ecological balance. Several methods for controlling AMD generation have been investigated. The limited effectiveness of some controlling methods has led to further study of methods to overcome aforementioned problems. One of the promising methods is carrier microencapsulation by using silicon-catechol complex. The use of this method to suppress pyrite oxidation will be explained in detail in this thesis.

1.1. Theoretical background

1.1.1. Acid mine drainage

Acid mine drainage (AMD) occurs when sulfide ores are exposed to the atmosphere, which can be enhanced through mining and milling processes where oxidation reactions are initiated. Mining increases the exposed surface area of sulfur-bearing rocks allowing for excess acid generation beyond natural buffering capabilities found in host rock and water resources. Since large masses of sulfide minerals are exposed quickly during the mining and milling processes, the surrounding environment can often not attenuate the resulting low pH conditions (Jennings et al., 2008). Water contaminated by AMD often contains elevated concentrations of metals, which can be toxic to aquatic organisms, also for most living creatures. In 1989, it was estimated that ca. 19,300 km of streams and rivers, and ca. 72,000 ha of lakes and reservoirs worldwide had been seriously damaged by mine effluents, although the true scale of the environmental pollution caused by mine water discharges is difficult to assess accurately (Johnson and Hallberg, 2005). In the US alone, oxidative decomposition of pyrite is responsible for the contamination of over 16,000 km of streams and rivers and 180,000 acres of lakes and reservoirs (Tao et al., 2000).

Every mine is unique in terms of its AMD potential; thus, the nature and size of the associated risk and feasibility of mitigation options will vary from one site to another. This is despite the fact that the International Network of Acid Prevention created a Global Acid Rock Drainage Guide which is aimed to provide world-wide reference for acid prevention and to identify Best Practice in the field of AMD (Bezuidenhout et al. 2009). There are no standardized methods for ranking, measuring and reducing the risk of AMD. Considering how large the penalties can be for

miscalculating of any variables, the responsibility is on the individual mining companies to take charge of their own destinies on this front. It must begin with recognition that there are AMD hazards at individual sites, and that they give rise to specific risks. Where AMD is inevitable or likely, it makes sense to gear the response to the probability of serious consequences, which requires site-specific research to be undertaken. In mining regions where AMD has not yet formed, research should be carried out to identify ways in which it can be prevented (Morrissey, 2003).

The cost of mitigation of environmental damage from AMD is huge. Johnson and Hallberg (2005) reported that treatment technologies to address the AMD problems are very costly. As an example is mining industry in Canada that facing the largest environmental liability caused by acidic drainage and is estimated at $2 to $5 billion dollars (MEND, 2001a). Same thing also happen in South African (Oelofse, 2010).

The impact of AMD on neighboring streams and rivers can be very dramatic. The (often) low pH and high osmotic potential of AMD, the presence of toxic metals and metalloids, and the formation and deposition of particulate materials (such as iron and aluminum hydroxides) can result in stress and death of indigenous populations, particularly higher life forms such as fish, resulting in reduced biodiversity (Hallberg and Johnson, 2005). Usually the environment is capable of absorbing the effect of AMD through a combination of dilution, biological action and neutralisastion, but at high metal concentrations this ability is drastically reduced (Evangelou, 1998). These heavy metals pose a serious threat to human health, animal and ecological systems. This is because AMD contains heavy metal contaminants, such as Cu^{2+}, Fe^{3+}, Mn^{2+}, Zn^{2+}, Cd^{2+} and Pb^{2+} which are not biodegradable and tend to accumulate in living organisms,

causing various diseases and disorders (Moreno et al., 2001; Sprynskyy et al., 2006; Bailey et al., 1999).

Besides environmental impacts, AMD also possible caused the societal impact such as for people and the farming communities who used groundwater and surface water for drinking purposes, to water livestock, to irrigate crops, etc. In cases the water used for irrigation is contaminated by mine effluent, the potential exist for metal bioaccumulation in crops and consequently, this would pose a human health risk. (Van Eeden, 2006; Davies and Mundalamo, 2010). In addition, Hallberg and Johnson (2005) reported that water courses affected by mine drainage cannot be used as sources of domestic or industrial water.

As the most abundant and widespread sulfide mineral on earth, pyrite has a major influence on the biogeochemical cycles of iron, sulfur, and oxygen. Likewise, coal deposits contain variable (generally 1–20%) amounts of pyritic sulfur (a generic term that includes other iron sulfide minerals such as marcasite) as well as organic sulfur (Johnson and Hallberg, 2005). Mining of associated materials exposes pyrite to oxygen and water, and this generates highly acidic toxic solutions, previously referred as AMD; this is one of the most serious environmental problems in the mining industry (Perdicakis et al., 2001; Gleisner, 2006).

AMD occurs when (i) mining waste contains enough sulfide to react chemically and biologically to form an acid leachate at a rate too high for it be neutralized by alkaline compounds in the waste; (ii) the physical properties of the waste allow both water and oxygen to permeate in sufficient quantities to support chemical and biological reactions; and (iii) the climate is humid enough to cause rainfall infiltration and/or the waste is located on a surface where water passes through it and transports the AMD into

the environment (Hutchison and Ellison, 1992). Once the AMD effluents have been released into the environment, the contamination they cause affects the ecological balance. Although this process occurs naturally where sulfide-rich rocks are exposed, mining can promote AMD generation by increasing the quantity of exposed sulfides (Akcil and Koldas, 2006). In addition to mining, the other main source of AMD is the high volume (about 18×10^9 m^3 per annum) of mill tailings stored in impoundments or left exposed to natural weathering (Sheoron and Sheoron, 2006).

AMD is characterized by low pH and high concentrations of dissolved metals (up to 200 g/L) and sulfate (up to 760 g/L) (Hustwit et al., 1992; Nordstrom and Alpers, 1999; Nordstrom et al., 2000; Moncur et al., 2005).

The reactions for AMD generation are best illustrated by examining the oxidation of pyrite, which is one of the most common sulfide minerals and generally given as follows:

$$4FeS_{2(s)} + 14O_2 + 4H_2O \rightarrow 4Fe^{2+} + 8SO_4^{2-} + 8H^+ \quad (1.1)$$

The Fe^{2+} can be further microbially oxidized to Fe^{3+} (ferric ions) at low pH.

$$4Fe^{2+} + O_2 + 4H^+ \rightarrow 4Fe^{3+} + H_2O \quad (1.2)$$

Ferric ions are either precipitated as $Fe(OH)_3$, a red-orange precipitate, which is called "yellow boy" and is seen in AMD-affected water, or they react directly with pyrite to produce more Fe^{2+} and sulfuric acid.

$$Fe^{3+} + 3H_2O \rightarrow Fe(OH)_{3\,(S)} + 3H^+ \quad (1.3)$$

$$14Fe^{3+} + FeS_{2(s)} + 8H_2O \rightarrow 2SO_4^{2-} + 15Fe^{2+} + 16H^+ \quad (1.4)$$

As the pH decreases with sulfuric acid production, two major aspects of the reaction sequence change: (i) iron-oxidizing bacteria may intervene in Eq. (1.2), increasing the rate by a factor of 10^6; and (ii) at the same time, the ferric ions act as an

oxidizing agent in Eq. (1.4) (Kleinmann et al., 1981; Backes et al., 1993). In short, the bacteria continuously recycle the ferrous iron product of Eq. (1.4) into ferric iron. In the majority of cases, bacteria play a major role in accelerating the rate of acid generation; the inhibition of bacterial activity can therefore impede the rate of acid generation (Akcil and Koldas, 2006).

Fig. 1.1. AMD-affected water at Upper Daisy Creek, Montana (Reprinted from: USGS, 2014).

The primary factors (Akcil and Koldas, 2006) that determine the rate of acid generation are:

- pH
- Temperature
- Oxygen content of the gas phase

- Oxygen concentration in the water phase
- Chemical activity of Fe^{3+}
- Surface area of exposed metal sulfide
- Chemical activation energy required to initiate acid generation, and
- Bacterial activity.

There are many types of sulfide minerals. Iron sulfides are most common but other metal sulfide minerals may also produce AMD. Metal contamination associated with AMD depends on the type and amount of sulfide mineral oxidized, as well as the type of gangue minerals present in the rock.

AMD associated with underground mining has long been considered a serious environmental hazard. There are two sources of AMD, which are presented in Table 1.1.

Table 1.1. Sources of acid mine drainage (Akcil and Koldas, 2006).

Primary sources	Secondary sources
▪ Mine rock dumps	▪ Treatment sludge pounds
▪ Tailings impoundment	▪ Rock cuts
▪ Underground and open pit mine workings	▪ Concentrated load-out
▪ Pumped/nature discharge underground water	▪ Stockpiles
▪ Diffuse seeps from replaced overburden in rehabilitated areas	▪ Concentrate spills along roads
▪ Construction rock used in roads, dams, etc.	▪ Emergency ponds

The effectiveness and feasibility of water treatment is highly variable depending on the treatments employed and unique site characteristics. According to Johnson and Hallberg (2005), water treatment installations may include both passive and active systems. Passive water treatment systems, typically wetlands, operate without chemical

amendments and without motorized or mechanized assistance. In contrast, active water treatment systems are highly engineered water treatment facilities commonly employing chemical amendments of acid mine water to achieve a water quality standard specified in a discharge permission.

1.1.2. Sulfide Minerals

The sulfide minerals are class of minerals containing sulfide (S^{2-}) as the major anion and act as inorganic compounds. The sulfide minerals are the most important, most diverse, and richest in term of physical, chemical, and structural properties. Such diversity originates from the more complex crystal and electronic structures compared to other classes of materials (Tossel and Vaughan, 1992). The main reasons are found in the variety of oxidation states, coordination numbers, symmetry, crystal field stabilization, density, stoichiometry, and acid base surface properties that metal sulfides exhibit. The truly are fascinating compounds, capable of insulating, semiconducting, showing metallic and magnetic behaviors with continuous or sudden transitions between these states (Rao and Chernyshova, 2011).

The sulfide minerals represent higher temperatures and a slightly deeper setting than the sulfate minerals, which reflect the oxygen-rich environment near the earth's surface. Sulfides occur as primary accessory minerals in many different igneous rocks and in deep hydrothermal deposits that are closely related to igneous intrusions. Sulfides also occur in metamorphic rocks where sulfate minerals are broken down by heat and pressure, and in sedimentary rocks where they are formed by the action of sulfate-reducing bacteria.

1.1.3. Pyrite

There are many types of sulfide minerals. The most common sulfide mineral found under crustal conditions is pyrite (FeS_2), commonly referred to as "Fool's gold", which is formed at temperatures below 743°C during diagenesis, metamorphism, late-stage magnetic crystallization and hydrothermal activity, or through exsolution and recrystallization of higher-temperature sulfide phases during cooling (Richards, 1998).

Pyrite is a brass-yellow mineral with a bright metallic luster. As the most widespread sulfide mineral on earth, pyrite has a major influence on the biogeochemical cycles of iron, sulfur, and oxygen. The production of AMD usually, but not exclusively, occurs in iron sulfide mineral (pyrite).

Pyrite is present not only in many different environments, but also exhibits surface chemistry that can profoundly affect to the environment. The reactivity of pyrite that can affect to the environment might be associated with anthropogenic activities (Marchand, 2003).

Pyrite crystallizes in a rock salt type structure (face-centered cubic). The mineral adopts a cubic NaCl-like structure with the Fe atoms on the corners and face center positions of the unit cell and the S_2 units lie at the midpoints of the twelve edges and in the center of the cube.

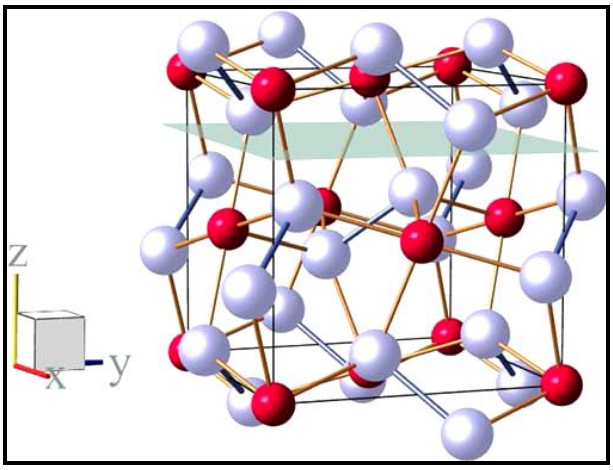

Fig. 1.2. The unit cell of pyrite FeS_2. Red atoms correspond to Fe^{2+} and grey ones to S_2^{2-}, respectively. Every iron ion is surrounded by six sulfur ions. S_2 dumb-bells are parallel with space diagonals. Sulfur ion has one S neighbour and three Fe neighbours (Reprintred from: Leiro et al., 2003).

1.1.4 Mechanism and chemistry of pyrite oxidation

In order to successfully control and prevent AMD formation, a clear and thorough understanding of the chemistry, mechanisms, and all reactants involved in AMD formation is important. The mechanism of pyrite oxidation is complex, and theories to explain this oxidation process differ considerably. While the chemical reaction theories consider the adsorption and reaction of molecular oxygen directly on the surface of pyrite, the electrochemical theories take into account the anodic dissolution of pyrite and cathodic reduction of oxygen (Hamilton and Woods, 1981). On the basis of these theories, many reaction paths and mechanisms of pyrite oxidation have been proposed. In addition, the products of pyrite oxidation have been found to vary considerably, depending upon the conditions of oxidation (Pugh et al ., 1984).

A mechanism in which oxygen is adsorbed on "reactive sites" of the pyrite has been outlined using the chemical reaction theory by Smith and Shumate (1970). The oxygen then dissociates and forms an activated complex that decomposes to form an oxidation product. The oxidation product then desorbs and another reactive site is formed. McKay and Halpern (1958) suggested that the adsorbed oxygen reacts only in a fully molecular path, designated as an atom transfer reaction as illustrated in Eq. 1.5.

$$2O_2 + FeS_2 \rightarrow Fe^{2+} + SO_4^{2-} + S° \quad (1.5)$$

Goldhaber (1983) later suggested that the initiation of pyrite oxidation is by the direct attachment of a dissolved oxygen molecule to a partially protonated pyrite surface. However, Moses and Herman (1991) found that although dissolved oxygen can directly oxidize pyrite, it can effectively do so only in the absence of Fe(II) adsorbed to the pyrite surface.

Electrochemically, pyrite dissolution is generally believed to occur according to one of the following anodic reactions (Bailey and Peters, 1976):

$$FeS_2 \rightarrow Fe^{2+} + 2S° + 2e^- \quad (1.6)$$

$$FeS_2 + 8H_2O \rightarrow Fe^{3+} + 2SO_4^{2-} + 16H^+ + 15e^- \quad (1.7)$$

$$FeS_2 \rightarrow Fe^{3+} + 2S° + 3e^- \quad (1.8)$$

$$FeS_2 + 4H_2O \rightarrow Fe^{3+} + SO_4^{2-} + S° + 8H^+ + 9e^- \quad (1.9)$$

The principal cathodic reaction is a four-electron oxygen reduction process and is represented by Eqs (1.5–1.10):

$$O_2 + 4H^+ + 4e^- \rightarrow 2H_2O \quad (1.10)$$

In the presence of dissolved Fe(III) ions, the following cathodic reaction is also suggested:

$$Fe^{3+} + e^- \rightarrow Fe^{2+} \quad (1.11)$$

The overall process is the sum of cathodic and anodic reactions that occurs at the pyrite surface.

Figure 1.3 shows the schematic representation of some of the possible reactions describing different pathways for pyrite oxidation.

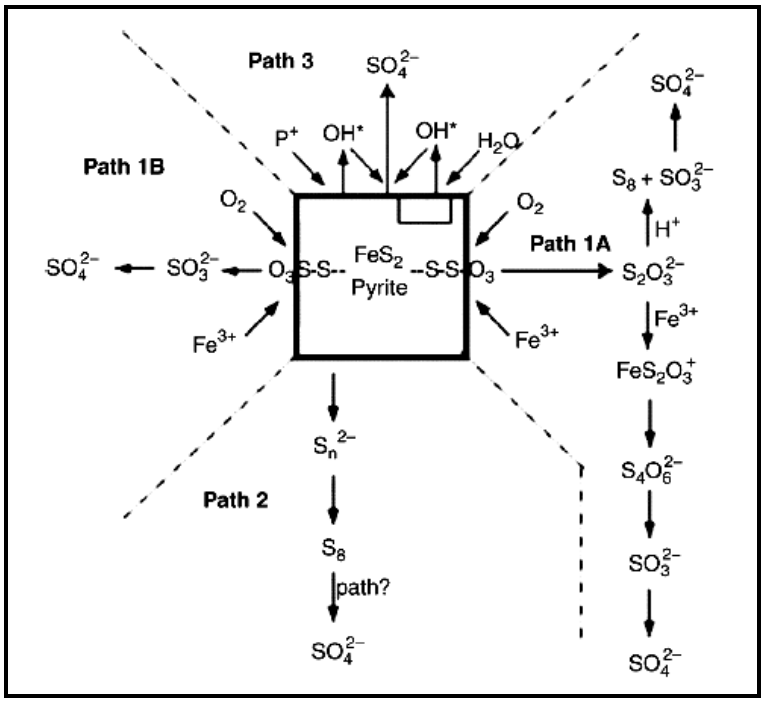

Fig. 1.3. Schematic representation of some of the possible reactions describing different pathways for pyrite oxidation. To the right is the thiosulfate pathway (Path 1A) where thiosulfate detaches and reacts, while to the left is the thiosulfate pathway where the Fe-S bond does not break; rather the S-S bond breaks, releasing sulfite which oxidizes to sulfate (Path 1B). To the bottom of the figure we represent the sulfide-polysulfide-elemental sulfur pathway (Path 2) and at the top is the defect/photochemically-driven pathway where holes or radicals react and drive S oxidation to sulfate (Path 3) (Druschel and Borda, 2006).

1.1.5 Acid mine drainage controlling methods

Acid mine drainage may arise as mine water from open pits and underground mine workings, or as surface drainage and seepage from tailings disposal facilities and waste rock dumps, and has been identified as the biggest single environment problem facing the mining industry.

Several techniques have been considered in the past for the treatment of acid mine drainage. While some of these methods are directed towards the treatment of the resulting drainage, others are directed towards prevention of AMD at source. Presently, at active mine sites and some inactive sites, where responsibility has reverted to the government, mining companies and governments operate comprehensive systems to collect and treat effluents and seepage from all sources. Although systems to collect and treat effluents at active and inactive mines, when operated well and maintained, may be sufficient to prevent downstream environmental impact, acid generation may persist for hundreds of years following mine closure (Filion et al., 1990). Many methods for controlling AMD formation have been investigated. The most common method is chemical neutralization using lime or other alkaline components to precipitate iron in the insoluble form as iron hydroxide/oxyhydroxide (Mackie and Walsh, 2012). This approach, however, has a short span of effectiveness (Evangelou, 1995). The main reason for this is that the surface of pyrite particles in mining waste are still exposed to the atmospheric O_2 after treatment. Besides that, the specific reactivity and total lime requirements cannot be accurately predicted due to variations in the waste make-up throughout pile and the lime can only be incorporated into soil up to limited depth and this strategy is costly (Caruccio et al., 1988). The use of limestone, however, has been abandoned in most chemical treatment systems because of the formation of ferric

oxyhydroxides which coat limestone in oxidizing environments and eliminate any further neutralizing capacity (Postgate, 1984). Wentzler and Aplan (1992) have also reported that iron hydroxide and gypsum coatings build up on the limestone surface inhibiting further neutralization reactions. Furthermore, the rate of the neutralization reaction was observed to decrease dramatically with increasing pH, so that limestone is not very useful above pH of 5. Though attractive economically, a fresh limestone surface must continually be presented to the acidic drainage for neutralization to occur.

Studies have also been conducted on the use of organic covers (Peppas et al., 2000) and the establishment of sustainable vegetative growth on tailings and waste rock. However, the establishment of vegetation on AMD susceptible sites has also failed to improve drainage quality (Filion et al., 1990).

Other acid mine drainage controlling techniques are explained below:

1.1.5.1. Flooding/Sealing of underground mines

The flooding and sealing of abandoned deep mines, serve to reduce the oxygen which is necessary for AMD formation. The dissolved oxygen present in the flooding waters will be consumed by mineral and other microorganisms present in the water. Atmospheric oxygen is prevented from entering the mine by sealing of the mine (Johnson and Hallberg, 2005). Mine sealing can minimize the AMD pollution associated with abandoned underground mines. The primary affecting the selection, design and construction of mine seals is the anticipated hydraulic pressure that the seal will have to withstand when sealing is completed. This procedure has commonly led to break out of the water, sometimes explosively, either at the seal or at nearby locations.

1.1.5.2. Underwater storage of mine tailings

Water covers are presently considered the best available technology for AMD prevention and long term storage of acid generating tailings (Davé, 1992). There is concern that some oxidation may still occur (Aubé et al., 1995). Dissolved oxygen could be transported through the water column to the tailings by diffusion, convection or circulating currents. Tailings resuspension by wave action might expose sulfide particles to dissolved oxygen (Li et al., 1997). If sufficient oxidation of the sulfide particles occurred, the resulting acid generation and metal flux could cause a deterioration of the water cover quality.

1.1.5.3. Land-based storage in sealed waste heaps

There are many type of covers used to minimize the movement of water and oxygen into waste heaps. Cover systems can be simple or complex, ranging from a single layer of earthen material to several layers of different material types, including native soils, suitable overburden, non-reactive waste materials, geosynthetic materials, and oxygen-consuming materials (MEND, 2004). Land-based storage in sealed waste heaps creates a sealing layer, usually comprised of clay, over an impermeable base (Swanson et al., 1997).

1.1.5.4. Blending of mineral wastes

Blending is the mixing of mineral wastes of varying acid generation and neutralization potential to create a deposit that generates a discharge of acceptable quality. The effectiveness of blending as an option depends on the availability of materials and the mine plan, the general stoichiometric balance between acid producing and acid neutralizing materials, geochemical properties, reactivity of waste rock types,

flow pathways created within the deposit, and the extent of mixing and method of blending. Homogeneous and thorough mixing is generally required to achieve maximum benefit (MEND, 1998 and 2001b). Blending of mineral wastes, comprised of acid-generating and acid-consuming materials, produces environmentally friendly composites (Mehling et al., 1997). Apart from being very costly, the blending of pyritic waste with alkaline material approach has been found to be ineffective in the long term.

1.1.5.5. Total solidification of tailings

Total solidification of tailings is achieved by adding solid-phase phosphates to mine waste in order to reduce its potential to act as an oxidant of sulfide minerals (Johnson and Hallberg, 2005).

1.1.5.6. Application of anionic surfactants (Biocides)

Microorganism can catalyze the oxidation of Fe^{2+} (Eq. 2) and continuously recycle the ferrous iron product of Eq. (4) into ferric iron. Due to that reason, the control of these microorganisms is important. Biocides are used to inhibit the activities of bacteria in mineral spoils and tailings. Biocides are anionic surfactants such as sodium dodecyl sulfate (SDS), which is highly toxic to this group of microorganisms. However, the effectiveness of biocide application has been found to only give short-term control of the problem and requires repeated applications of the chemicals (Loos et al., 1989). This is mainly because most biocides are water soluble and in running streams, they can be washed away after application. Application of anionic surfactants, which is highly toxic to biocides that are found in mineral spoils and tailings, provides short-term control.

1.1.5.7. Bioelectrochemical treatment

Bioelectrochemical treatment is a system whereby bacteria catalyze the conversion of the chemical energy from organic substrates into electrical energy (Logan et al., 2006). As the energetic performance, this system is still unsatisfactory to justify for scale-up. This treatment could be an effective solution for the treatment of Fe-dominated AMD by the consumption of excess H^+ to promote the oxygen reduction at the cathode of the system (Lefebvre et al., 2012).

1.1.5.8. Microencapsulation

In order to prevent pyrite oxidation on a long-term basis, it appears essential to prevent the contact of the atmospheric O_2 with the pyritic surfaces. This could be accomplished through passivation by using microencapsulating. Microencapsulation is a technique that can inhibit oxygen diffusion to the surface of pyrite by forming a thin protective coating on its surface (Evangelou, 1995). Once a coating is established on the surface of pyrite, oxidation of pyrite and the production of AMD are prevented.

The coating can be produced by reacting sulfidic material with low concentration of an oxidizing agent in the presence of soluble phosphate or silica in a buffered solution. Hydrogen peroxide or calcium hypochlorite has been typically used as oxidizing agents. The oxidizing agent reacts with the sulfide to produce ferric ions:

$$FeS_2 + 15/2H_2O_2 \rightarrow Fe^{3+} + 2SO_4^{2-} + 7H_2O + H^+ \quad (1.12)$$

$$FeS_2 + 15/4Ca(OCl)_2 + 1/2H_2O \rightarrow Fe^{3+} + 2SO_4^{2-} + 15/4Ca^{2+} + 15/2Cl^- + H^+ \quad (1.13)$$

Sodium acetate has been used to buffer the solution at a pH 5 to 6. At this pH, dissolved ferric iron is unstable and precipitates as ferric hydroxide. If dissolved phosphate is presence, it will scavenge ferric ions and ferric phosphate will precipitate.

$$Fe^{3+} + KH_2PO_4 \rightarrow FePO_4 + K^+ + 2H^+ \quad (1.14)$$

If silicic acid is present in the solution, it will react with the ferric hydroxides, producing an insoluble ferric silicate precipitate that is chemically stable at low pH (Evangelou, 1996).

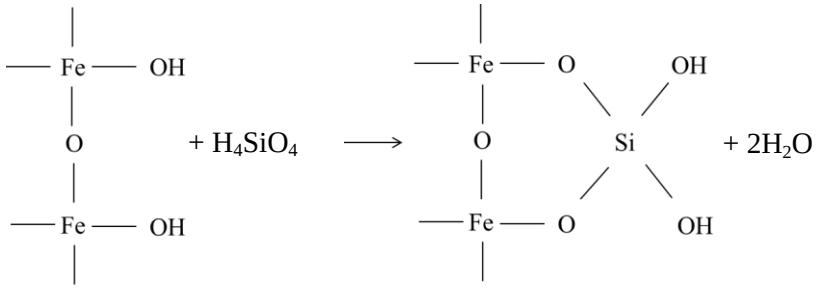

(1.15)

A number of studies have dealt with the feasibility of chemical producing coatings on reactive mine wastes and tailings. Some chemicals applied with variable success to suppress chemical reaction on pyrite surfaces by microencapsulation include acetyl acetone, humic acid, lignin, and oxalic acid (Lalvani et al., 1990, 1991). Among these coating, silica coating seems to be superior to other methods, because silica coatings are relatively water-stable solids at neutral pH, most resistant to acidic surroundings, and sustain the inhibition of AMD production for several years (Zhang and Evangelou, 1998).

Silica (silicon dioxide) is the most abundant mineral in the Earth's crust, so silica coating is friendlier to the environment than other coating methods. Besides that, silica can be polymerized easily in aqueous solutions by decreasing the pH of an alkaline silica solution, and the polymerization of silica can be controlled by increasing concentration of silica in the solution, decreasing temperature, or adding other cations, such as Fe^{3+}, Al^{3+} and so on (Iler, 1979). Therefore, the silica, which is precipitated

from concentrated silica solutions by pH adjustment, can be applied as an infill to prevent AMD.

The method known as carrier microencapsulation (CME), reported by Satur et al. (2007) and Jha et al. (2008), is a promising method for the suppression of pyrite oxidation. In CME, the pyrite is treated with aqueous solutions of metal ions (Ti^{4+} or Si^{4+}) complexed with an organic carrier such as catechol (Cat), i.e., $Si[Cat]_3^{2-}$ or $Ti[Cat]_3^{2-}$. The complex is adsorbed on the pyrite surface and decomposes oxidatively; the released metal ions are hydrolyzed to a thin layer of metal oxide or hydroxide (Jha et al., 2012).

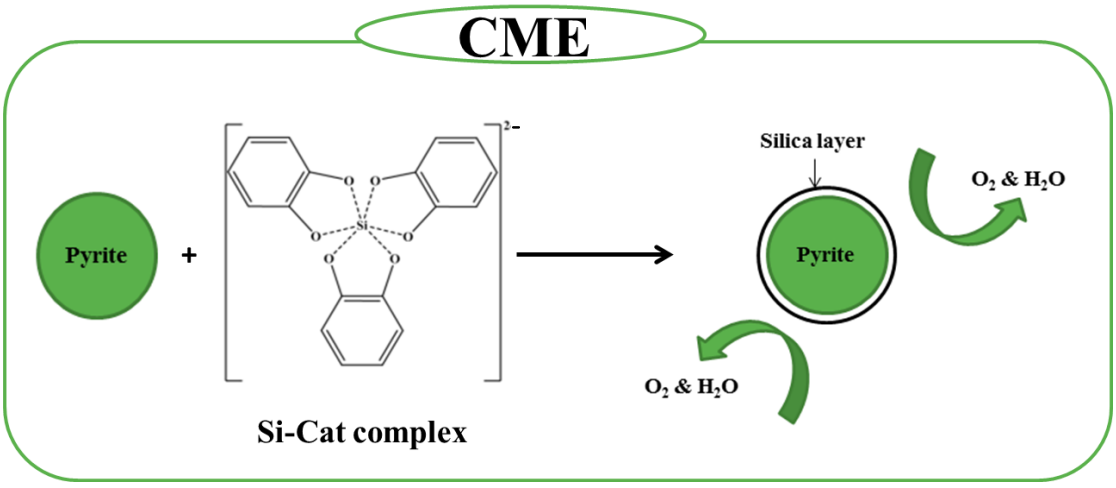

Fig. 1.4. Schematic illustration of carrier microencapsulation using Si–Cat complex.

In the first step of reaction (1.16), $Si(Cat)_3^{2-}$ is adsorbed from the aqueous phase at the anode site of the pyrite surface, and is then oxidatively decomposed to quinone and Si^{4+}.

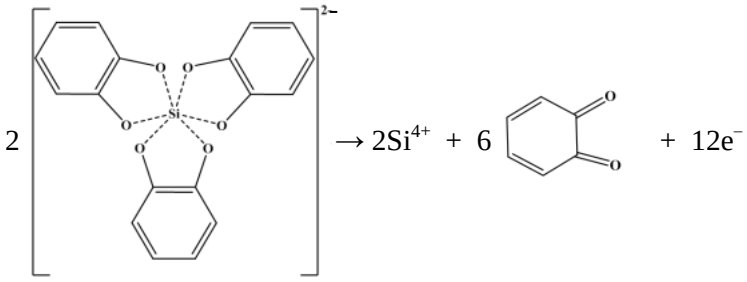

(1.16)

The electrons released are consumed by dissolved oxygen at the cathode site of the pyrite:

$$3O_2 + 12H^+ + 12e^- \rightarrow 6H_2O \quad (1.17)$$

The released Si^{4+} forms $Si(OH)_4$ or SiO_2 on the pyrite surface, as follows:

$$Si^{4+} + 4H_2O \rightarrow Si(OH)_4 + 4H^+ \quad (1.18)$$

$$Si(OH)_4 \rightarrow SiO_2 + 2H_2O \quad (1.19)$$

The overall reactions are as follows:

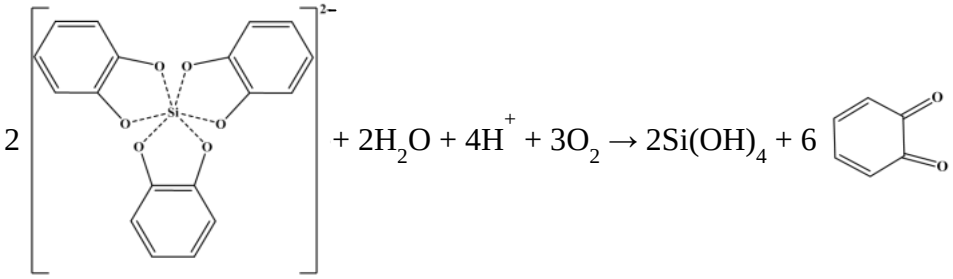

(1.20)

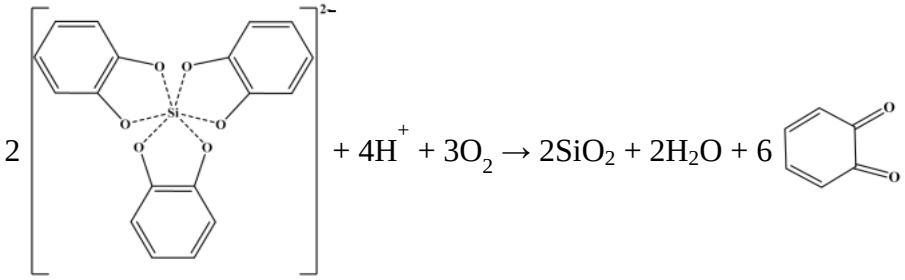

(1.21)

It was found that waste water collected from hydrothermal dewatering of tropical peat contained organic carbon at various processing temperatures (250–380°C), in the form of compounds such as methanol, acetone, butanone, organic acids, phenol,

and phenol derivatives (guaiacol, 3-pyridinol, catechol, and 2,6-dimethoxyphenol); catechol was present at high concentrations at all temperatures, along with phenol and other phenol derivatives (Mursito et al., 2010). The various liquid products obtained from hydrothermal dewatering of peat, biomass hydrothermal treatment, and hydrothermal treatment of LRC have similar characteristics, such as reducing, sterilization, and complexation abilities, which are expected to suppress pyrite oxidation.

1.2. Objective of the thesis

This has already been pointed out that AMD largely resulting from pyrite oxidation can have a devastating effect on the surrounding environment. However, avoiding mining of sulfide ores with the AMD potential formation may be difficult because they are often associated with the precious metals. Therefore, it becomes imperative to apply AMD mitigation to limit it potential impact.

As it has been mentioned above, CME by using Si–Cat complex is a promising method for the suppression of pyrite oxidation. However, the details mechanisms and the coating properties are not yet confirmed and further investigation is needed. The study reported here includes an investigation of the covering layer characteristic formed from Si–Cat complex; thus, better coating process could be applied. Besides, the utilization of byproduct of hydrothermal liquid of LRC as an organic CME carrier was also investigated (Si–HTL). In order to achieve these major objectives, experiments were carried out in 5 specified objectives:

1. To investigate the covering layer characteristic formed from Si–Cat complex.
2. To investigate the effectiveness of catechol-containing hydrothermal treatment liquid (HTL) produced from low-rank coal as a carrier in CME.

3. To determine suppression effect of Si–HTL compared with Si–Cat.
4. To investigate the optimum condition (pH and treatment time) of pyrite oxidation suppression by Si–Cat treatment.
5. To investigate the effect of Si–Cat treatment on other sulfide mineral samples: chalcopyrite, molybdenite, and arsenopyrite.

Various characterization methods were used to analyze the surface characteristics and chemical composition of coating layer. Finally, the possible mechanism of pyrite oxidation suppression by Si–Cat treatment is proposed.

1.3. Structure of the thesis

Based on above explanation, this thesis is divided into 6 chapters.

Chapter 1 presents the background and the objectives of this study. In addition, an overview of acid mine drainage and its prevention are presented in order to provide a basic understanding on pyrite oxidation suppression. Previous studies related to the present study are also discussed in this chapter.

Chapter 2 describes the effect of carrier microencapsulation (CME) using silicon (Si) and organic carriers on pyrite oxidation suppression. The use of catechol-containing hydrothermal treatment liquid (HTL) produced from low-rank coal as a carrier in CME was investigated (Si–HTL). As a comparison, a mixture of catechol and a silicon reagent (Si–Cat) was also used. Several analytical methods were applied to reveal the effectiveness of Si–HTL and Si–Cat on pyrite oxidation suppression. Results from dissolution tests and characteristics of coating layer using SEM-EDX, FTIR, AFM and DFM are presented to show the characteristics before and after treatment.

In chapter 3, three different electrochemical methods, namely, potential polarization, chronoamperometry, and electrochemical impedance spectroscopy (EIS), were used to investigate the electrochemical behavior of pyrite oxidation suppression in the presence of a silicate coating (pretreatment with either Si–HTL or Si–Cat). The electrochemical behavior of the treated pyrite samples showed oxidative decomposition of the Si–Cat complex and formation of an encapsulating layer at 690 mV for Si–HTL and 550 mV for Si–Cat. The two semi-circular curves in the Nyquist plot showed that the total impedances of the treated pyrite samples increased, indicating that another product layer has grown on the electrode surface.

In chapter 4, a more systematic investigation of the silica–quinone coating layer is presented. Pyrite treatment using Si–Cat under different conditions resulted in differences in the suppression of pyrite oxidation. The adsorption of Si–Cat and polymerization on the pyrite surface were examined. Furthermore, the mechanism involved in this coating treatment is proposed from the result of SEM-EDX, FTIR and XPS.

In chapter 5, pyrite oxidation suppression by the Si–Cat complex was applied to other sulfide minerals: chalcopyrite ($CuFeS_2$), molybdenite (MoS_2), and arsenopyrite (FeAsS). Effect of silicate covering layer on treated minerals surfaces were evaluated by potential polarization, chronoamperometry, electrochemical impedance spectroscopy (EIS), and scanning electron microscopy with energy dispersive X-ray spectroscopy (SEM-EDX).

Chapter 6 summarizes the main conclusions derived based on results and discussion in this study, and provides the outlook for further study.

References

Akcil, A., Koldas, S., 2006. Acid Mine Drainage (AMD): causes, treatment and case studies. J. Clean. Prod. 14, 1139-1145. doi:10.1016/j.jclepo.2004.09.006

Aubé, B.C., St-Arnaud, L.C., Payant, S.C., Yanful, E.K., 1995. Laboratory evaluation of the effectiveness of water covers for preventing acid generation from pyritic rock. In: Proceedings of Sudbury, 95 Conference on Mining and the Environment, Sudbury, Ont., Canada, May 28-June 1, 1995. Vol 2, pp. 495-505.

Backes, C.A., Pulford, I.D., Duncan, H.J., 1993. Seasonal variation of pyrite oxidation rates in colliery spoil. Soil Use Manage 9, 30-34.

Bailey, L.K., Peters, E., 1976. Decomposition of pyrite in acids by pressure leaching and anodization: the case for an electrochemical mechanism. Can. Metall. Q. 15, 333-334.

Bailey, S. E., Trudy, J., Olin, T. J., Bricka, M. R., Adrian, D. D., 1999. A review of potentially low-cost sorbents for heavy metals. Water Res. 33, 2469-2479.

Bezuindenhout, N., Verburg, R., Chatwin, T., ferguson, K., 2009. INAP's global acid rock drainage guide and the current state of acid rock drainage assessment and management in South Africa, International Mine Water Conference Proceedings, 19-23rd October 2009, Pretoria, South Africa.

Caruccio, F.T., Hossner, L.R., Geidel, G., 1988. In: L.R. Hossner (Ed.), Reclamation of surface-mined lands, CRC Press, Boca Raton, FL. 159-169.

Davé, N.K., 1992. Water covers on acid generating mine/mill wastes; A technical review. CANMET Report, MSL 89-107 (LS).

Davies, T.C., Mundalamo, H.R., 2010. Environmental health impacts of dispersed mineralization in South Africa. Journal of African Earth Sciences 58, 652-666.

Druschel, G., Borda, M., 2006. Comment on "Pyrite dissolution in acidic media" by M. Descostes, P. Vitorge, and C. Beaucaire. Geochim.Cosmochim. Acta 70, 5246-5250. doi: 10.1016/j.gca.2005.07.023

Evangelou, V.P., 1995. Pyrite oxidation and its control. CRC Press, Boca Raton, FL.

Evangelou, V.P., 1996. Oxidation proof silicate surface coating on iron sulfides. U.S. Patent No. 5,494,703 documentation.

Evangelou, V.P., 1998. Pyrite chemistry: the key for abatement of acid mine drainage. In: Geller, A., Klapper, H., Salomons, W., editors. Acidic Mining Lakes: Acid Mine Drainage, Limnology and Reclamation. Berlin: Springer; 197– 222.

Filion, M.P., Sirois, L.L., Ferguson, K., 1990. Acid mine drainage research in Canada. CIM Bull. 83, 33-40.

Gleisner, M., Herbert, J.R.B., Kockum, P.C.F., 2006. Pyrite oxidation by Acidithiobacillus ferrooxidans at various concentrations of dissolved oxygen. Chem. Geol. 225, 16-29.

Goldhaber, M.B., 1983. Experimental study on metastable sulfur oxyanion formation during pyrite oxidation at pH 6-9 and 30°C. Am. J. Sci. 283, 193-217.

Hallberg, K.B., Johnson, D.B., 2005. Microbiology of wetland ecosystem constructed to remediate mine drainage from a heavy metal mine. Sci. Total Environ. 338, 53-66.

Hamilton, I.C., Woods, R., 1981. An investigation of surface oxidation of pyrite and pyrrhotite by linear potential sweep voltammetry. J. Electroanal. Chem. 118, 327-343. doi: 10.1016/S0022-0728(81)80551-7

Hustwit, C.C., Ackman, T.E., Erickson, P.M., 1992. The role of oxygen transfer in acid mine drainage treatment. Water Environ. Res. 64, 817-823.

Hutchison, I.P.G., Ellison, R.D., 1992. Acid mine drainage, in: I.P.G. Hutchison, R.D. Ellison (Eds). Mine Waste Management. Lewis, Michigan, pp. 654.

Iler, R.K., 1979. Chemistry of silica. Wiley-Interscience, New York.

Jha, R.K.T., Satur, J., Hiroyoshi, N., Ito, M., Tsunekawa, M., 2008. Carrier-Microencapsulation using Si–catechol complex for suppressing pyrite floatability. Miner. Eng. 21, 889-893. doi:10.1016/j.mineng.2008.02.011

Jha, R.K.T., Satur, J., Hiroyoshi, N., Ito, M., Tsunekawa, M., 2012. Suppression of Pyrite Oxidation by Carrier Microencapsulation using Silicon and Catechol. Miner. Process. Extr. M. 33, 89-98. doi:10.1080/08827508.2011.562946

Jennings, S.R., Neuman, D.R., Blicker, P.S., 2008. Acid mine drainage and effects on fish health and ecology: a review. Reclamation Research Group Publication, Bozeman, MT.

Johnson, D.B., Hallberg, K.B., 2005. Acid mine drainage remediation options: a review. Sci. Total Environ. 338: 3-14. doi:10.1016/j.scitotenv.2004.09.002

Kleinmann, R.L.P., Crerar, D.A., Pacellli, R.R., 1981. Bio-geochemistry of acid mine drainage and a method to control acid formation. Min. Eng.-Littleton 3, 300-305.

Lalvani, S.B., DeNeve, B.A., Weston, A., 1990. Passivation of pyrite due to surface treatment. Fuel 69, 1567-1569. doi:10.1016/0016-2361(90)90209-9

Lalvani, S.B., DeNeve, B.A., Weston, A., 1991. Prevention of pyrite dissolution in acidic media. Corrosion 47, 55-61. doi: http://dx.doi.org/10.5006/1.3585220

Lefebvre, O., Neculita, C. M., Yue, X., Ng, H.Y., 2012. Bioelectrochemical treatment of acid mine drainage dominated with iron. J. Hazard. Mater. 241-242, 411-417.

Leiro, J.A., Mattila, S.S., Laajalehto, K., 2003. XPS study of the sulphir 2p spectra of pyrite. Surf. Sci. 547, 157-161. doi:10.1016/j.susc.2003.09.033

Li, M.G., Aube, B.C., St-Arnaud, L.C., 1997. Considerations in the use of shallow water covers for decommissioning reactive tailings, Proceedings of the Fourth International Conference on Acid Rock Drainage, May 30–June 6, Vancouver, BC, I, pp. 115-130.

Logan, B.E., Hamelers, B., Rozendal, R., Schrorder, U., Keller, J., Freguia, S., Aelterman, P., Verstraete, W., Rabaey, K., 2006. Microbial fuel cells: methodology and technology, Environ. Sci. Technol. 40, 5181–5192.

Loos, M.A., Bosch, C., Mare, J., Immelman, E., Sanderson, R.D., 1989. Evaluation of sodium lauryl sulphate, sodium benzoate and sorbic acid as inhibitors of acidification of South African coal waste. Groundwater and Mining: Proceedings of the 5th Biennial Symposium of the Groundwater Division of the Geological.

Mackie, A.L., Walsh, M.E., 2012. Bench-scale study of active mine water treatment using cement kiln dust (CKD) as a neutralization agent. Water Research 46, 327-334. doi:10.1016/j.watres.2011.10.030

Marchand, E.A., 2003. Minerals and Mine Drainage. Water Environ. Res. 75, 975-1011.

McKay, D.R., Halpern, J., 1958. A kinetic study of the oxidation of pyrite in aqueous suspension. Trans. Metall. Soc. 212, 301-309.

Mehling, P.E., Day, S.J., Sexsmith, K.S., 1997. Blending and layering waste rock to delay, mitigate or prevent acid generation: a case review study, Proceedings of the Fourth International Conference on Acid Rock Drainage, May 30–June 6, Vancouver, BC, II, pp. 953-970.

MEND (Mine Environmental Neutral Drainage), 1998. Blending and Layering Waste Rock to Delay, Mitigate or Prevent Acid Rock Drainage and Metal Leaching: A Case Study Review. Report 2.37.1, CANMET.

MEND (Mine Environmental Neutral Drainage), 2001a. List of potential information requirements in metal leaching/acid rock drainage assessment and mitigation work. Mining Environment Neutral Drainage Program. W. A. Price, CANMET.

MEND (Mine Environmental Neutral Drainage), 2001b. Prevention and Control. Volume 4. Manual 5.4.2d. G.A. Tremblay and C.M. Hogan (Eds.), CANMET.

MEND (Mine Environmental Neutral Drainage), 2004. Design, construction and performance monitoring of covers systems for waste rock and tailings. Canadian Mine Environment Neutral Drainage Program, Project 2.21.4.

Moncur, M.C., Ptacek, C.J., Blowes, D.W., Jambor, J.L., 2005. Release, transport and attenuation of metals from an old tailings impoundment. Appl. Geochim. 20, 639-659. doi:10.1016/j.apgeochem.2004.09.019

Moreno, N., Querol, X., Ayora, C., 2001. Utilization of zeolites synthesized from coal fly ash for the purification of acid mine waters. Environ. Sci. Technol. 35, 3526-3534. doi: 10.1021/es0002924

Morrissey, C., 2003. Mining's malignant menace. In: Review Magazine, Vol. 68. 6 St. James' Square, London: Rio Tinto, pp. 1-8.

Mursito, A.T., Hirajima, T., Sasaki, K., Kumagai, S., 2010. The effect of hydrothermal dewatering of Pontianak tropical peat on organics in wastewater and gaseous produtcs. Fuel 89, 3934-3942. doi:10.1016/j.fuel.2010.06.035

Moses, C.O., Herman, J.S., 1991. Pyrite oxidation at circumneutral pH. Geochim. Cosmochim. Acta 55, 471-482. doi:10.1016/0016-7037(91)90005-P

Nordstrom, D.K., Alpers, C.N., 1999. Negative pH, efflorescent mineralogy, and consequences for environmental restoration at the Iron Mountain Superfund site, California, in: National Academy of Sciences colloquium "Geology, Mineralogy, and Human Welfare", Irvine, CA, USA, 1999, pp. 3455–3462.

Nordstrom, D.K., Alpers, C.N., Ptacek, C.J., Blowes D.W., 2000. Negative pH and extremely acidic mine waters from Iron Mountain, California. Environ. Sci. Technol. 34, 254-258.

Oelofse, S., 2010. The pollution reality of gold mining waste on the Witwatersrand, Waste water management. ReSource, 51-55.

Peppas, A., Komnitsas, K., Halikia, I., 2000. Use of organic covers for acid mine drainage control. Miner. Eng. 13, 563-574. doi:10.1016/S0892-6875(00)00036-4

Perdicakis, M., Geoffroy, S., Grosselin, N., Bessiere, J., 2001. Application of the scanning reference electrode technique to evidence the corrosion of a natural conducting mineral: Pyrite inhibiting role of thymol. Electrochim. Acta. 47, 211-216.

Postgate, J.R., 1984. The Sulfate Reducing Bacteria. Cambridge University Press: Cambridge, pp. 208.

Pugh, C.E., Hossner, L.R., Dixon, J.B., 1984. Oxidation rate of iron sulfides as affected by surface area, morphology, oxygen concentration, and autotrophic bacteria. Soil Sci. 137, 309-314. doi: 10.1097/00010694-198405000-00003

Rao, K.H., Chernyshova, I.V., 2011. Challenges in Sulphide Mineral Processing. The Open Mineral Processing Journal 4, 7-13.

Richards, J.P., 1998. Sulfide minerals. Geochemistry Encyclopedia of Earth Science. Springer Netherlands. doi: 10.1007/1-4020-4496-8_304

Satur, J., Hiroyoshi, N., Tsunekawa, M., Okamoto, H., 2007. Carrier-Microencapsulation for preventing pyrite oxidation. Int. J. Miner. Process. 83, 116-124. doi:10.1016/j.minpro.2007.06.003

Sheoran, A.S., Sheoran, V., 2006. Heavy metal removal mechanism of acid mine drainage in wetlands: A critical review. Miner. Eng. 19, 105–116.

Smith, E.E., Shumate, R.S., 1970. The sulfide to sulfate reaction mechanism. Report no. 14010 FPS, Federal Water Pollution Control Administration: Washington, DC, pp. 20.

Sprynskyy, M., Boguslaw B., Terzyk, A.P., Namiesnik, J., 2006. Study of the selection mechanism of heavy metal (Pb^{2+}, Cu^{2+}, Ni^{2+} and Cd^{2+}) adsorption on clinoptilolite. J. Colloid Interface Sci. 304, 21-28.

Swanson, D.A., Barbour, S.L., Wilson, G.W., 1997. Dry-site versus wet-site cover design, Proceedings of the Fourth International Conference on Acid Rock Drainage, May 30–June 6, Vancouver, BC, IV, pp. 1595–1610.

Tao, D., Abdelkhalck, M., Chen, S., Parekh, B.K., Hepworth, M.T., 2000. Environmental issues and management of waste in energy and mineral production, in: Proceedings of the International Conference on Environmental Issues and Management of Waste in Energy and Mineral Production, 6th, Calgary, AB, Canada, May 30-June 2, pp. 347-353.

Tossell, J.A., Vaughan, D.J., 1992. Theoretical Geochemistry: Application of Quatum Mechanics in the Earth and Mineral Sciences. Oxford University Press. New York.

USGS (United States Geological Survey), 2014. Development and Research: Diurnal Metal Variations in Streams. Accessed June 5, 2015. Available from:

http://toxics.usgs.gov/photo_gallery/photos/metals_variation/UpperDaisyCreek_lg.jpg

Van Eeden, E.S., Liefferink, M., Durand, J.F., 2009. Legal issues concerning mine closure and social responsibility on the West Rand. The Journal for Transdisciplinary Research in Southern Africa 5, 51-71.

Wentzler, T.H., Aplan, F.F., 1992. In Proceedings of the Symposium on Emerging Process Technologies for a Cleaner Environment, Chander, S., Richardson, P.E., El-Shall H. (eds). SME: Phoenix, AZ, 149.

Zhang, Y.L., Evangelou, V.P., 1998. Formation of ferric hydroxide-silica coatings on pyrite and its oxidation behavior. Soil Sci. 163, 53-62. doi:10.1097/00010694-199801000-00008

CHAPTER 2

Suppression of Pyrite Oxidation by Carrier Microencapsulation using Si–HTL and Si–Cat

Chapter 2 describes suppression of pyrite oxidation by carrier microencapsulation (CME) with silicon (Si) and an organic carrier. It was found that waste water collected from hydrothermal treatment (HT) of low-rank coal contains organic carbon compounds, such as phenol and catechol. The use of HT liquid (HTL) produced from low-rank coal as a carrier in CME was investigated. In dissolution tests for 51 days with pyrite and iron-oxidizing bacteria, treatment with a mixture of HTL and a silicon reagent (Si–HTL) lowered the ferric ion concentration and limited bacterial attachment compared with untreated pyrite. A mixture of catechol and a silicon reagent (Si–Cat) was also used, and the coatings obtained using Si–HTL and Si–Cat were compared.

2.1. Introduction

Hydrothermal treatment (HT) is one of the important pretreatment processes involves applying heat under pressure to achieve reaction in aqueous medium. It has been attracting worldwide attention because of the fascinating characteristics of water as reaction medium at elevated temperatures and pressures (Savage, 1999). During the process, various reactions such as oxidation, hydrolysis, dehydration and thermal decomposition can be carried out energetically so that the reaction can be successfully used for oxidizing organic wastes to CO_2 and other innocuous end products, as well as for conversion of organic wastes to fuels or useful materials (He et al., 2008).

Many studies have been conducted to evaluate the hydrothermal treatment of carbonaceous materials such as coal, biomass, and peat (Blazsó et al., 1986; Ross et al., 1991; Timpe et al., 2001; Racovalis et al., 2002; Karagöz et al., 2005; Mursito et al, 2010). Those treatments commonly produce upgraded solids, but do not take into account considerations of wastewater products.

The recovery of waste substances is not only important for prevention of environmental issues, but also for rational utilization of natural resources (He et al., 2008). It was found that waste water collected from hydrothermal dewatering of tropical peat contained organic carbon at various process temperatures (250–380°C), in the form of compounds such as methanol, acetone, butanone, organic acids, phenol, and phenol derivatives (guaiacol, 3-pyridinol, catechol, and 2,6-dimethoxyphenol); catechol was present at high concentrations at all temperatures, along with phenol and other phenol derivatives (Mursito et al., 2010).

As reported by Satur et al. (2007) and Jha et al. (2008), catechol (Cat) can be used as organic carrier in carrier microencapsulation (CME) to suppress pyrite oxidation. In this method, the pyrite sample is treated with aqueous solutions of metal ions (Ti^{4+} or Si^{4+}) complexed with catechol, i.e., $Si[Cat]_3^{2-}$ or $Ti[Cat]_3^{2-}$. The complex is adsorbed on the pyrite surface and decomposes oxidatively; the released metal ions are hydrolyzed to a thin layer of metal oxide or hydroxide (Jha et al., 2012). The properties of this covering layer are poorly understood, and the work reported here includes an investigation of the covering layer chemistry.

The various liquid products obtained from hydrothermal dewatering of peat, biomass hydrothermal treatment, and hydrothermal treatment of LRC have similar characteristics, such as reducing, sterilization, and complexation abilities, which are expected to suppress pyrite oxidation. A major objective of the present study was to determine whether these liquid products (especially catechol) can be used to suppress pyrite oxidation. Experiments in which the hydrothermal treatment liquid (HTL) products of LRC were evaluated are reported in this chapter.

2.2. Materials and methods

2.2.1. Materials

2.2.1.1. Pyrite

Pure crystalline pyrite was used for dissolution tests. The analytical results for the pyrite (from the Saimoku mine, Gunma, Japan), obtained using inductively coupled plasma atomic emission spectroscopy (ICP-AES Agilent 725, Santa Clara, CA., USA) and X-ray diffraction (XRD Rigaku Ultima IV diffractometer, Tokyo, Japan; Cu Kα [40

kV, 40 mA] radiation; scanning speed 2 min^{-1}, and scanning step 0.02°), are shown in Table 2.1 and Fig. 2.1.

Table 2.1. Elemental compositions of pyrite sample from Saimoku mine, determined using ICP-AES.

Element	Percentage by weight
Fe	44.7
S	53.8
Al	0.13
Cu	0.007
K	<0.1
Zn	<0.01
Si	<0.2

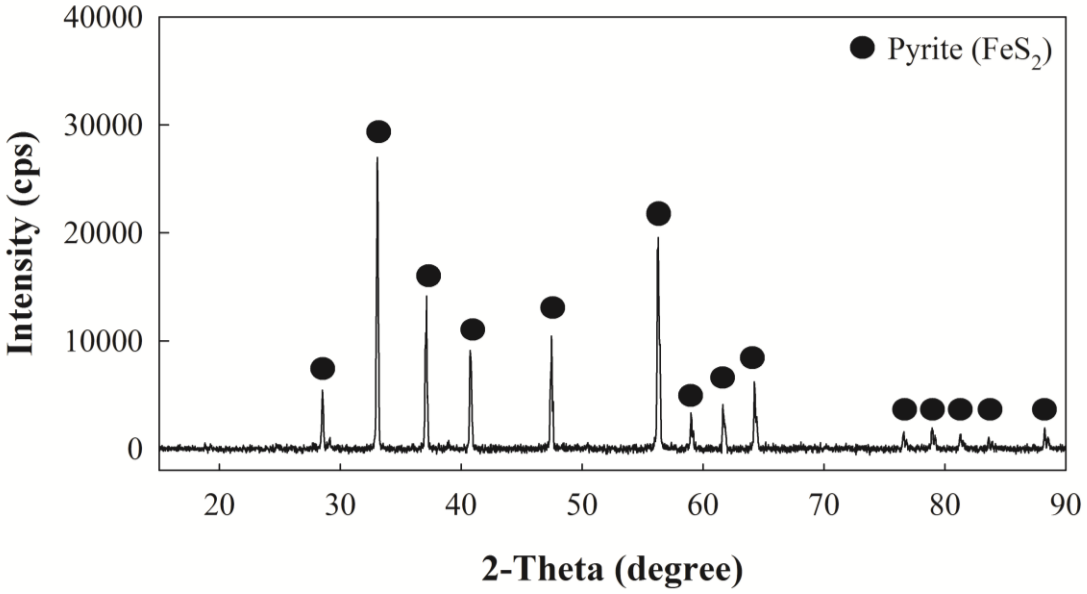

Fig. 2.1. XRD patterns of pyrite sample from Saimoku mine.

For the dissolution tests and coating characteristics, a pyrite sample was ground to +38–75 μm on an agate mortar in a nitrogen-purged glove box. After grinding, the

washing method reported by Sasaki et al. (1995) was used to remove the surface oxide. Finally, the washed pyrite was dried by freezing dehydration.

2.2.1.2. Liquid product from hydrothermal treatment of LRC

Loy Yang Coal, an Australian brown coal, was hydrothermally treated to generate the liquid product for using in the present CME experiments. First, a vessel was filled with 30.00 g (dry basis) of the sample (−275 μm in diameter), 300 mL of ultrapure water, and nitrogen gas at an initial pressure of 2.0 MPa. The vessel was heated to 350 °C and the reaction temperature was held for 30 min. After air-cooling, the gas phase was sampled and the vessel was opened to recover the slurry. The slurry was filtered using a sheet of 5C filter paper to separate the solid and liquid phases. The properties of raw Loy Yang Coal and the results of the solid product analysis are listed in Table 2.2.

Table 2.2. Proximate and ultimate analyses of Loy Yang Coal.

Properties	**Raw**	**Solid product of HT 350 °C**
Proximate analysis (wt%)		
Volatile matter (d.a.f)	51.9	42.4
Fixed carbon (d.a.f)	48.1	57.6
Ash (d.b)	1.2	0.8
Ultimate analysis (wt.%) (d.a.f)		
C	64.8	75.2
H	4.9	5.1
O (diff)	29.7	19.0
N	0.6	0.7

d.b. = dry basis; d.a.f = dry ash free basis; diff. = differences

Qualitative and quantitative analyses of the organic material in the liquid product were performed using gas chromatography-mass spectrometry (GC-MS Agilent 6890N

[Wilmington, USA] and JEOL Jms-Q1000GC [Tokyo, Japan]), with a J&W Scientific methyl silicon capillary column measuring 0.32 mm × 60 m. The concentrations of selected typical organic compounds in the HTL of the LRC are listed in Table 2.3.

Table 2.3. Concentrations of selected typical organic compounds in HTL of LRC, determined using GC-MS.

Compounds	Formula	Concentration (ppm)
Catechol (1,2-benzenediol)	$C_6H_6O_2$	797.19
Phenol	C_6H_6O	85.92

2.2.2. Methods

2.2.2.1. Pretreatment of pyrite and dissolution tests

The HTL was diluted with ultrapure water to adjust its catechol concentration to 7.00 mmol/L. For comparison, catechol (Wako, special grade) was added to ultrapure water, and the catechol concentration was also adjusted to 7.00 mmol/L. Subsequently, sodium metasilicate nonahydrate (Wako, special grade) was added to the diluted HTL and catechol solutions, and the sodium metasilicate nonahydrate concentrations were adjusted to 2.34 mmol/L. The diluted HTL (Si–HTL) and diluted catechol (Si–Cat) solutions were then used for pyrite surface treatments.

A washed pyrite sample (10.00 g) was added to 100 mL of Si–HTL solution in a 250 mL bottle and the mixture was shaken for 1 h at 100 rpm and 25 °C. A washed pyrite sample (10.00 g) was added to 100 mL of Si–Cat solution in another 250 mL bottle, and the mixture was shaken for 1 h at 100 rpm and 25 °C. The solid residues

were recovered from each bottle by filtration and dried by freezing dehydration. These two treated pyrite samples are denoted by Si–HTL pyrite and Si–Cat pyrite.

Dissolution tests were conducted in three 500 mL Erlenmeyer flasks each containing 2.00 g of pyrite in 200 mL of 9K basal medium of composition $(NH_4)_2SO_4$ 3.0 g/L, KCl 0.1 g/L, K_2HPO_4 0.5 g/L, $MgSO_4 \cdot 7H_2O$ 0.5 g/L, $Ca(NO_3)_2 \cdot 4H_2O$ 0.01 g/L, and pH 2.0 (Silverman and Lundgren, 1959), and 1.0×10^7 cells/mL of the iron-oxidizing bacterium *Acidithiobacillus ferrooxidans* (ATCC 23270), with shaking at 100 rpm and 25 °C. One flask contained Si–HTL pyrite/bacteria, one flask contained Si–Cat pyrite/bacteria, and the third flask contained untreated pyrite/bacteria. In a fourth, sterile, control experiment flask, sodium azide solution (0.10 mmol/L) was added to untreated pyrite (untreated pyrite/sterilized).

During the dissolution tests, the live-cell numbers (detected using a hemocytometer), pH, and oxidation-reduction potential (ORP) were monitored; liquid samples were taken, filtered, and their total iron and ferrous ion concentrations were determined using the *o*-phenanthroline method. After leaching for 51 days, the solid residues were removed and dried. Microscopic observations and elemental analysis of the dried solids were performed using SEM-EDX (Keyence VE-9800, Osaka, Japan).

2.2.2.2. Surface characteristics of coating layer on pyrite

Pyrite powder was prepared as described in Section 2.2.2.1. The surface morphologies of the samples were investigated using SEM-EDX and FTIR. The data were compared with those for untreated pyrite, as discussed below.

For atomic force microscopy (AFM) and dynamic force microscopy (DFM) analyses, the massive pyrite sample was cut as a flat shape and then it was exposed for

polishing from #400 to #4000 emery, a Texmet (Buehler, IL, USA) perforated non-woven pad, and a DP-Nap (Struers, Ballerup, Denmark) fine polishing cloth mounted on a plate using 3 μm and 1 μm diamond sprays.

Untreated and treated pyrite samples were examined by AFM and DFM to investigate their morphology, changes in their surface characteristics and surface adhesion force. AFM and DFM images were collected in contact mode using a silicon nitride cantilever SN-AF01S-NT from SII with a resonance frequency of 33.7 kHz and a spring constant of 0.08 N/m at a scan rate of 0.4 Hz. Images were collected for each of untreated and treated samples. Topographical and phase images were obtained by means of NanoNavi S-image atomic force microscopy (Seiko Instruments Inc., Chiba, Japan).

2.3. Results and discussion

2.3.1. Dissolution tests

The dissolution tests mimicked the natural oxidation reaction of pyrite. The tests were used to investigate the effects on acid generation of pyrite samples that had undergone different treatments. In the dissolution tests, the pyrite was dissolved and the resulting Fe^{2+} was further microbially oxidized to Fe^{3+} at low pH, followed by the reactions in Eq. (1.3) and (1.4). The changes that occurred during the dissolution tests were recorded as a function of time: cells number (Fig. 2.2), ferric ion concentration (Fig. 2.3), total iron concentration (Fig. 2.4), pH (Fig. 2.5), and ORP (Fig. 2.6). These changes were used to assess the effects of different treatments.

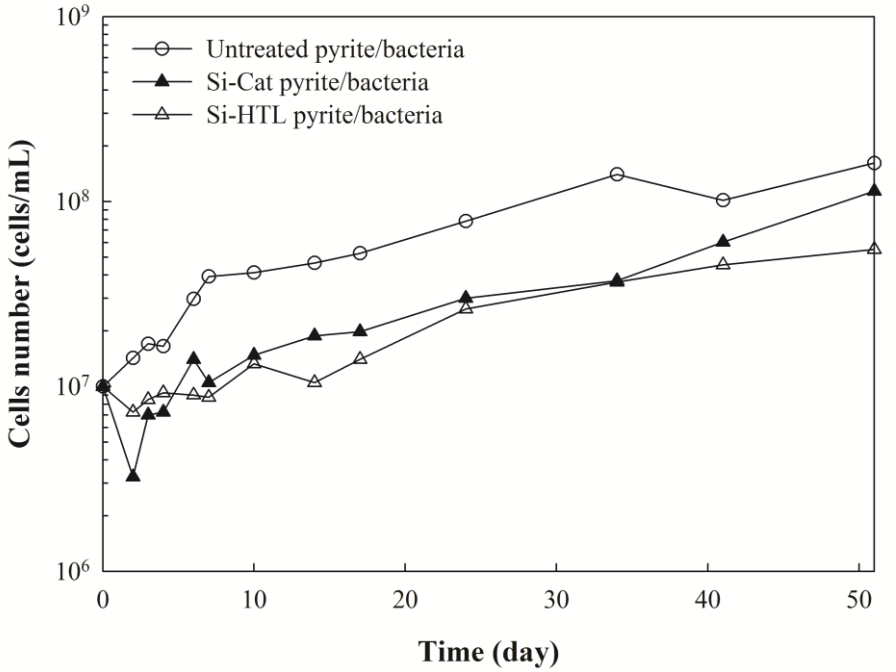

Fig. 2.2. Changes in cells number with time.

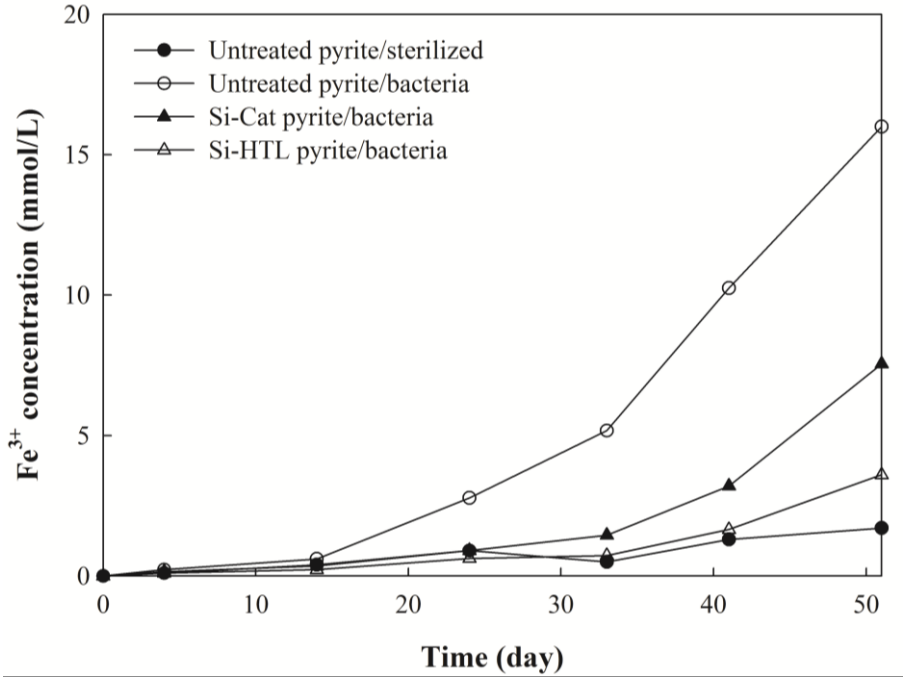

Fig. 2.3. Changes in ferric ion concentration with time.

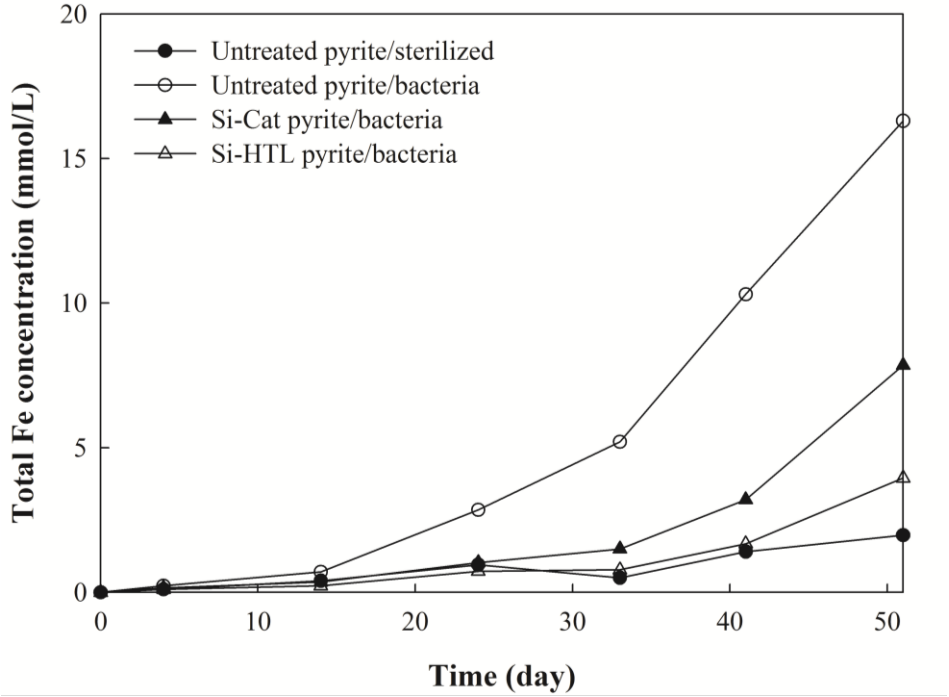

Fig. 2.4. Changes in total iron concentration with time.

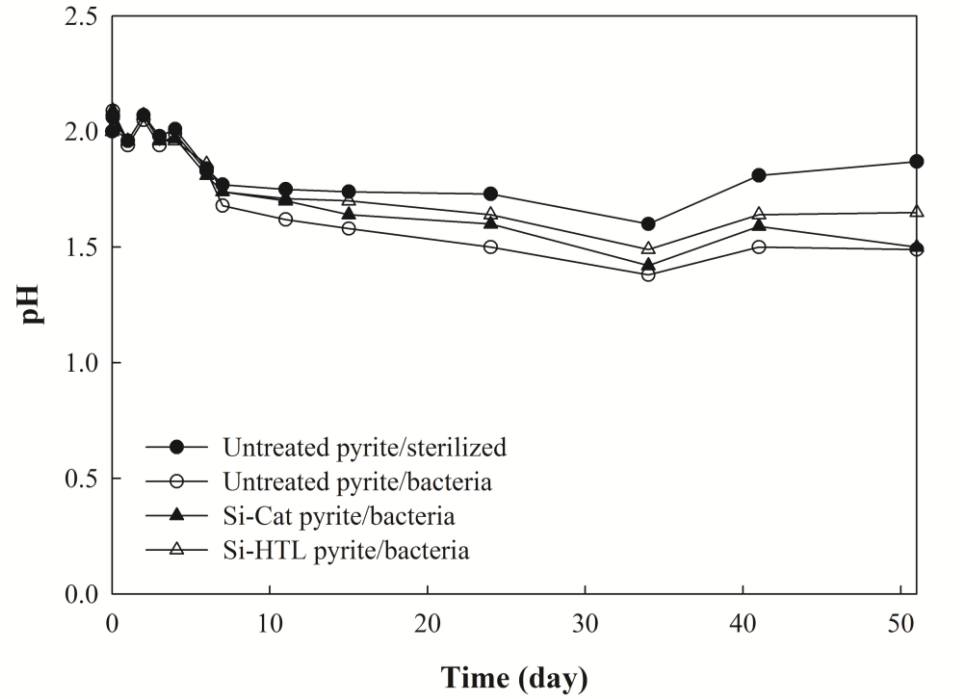

Fig. 2.5. Changes in pH with time.

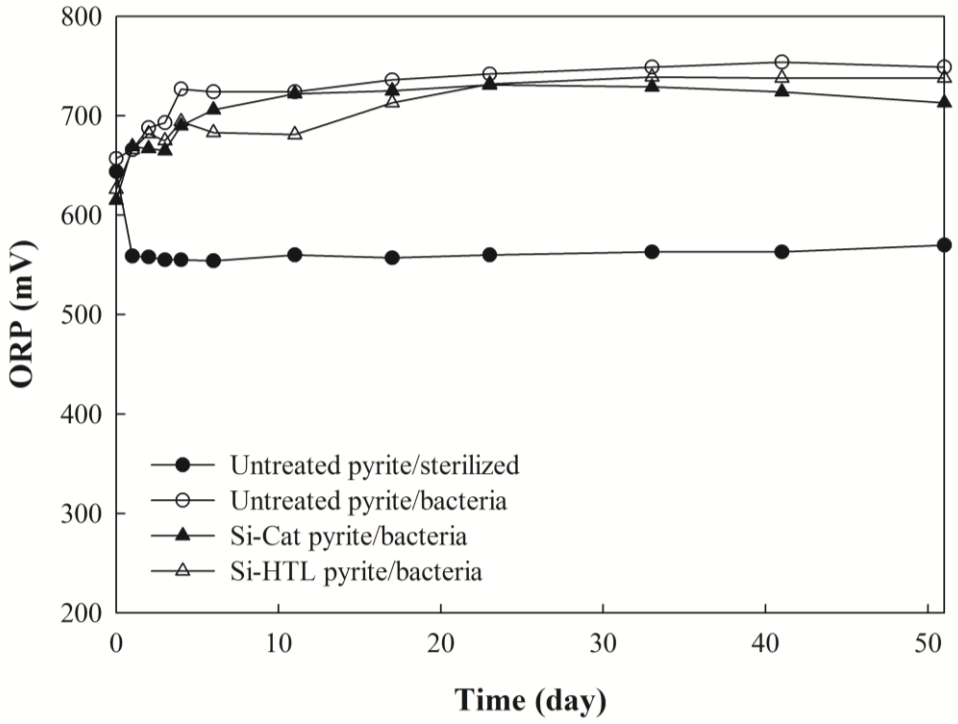

Fig. 2.6. Changes in ORP with time.

In the case of untreated pyrite, in the presence of iron-oxidizing bacteria (untreated pyrite/bacteria), the bacterial population grew rapidly to about 1.6×10^8 cells/mL. These bacteria may have accelerated the oxidation of dissolved ferrous ions, because the ferric ion concentration of this sample was much higher than those of the others (912 ppm) after leaching for 51 days. Because of the ferric ion concentration, the pH decreased from 2.00 to 1.49 and the ORP increased to 750 mV. In the sterile control experiment (untreated pyrite/sterilized), the total dissolved iron was 111 ppm, and the pH decreased moderately to 1.87, with the ORP remaining at 560 mV after leaching for 51 days.

The iron-oxidizing bacteria populations in the Si–HTL pyrite and Si–Cat pyrite samples grew moderately, to 5.5×10^7 and 1.1×10^8 cells/mL, respectively.

Because the dissolution conditions were the same in the experiments with and without bacteria, the effect of pyrite treatment (with HTL or catechol) on the dissolution of pyrite could be determined directly by comparing the amounts of iron released. Figure 2.3 shows the amounts of dissolved ferric ions for treated pyrite and untreated pyrite samples, with and without bacteria. In the Si–Cat pyrite/bacteria sample, the ferric ion concentration was only about half that of the untreated pyrite/bacteria sample. The Si–HTL pyrite/bacteria sample had the lowest ferric ion concentration of all the non-sterile samples, namely 221 ppm. These results indicate that HTL can be used to suppress pyrite oxidation.

Figure 2.7 shows SEM images of the pyrite samples after leaching for 51 days. The surface of the untreated pyrite/sterilized sample was not eroded (Fig. 2.7a), but the surface of the untreated pyrite/bacteria sample was eroded and covered with a significant number of bacteria (Fig. 2.7b). These results can be explained by the contact mechanism proposed by Fowler et al. (2001) and Crundwell (2003), in which bacteria attached to a pyrite surface oxidize ferrous ions to ferric ions, and then the ferric ions leach the mineral surface and create erosive surface pores. The pyrite surface erosion shows that the bacteria were very active in catalyzing the oxidation of ferrous ions, and confirms the dissolution test results, which showed that the ferric ion concentration was highest for the untreated pyrite/bacteria sample (Fig. 2.3). In contrast, the Si–Cat pyrite/bacteria and Si–HTL pyrite/bacteria samples were not eroded, but the surfaces appeared to have peeled off and the numbers of iron-oxidizing bacteria attached to the surfaces were very low (Fig. 2.7c and 2.7d). These results suggest that the pyrite surfaces of these samples were covered with a layer that impeded the bacterial contact mechanism. Notably, from the beginning of the dissolution tests until day 41, the ferric

ion concentrations in the Si–Cat pyrite/bacteria and Si–HTL pyrite/bacteria samples were similar to the concentrations in the untreated pyrite/sterilized sample. However, after 41 days, the ferric ion concentration increased gradually in the treated samples. It is possible that the shaking process peeled off the coating layer and exposed a new surface to the solution; this exposed surface would then be oxidized and catalyzed by newly attached bacteria, resulting in increased ferric ion concentrations (Fig. 2.3).

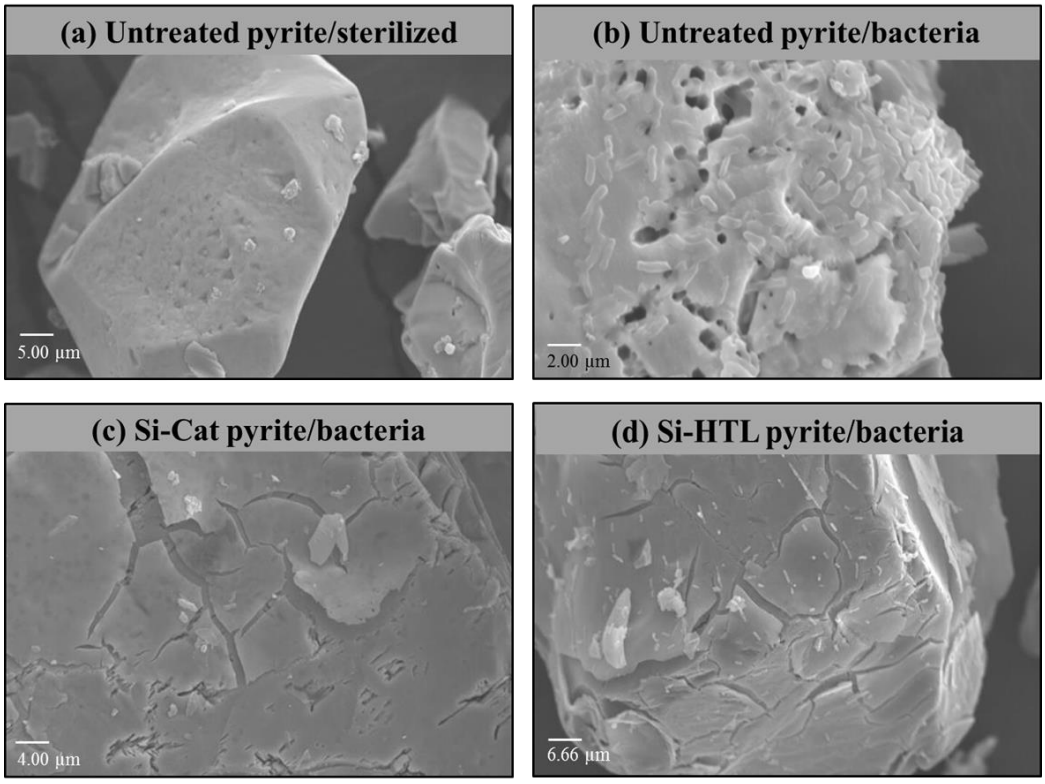

Fig. 2.7. SEM images of pyrite samples: (a) untreated pyrite/sterilized, (b) untreated pyrite/bacteria, (c) Si–Cat pyrite/bacteria, and (d) Si–HTL pyrite/bacteria.

2.3.2. Surface characteristics of coating layer on pyrite

The surface morphologies of the untreated and treated pyrite samples by using SEM-EDX element mapping are shown in Figs. 2.8, 2.9, and 2.10.

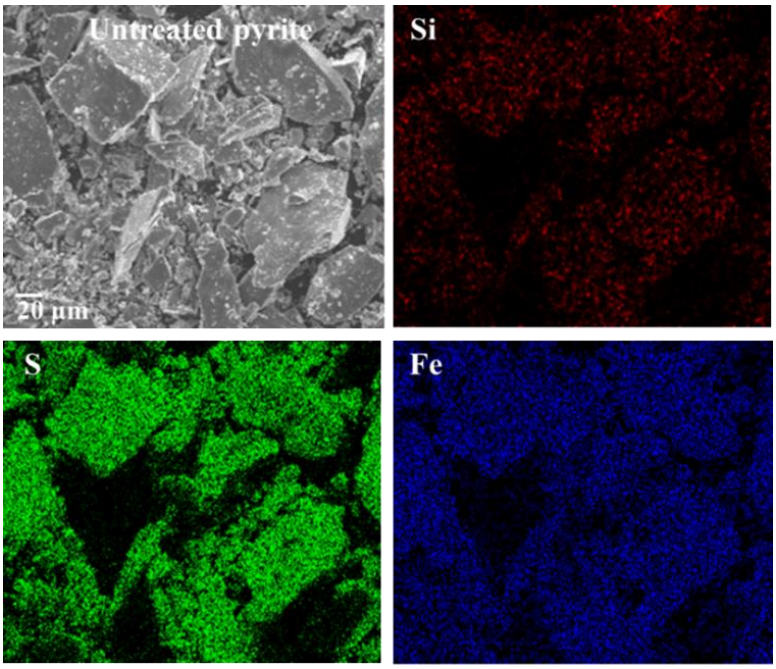

Fig. 2.8. SEM-EDX element mapping of untreated pyrite.

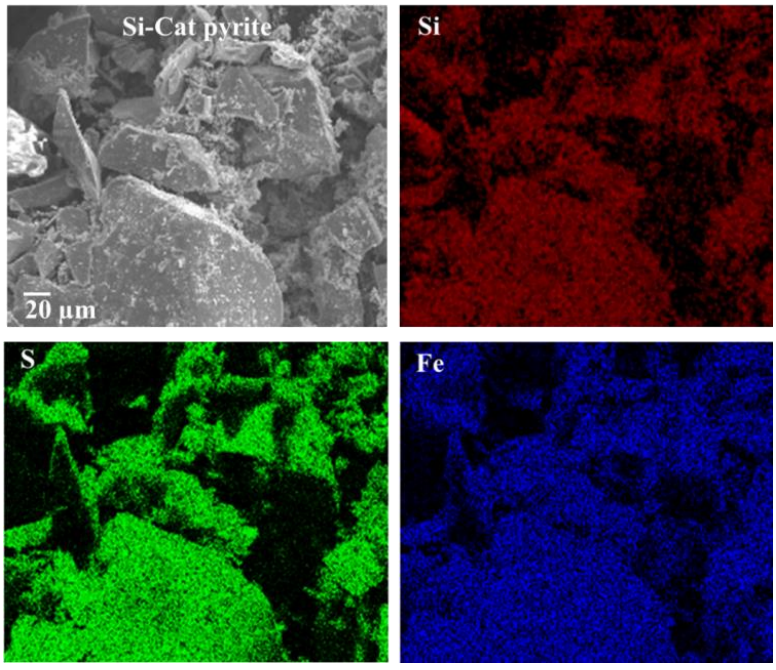

Fig. 2.9. SEM-EDX element mapping of pyrite in presence of Si–Cat (Si–Cat pyrite).

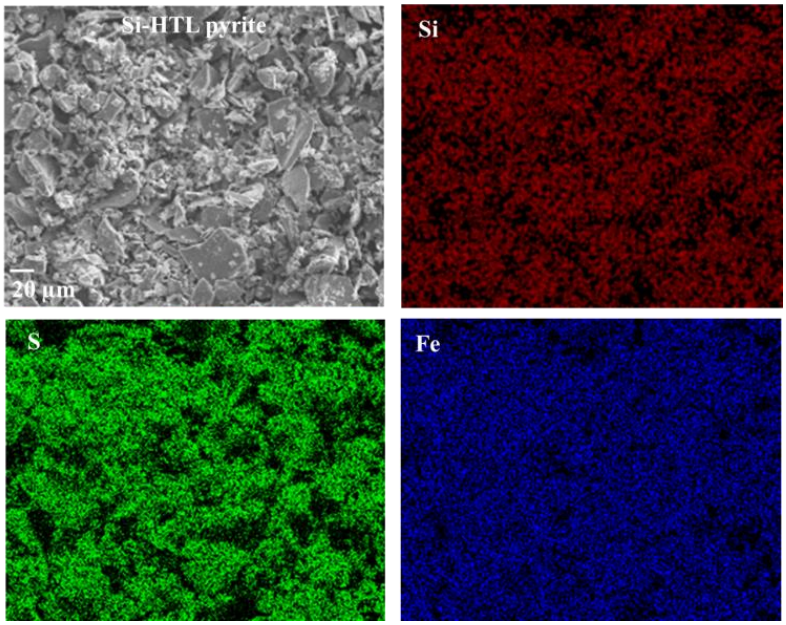

Fig. 2.10. SEM-EDX element mapping of pyrite in presence of Si–HTL (Si–HTL pyrite).

These figures show that silica was present on the pyrite surfaces of the untreated and two treated pyrite samples, but the silica densities of the treated pyrite samples were much higher than that of the untreated sample. The Si contents of the untreated pyrite, Si–Cat-treated pyrite, and Si–HTL-treated pyrite samples were 0.21%, 1.08% and 3.26%, respectively. These results confirm that silica adsorption occurred, and silica coatings were formed on the surfaces of the treated pyrite samples.

The high silica density of Si–HTL pyrite was probably caused by the formation of a silica polymer, as reported by Zhang and Evangelou (1998), and Fytas and Bousquet (2002). At pH > 4 (the pH of Si–HTL was 4.34), the ferric hydroxide precipitated on the pyrite surface reacts with Si-containing species (Eq. 2.1) to form a ferric hydroxide–silica barrier.

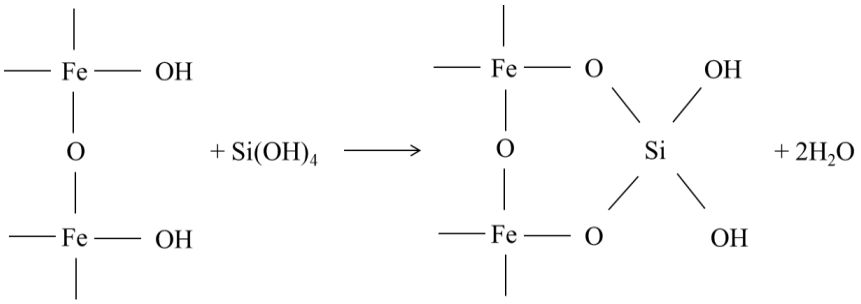

(2.1)

The silica polymer formed in Eq. (2.1) may act as receiving sites for subsequent silica precipitation, as follows:

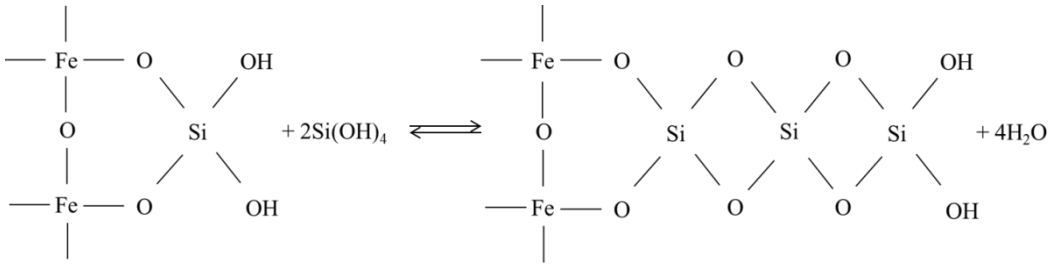

(2.2)

This may result in the formation of negatively charged, open-framework silica polymers that can either flocculate on or coat the pyrite.

The FTIR in Fig. 2.11 show that FTIR spectra, obtained using FT-IR-670 Plus (JASCO, Tokyo, Japan [accumulation, 100 times; resolution, 4 cm^{-1}; detector, triglycine sulfate (TGS); wave numbers, 400–4000 cm^{-1}]), of the untreated and treated pyrite samples differ in the region 1475–1517 cm^{-1} and at 1559 cm^{-1}, the peaks assigned to C-C stretching in the aromatic ring; the peak at 1690 cm^{-1} indicates C=O stretching in an aromatic ketone. The peaks at 2865 and 2937 cm^{-1} represent C-H stretching in alkanes; and the shoulder at around 2974 cm^{-1} represents C-H stretching in an aromatic. It is suggested that the spectra indicate adsorption of a quinone compound on the pyrite surface after oxidative decomposition of the Si–Cat complex, with release of metal ions. The presence of quinone is consistent with equilibrium reaction (1.16),

which shows that silica and quinone are both adsorbed on the pyrite surface, in a silica-quinone layer.

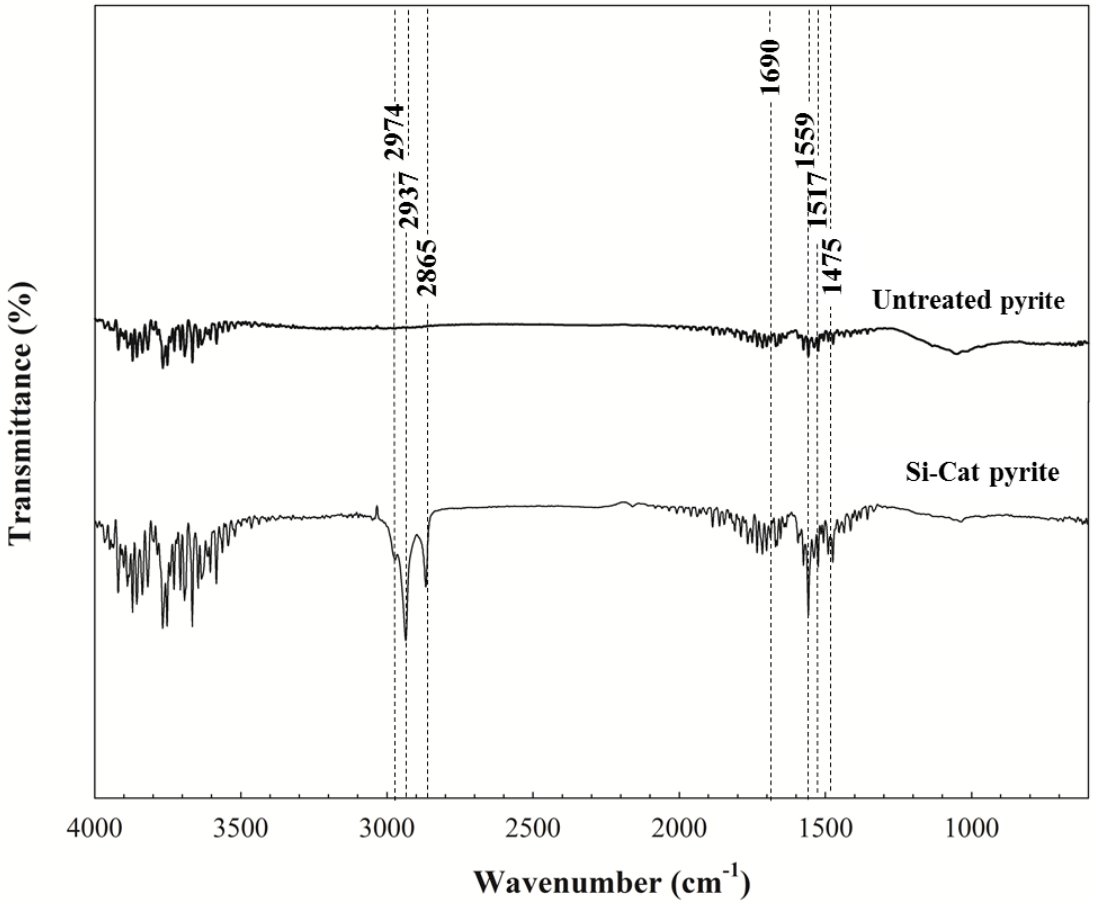

Fig. 2.11. FTIR spectra of untreated and Si–Cat-treated pyrite samples.

Figure 2.12 and 2.13 indicates the images of AFM and DFM for untreated and Si–Cat treated pyrite.

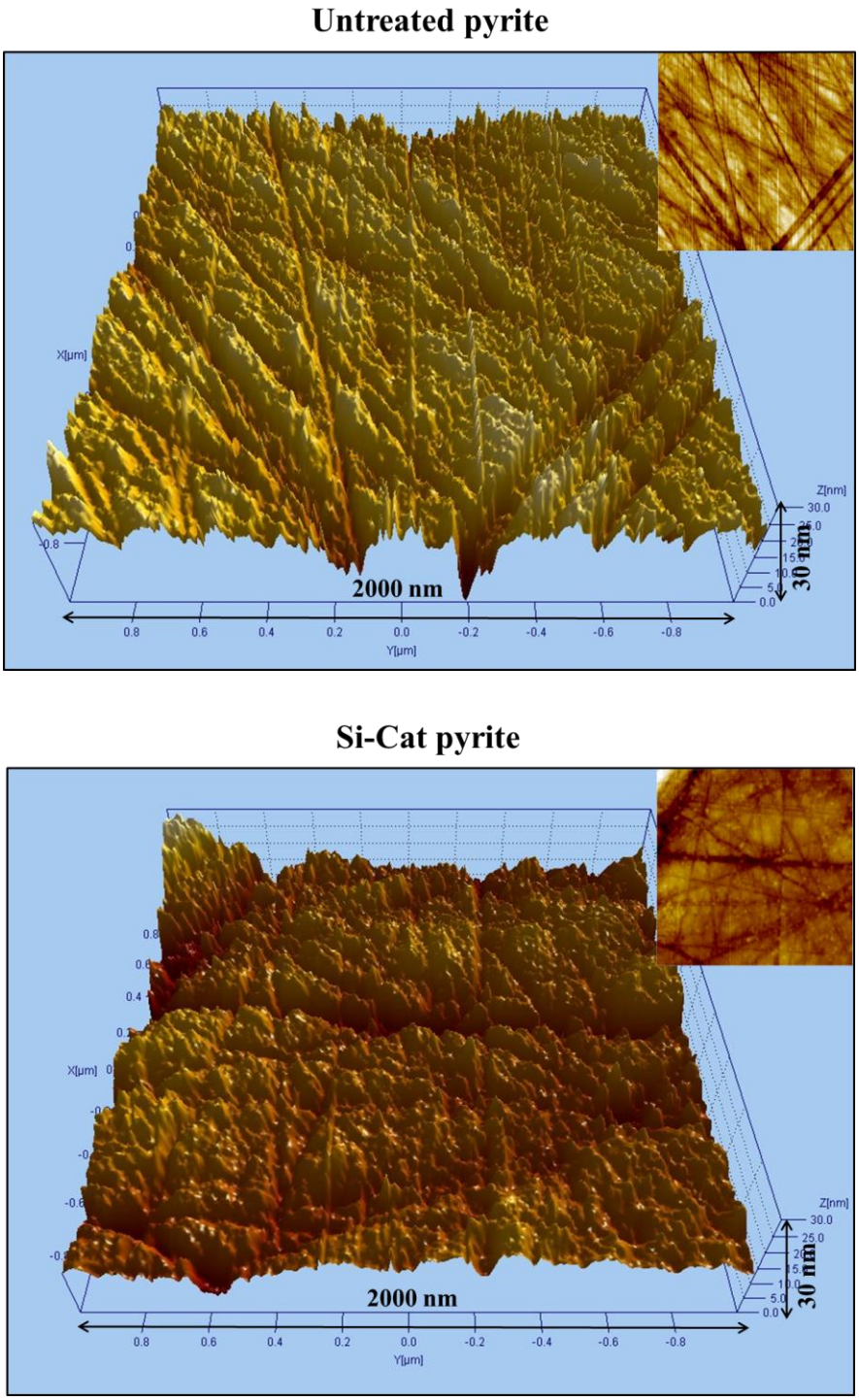

Fig. 2.12. AFM images of untreated and Si–Cat pyrite.

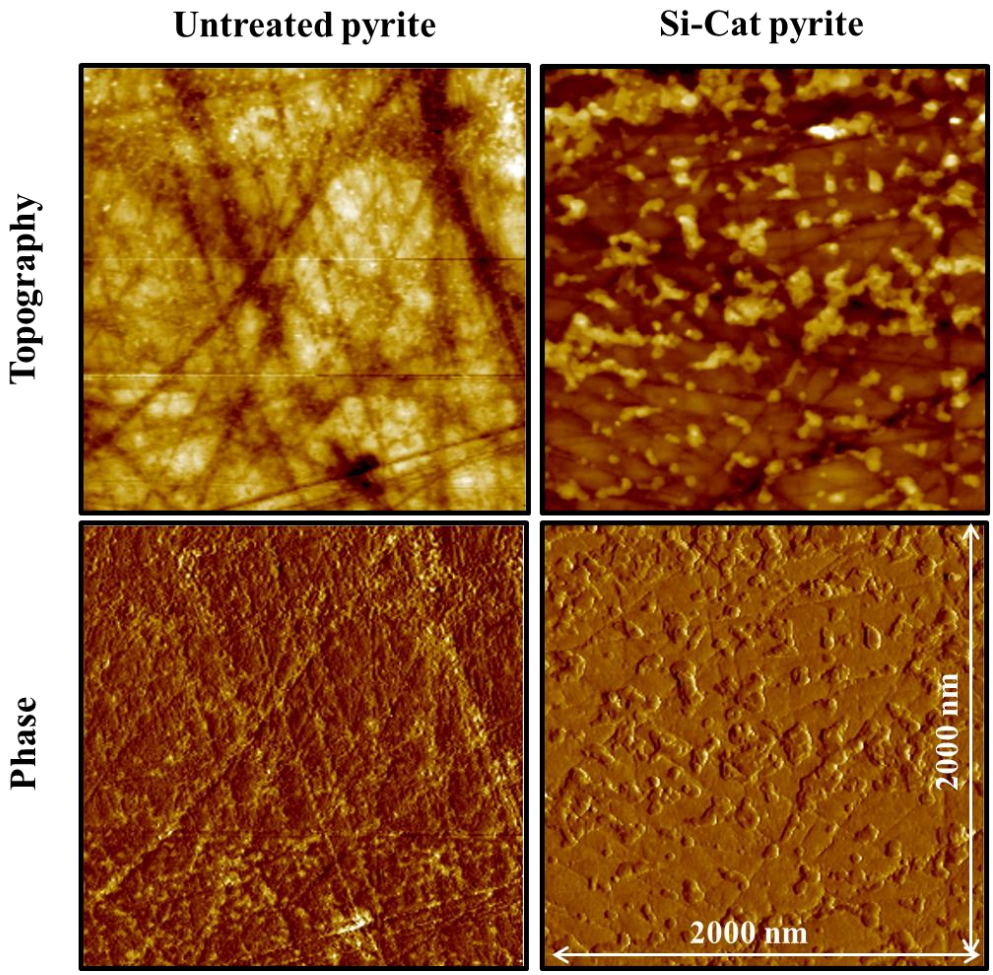

Fig. 2.13. DFM (topography and phase) images of untreated and Si–Cat pyrite.

Table 2.4. Average surface roughness calculated from Fig. 2.12.

	Average surface roughness (nm)
Untreated pyrite	1.528
Si–Cat pyrite	2.705

As shown in Fig. 2.12 and Table 2.4, although these roughness is nano-meter scale, untreated pyrite was smooth and became rough after Si–Cat treatment. This indicates the deposition of substances on the surface of treated pyrite. This phenomenon supported by DFM images (Fig. 2.13) that show the differences between untreated and

Si–Cat-treated pyrite. Without Si–Cat treatment, the deposition was not observed on the pyrite surface; therefore, scratches indicating fresh mineral can be seen clearly. Meanwhile, after Si–Cat treatment, deposition was observed and covered the scratches on the surface of treated pyrite. It is suggested that this deposition is a silica–quinone coating.

2.4. Conclusions

The present study investigated the use of HTL from LRC to suppress pyrite oxidation, to develop a process for controlling the formation of AMD. The results of dissolution and theoretical evaluation, microscopy, and spectroscopy led to the following conclusions.

1) Dissolution tests showed that treatment of pyrite with HTL and a silicon reagent gives a lower ferric ion concentration than those obtained using Si–Cat reagents and untreated pyrite.
2) Based on dissolution tests, Si–HTL coating layer shows better barrier properties than Si–Cat coating layer. This showed that the ability of Si–HTL to suppress pyrite oxidation is higher than that of Si–Cat. This is because HTL contains not only catechol, but also phenol and other phenol derivatives, which increase the reducing, sterilization, and complexation abilities.
3) The coating layer reduces the reactivity of iron on the surface and provides a barrier to bacterial attachment.
4) Theoretical chemical reaction constraints allow for the formation of silicon oxide or hydroxide layers on the pyrite surface during treatment with a solution consisting of silicate mixed with organic materials such as those in HTL.

5) Morphological analyses by using SEM-EDX, AFM, and DFM showed the deposition on the surface of treated pyrite and it was silica rich. The FTIR spectra indicate the adsorption of a quinone compound on the pyrite surface after oxidative decomposition of Si–Cat complex. It is suggested that silica and quinone are both adsorbed on the pyrite surface, in a silica–quinone layer, which can suppress pyrite oxidation.

References

Blazsó, M., Jakab, E., Vargha, A., Székely, T., Zoebel, H., Klare, H., Keil, G., 1986. The effect of hydrothermal treatment on a Merseburg lignite. Fuel 65, 337-341. doi:10.1016/0016-2361(86)90292-9

Crundwell, F.K., 2003. How do bacteria interact with minerals?. Hydrometallurgy 71, 75-81. doi:10.1016/S0304-386X(03)00175-0

Fowler, T.A., Holmes, P.R., Crundwell, F.K., 2001. On the kinetics and mechanism of the dissolution of pyrite in the presence of *Thiobacillus ferrooxidans*. Hydrometallurgy 59, 257-270. doi:10.1016/S0304-386X(00)00172-9

Fytas, K., Bousquet, P., 2002. Silicate micro-encapsulation of pyrite to prevent acid mine drainage, CIM Bulletin 95, pp. 1063.

He, W., Li, G., Kong, L., Wang, H., Huang, J., Xu, J., 2008. Application of hydrothermal reaction in resource recovery of organic wastes. Resour. Conserv. Recy. 52, 691-699. doi:10.1016/j.resconrec.2007.11.003

Jha, R.K.T., Satur, J., Hiroyoshi, N., Ito, M., Tsunekawa, M., 2008. Carrier-Microencapsulation using Si–catechol complex for suppressing pyrite floatability. Miner. Eng. 21, 889-893. doi:10.1016/j.mineng.2008.02.011

Jha, R.K.T., Satur, J., Hiroyoshi, N., Ito, M., Tsunekawa, M., 2012. Suppression of Pyrite Oxidation by Carrier Microencapsulation using Silicon and Catechol. Miner. Process. Extr. M. 33, 89-98. doi:10.1080/08827508.2011.562946

Karagöz, S., Bhaskar, T., Muto, A., Sakata, Y., Oshiiki, T., Kishimoto, T., 2005. Low-temperature catalytic hydrothermal treatment of wood biomass: analysis of liquid products. Chem Eng J. 108, 127-137. doi:10.1016/j.cej.2005.01.007

Mursito, A.T., Hirajima, T., Sasaki, K., Kumagai, S., 2010. The effect of hydrothermal dewatering of Pontianak tropical peat on organics in wastewater and gaseous produtcs. Fuel 89, 3934-3942. doi:10.1016/j.fuel.2010.06.035

Racovalis, L., Hobday, M.D., Hodges, S., 2001. Effect of processing conditions on organics in wastewater from hydrothermal dewatering of low rank coal. Fuel 81, 1369-1378. doi:10.1016/S0016-2361(02)00024-8

Ross, D.S., Loo, B.H., Tse, D.S., Hirschon, A.S., 1991. Hydrothermal treatment and the oxygen functionalities in Wyodak coal. Fuel 70, 289-295. doi:10.1016/0016-2361(91)90115-Q

Sasaki, K., Tsunekawa, M., Ohtsuka, T., Konno, H., 1995. Confirmation of a sulfur-rich layer on pyrite after oxidative dissolution by Fe(III) ions around pH 2. Geochim. Cosmochim. Acta 59, 3155-3158. doi:10.1016/0016-7037(95)00203-C

Satur, J., Hiroyoshi, N., Tsunekawa, M., Okamoto, H., 2007. Carrier-Microencapsulation for preventing pyrite oxidation. Int. J. Miner. Process. 83, 116-124. doi:10.1016/j.minpro.2007.06.003

Savage, P.E., 1999. Organic Chemical Reactions in Supercritical Water. Chem. Rev. 99, 603-621. doi:10.1021/cr9700989

Silverman, M.P., Lundgren, D.G., 1959. Studies on the chemoautotrophic iron bacterium *Ferrobacillus ferrooxidans*. I. An improved medium and harvesting procedure for securing high cells yields. J. Bacteriol. 77, 642-647.

Timpe, R.C., Mann, M.D., Pavlish J.H., Louie, P.K.K., 2001. Organic sulfur and hap removal from coal using hydrothermal treatment. Fuel Process Technol. 73, 127-141. doi:10.1016/S0378-3820(01)00201-6

Zhang, Y.L., Evangelou, V.P., 1998. Formation of ferric hydroxide-silica coatings on pyrite and its oxidation behavior. Soil Sci. 163, 53-62.

CHAPTER 3

Electrochemical Behavior of Resultant Encapsulating Layer of Silicate Coating

Electrochemistry is the study of the chemical response of a system to an electrical stimulation. As semi-conductor, pyrite surface is subject to vary electrochemical processes such as reduction-oxidation reactions and adsorption. These electrochemical processes can be investigated by electrochemical methods that offer a different perspective than other techniques where the responses of a system depend on potential, current, charge and time. In this chapter, three different electrochemical methods, namely, potential polarization, chronoamperometry, and electrochemical impedance spectroscopy were used to investigate the electrochemical behavior of pyrite oxidation suppression in the presence of silicate coating.

3.1. Introduction

Pyrite poses the properties of semi-conductor, and when oxygen and other oxidizing ions are present, the mineral surface is subject to vary electrochemical processes such as reduction-oxidation reactions and adsorption. These electrochemical oxidations not only have an important effect on geochemical process, such as ore geochemistry (Lindsay et al., 2009) and environmental geochemistry (Seal et al., 2008), but they also broadly affect the exploitation and use of sulfide minerals by human beings (Giannetti et al., 2006; Kocabağ and Güler, 2007).

To better understand the electrochemical behavior of pyrite, the most vital thing is to understand its electrochemical interaction mechanisms. In most electrochemical techniques, data are collected using a three-electrode cell that consists of a reference, counter, and working electrode. The working electrode is the sample of interest being studied, while the reference electrode may be, for example, a saturated calomel electrode, silver/silver chloride, etc. No current, or electricity, flows through the reference electrode. Instead it only serves as a reference with a known and constant potential. The third element in the electrochemical cell is the counter electrode, to which the current is allowed to flow. The three electrodes are connected to a potentiostat, an instrument which controls the potential of the working electrode and measures the resulting current. In one typical electrochemical experiment, a potential is applied to the working electrode and the resulting current measured then plotted versus time. In another, the potential is varied and the resulting current is plotted versus the applied potential.

The different combinations of parameters and working electrode types make for a long list of methods. In this study, electrochemical behavior of pyrite oxidation

suppression by Si–Cat complex was evaluated using three different electrochemical methods, namely, potential polarization, chronoamperometry, and electrochemical impedance spectroscopy.

3.1.1. Potential polarization

In potential polarization, the electrode potential is varied at a constant rate throughout the scan and the resulting current is measured. The applied potential is plotted on the x-axis and the resulting current on the y-axis. All potentials are specified in relation to the reference electrode.

3.1.2. Chronoamperometry

When a potential step large enough to cause an electrochemical reaction is applied to an electrode, the current changes with time. The study of this current response as a function of time is called Chronoamperometry.

Chronoamperometry is a useful tool for determining diffusion coefficients and for investigating kinetics and mechanisms.

3.1.3. Electrochemical impedance spectroscopy (EIS)

One of the basic concepts related to electrochemical behaviors is the concept of electrical resistance. This concept is well known and is defined by Ohm's law. Resistance is the ability of a circuit to resist the flow of current, mathematically expressed as

$$R = \frac{V}{I} \tag{3.1}$$

where *R* is resistance in ohm, *V* is voltage in volt, and *I* is current in ampere. However, this relationship is limited to only one circuit element, the ideal resistor. In the real world, circuit elements exhibit much more complex behavior that lead the use of impedance (*Z*), a more general circuit parameter.

Electrochemical impedance is usually measured by applying an AC potential to an electrochemical cell and then measuring the current through the cell. The technique where the cell or electrode impedance is plotted *vs*. frequency is called electrochemical impedance spectroscopy (EIS) (Bard and Faulkner, 2001).

Electrochemical impedance spectroscopy is an important technique in applied electrochemistry and material science. It is a powerful method to investigate the mechanisms of electrochemical reactions by analyzing a current response to the small AC of potential with variable frequency. EIS has proven to be a valuable test method for the electrochemical characterization of the protective organic coating on metals (Deflorian et al., 1994; Thompson and Campbell, 1994).

In an electrical circuit, impedance, *Z*, is related to voltage and current by Ohm's Law:

$$Z = \frac{V(t)}{I(t)} \tag{3.2}$$

where *V(t)* and *I(t)* are the time dependent voltage and current, respectively (Lvovich, 2012).

Impedance includes information on the phase difference that occurs between voltage and current. Impedance can be separated into a real portion, which is the in-phase component associated with energy loss, and imaginary portion which is the 90° out-of-phase component associated with storing electrical energy (Lvovich, 2012).

Electrochemical impedance is normally measured using a small excitation signal. In this study, sinusoidal voltages are applied and the resulting time-dependent current are measured. The voltage can be expressed as:

$$V(t) = V_A sin(2\pi f t) = V_A sin(\omega t) \quad (3.3)$$

where V_A is the voltage amplitude [V], f is the frequency [Hz], t is the time [s], and ω is the angular frequency ($\omega = 2\pi f$) [rad/s]. The current response to a sinusoidal potential will be a sinusoid at the same frequency but shifted in phase between 0 to –π/2 rads. The equation for the current response is (Lvovich, 2012):

$$I(t) = I_A sin(\omega t + \theta) \quad (3.4)$$

where I_A is the current amplitude [A] and θ is the shift in phase [rads]. Figure 3.1 shows a plot of the current response to a sinusoidal voltage input. Depending on the circuit, the current will either lead or lag the voltage (Lvovich, 2012). In Fig. 3.1 the current is leading the voltage by the phase shift θ.

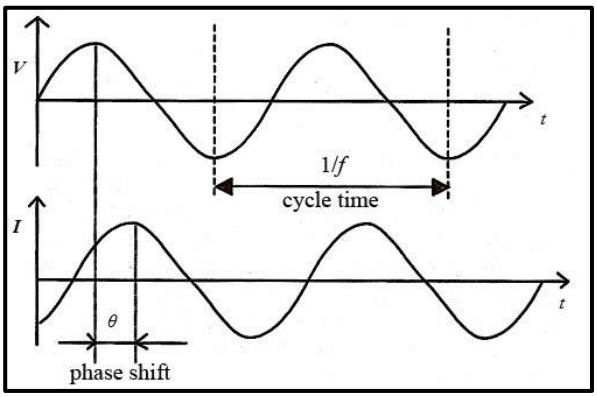

Fig. 3.1. Current response to a sinusoidal voltage input at a given frequency (Lvovich, 2012).

The voltage function and current function can be expressed as the complex relationship

$$V(t) = V_A\, e^{j\omega t} \quad (3.5)$$

$$I(t) = I_A\, e^{j\omega t - j\theta} \tag{3.6}$$

where j is the imaginary number ($j = \sqrt{-1}$). Using equation 3.2, 3.5, and 3.6, the impedance equation can be written as (Lvovich, 2012):

$$Z = Z_A e^{j\theta} = Z_A(cos\theta + jsin\theta) \tag{3.7}$$

where the last relationship is determined using Euler's equation. Equation 3.7 can be separated into real and imaginary components as follows (Lvovich, 2012):

$$Z_{real} = Z_A cos\theta = Z' \tag{3.8}$$

$$Z_{img} = Z_A sin\theta = Z'' \tag{3.9}$$

$$Z = Z' + jZ'' \tag{3.10}$$

Impedance can also be expressed equivalently by using its magnitude (Lvovich, 2012):

$$|Z| = \sqrt{(Z')^2 + (Z'')^2} \tag{3.11}$$

And a phase angle (Lvovich, 2012)

$$\theta = tan^{-1}\frac{Z''}{Z'} \tag{3.12}$$

In this study, impedance will be described in terms of its real and imaginary components and/or its magnitude and phase angle.

3.1.3.1. Circuit Elements

Equivalent circuit analysis is a useful method that helps in understanding the electrochemical system. In the equivalent circuit, each element presents an impedance behavior.

Resistance (*R*) is an element that only presents the real part of the impedance. Hence, the voltage and current are always in phase with each other. From the definition, resistance is frequency independent ($R = V/I = Z$ (Impedance)). In the electrochemical system, *R* is used to describe several phenomena: (1) electrolyte resistance, (2)

polarisation resistance, (3) charge transfer resistance (Orazem and Tribollet, 2008; Cao and Zhang, 2002).

Capacitance (*C*) is an element that provides the imaginary part of the impedance and is a function of frequency as presented in equation 3.13. From the equation, impedance of capacitance is inversely proportional to the frequency. Unlike a resistor, the current of capacitor is shifted -90° to its voltage.

$$Z = \frac{1}{j\omega C} \tag{3.13}$$

Inductance (*L*) is an element which is attributed to the relaxation reactions or adsorption processes to produce intermediate reaction products (Ghasemi et al., 2010). The impedance of inductance is:

$$Z = j\omega L \tag{3.14}$$

From the above equation, inductance is dependent upon frequency. Similar to capacitance, inductance provides only imaginary impedance and its current is shifted +90° compared to its voltage.

Additional elements were developed and applied to describe complex electrochemical phenomena, such as constant-phase element (CPE) and Warburg diffusion element (Orazem and Tribollet, 2008). CPE is an element used to represent a frequency independent distribution. The definition of CPE is shown as follows:

$$Z(\omega) = \frac{1}{Q(j\omega)^{\alpha}} \tag{3.15}$$

where *Q* is a numerical value, which depends on the empirical constant α. When α = 1, $Z(\omega)$ describes the impedance of capacitance, and *Q* is an ideal capacitance (*C*); when α = 0, $Z(\omega)$ describes a resistor; and when α = -1, $Z(\omega)$ describes the impedance of inductance, and *Q* presents an inductance (*L*).

CPE is used in the equivalent circuit analysis in several situations, to describe (1) surface roughness and heterogeneities (Kerner and Pajkossy, 1998), (2) electrode porosity (Lasia, 1995), (3) inhomogeneous reaction rates on the surface (Kim et al., 2003), (4) a varying thickness or composition of a coating (Schiller and Strunz, 2001) and (5) non-uniform current distribution (Jorcin et al., 2006).

The Warburg element is used to model diffusion. Two different Warburg elements W_O and W_S were developed to describe unlimited (infinite) and constrained (finite) conditions of diffusion, respectively.

Table 3.1. Summarize the typical circuit elements that are used when modelling EIS results.

Table 3.1. Circuit elements

Component	Equivalent element	Impedance (Z)
Resistor	R (ohm)	R
Capacitor	C (F, or ohm^{-1}s)	$1/j\omega C$
Inductor	L (H, or ohm s)	$j\omega L$
Constant Phase Element (CPE)	Q (ohm^{-1}s$^{\alpha}$)	$1/Q(j\omega)^{\alpha}$

3.1.3.2. Nyquist Plot

A Nyquist plot, also called a complex plane impedance diagram, is created when the negative imaginary portion of the impedance equation (Equation 3.10) is plotted on the vertical axis and the real portion is plotted on the horizontal axis [Lvovich, 2012]. Each point on the Nyquist plot is the impedance at one frequency. Figure 3.2 shows a Nyquist plot for a typical $R||C$ circuit. The impedance on the Nyquist plot can be expressed as a vector of length $|Z|$ (Gamry Instrument). The angle between this vector and the horizontal axis commonly called the phase angle, θ.

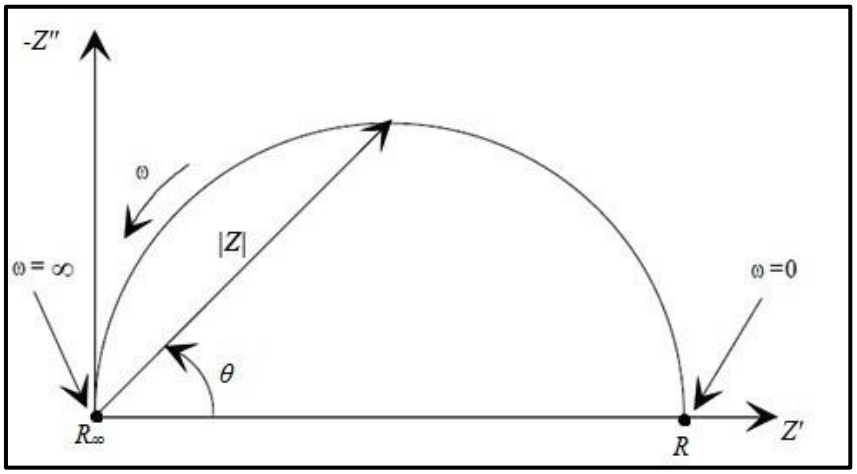

Fig. 3.2. Nyquist plot for *R*||*C* circuit showing impedance vector and other major features (Gamry Instrument).

A Nyquist plot does not always have a single full semi-circle with the center of the semi-circle on the real axis (Macdonald, 1987). There are several reasons for why the center of the semi-circle may be located in the complex plane. One scenario is where the arc does not pass through the origin. This may be caused by $R\infty$ having a value greater than zero and/or the plot containing more arcs at higher frequencies. Another scenario is when the material-electrode system contains distributed elements. This will cause the time constant to no longer equal a single value, but instead be distributed continuously or discretely around a mean time constant. The width of the distribution of a time constant is related to the angle by which a semi-circle arc has been depressed below the real axis.

The shape of a Nyquist plot can reveal if a coating is functioning well or if it has failed. An ideal perfect coating would appear as a vertical line in the Nyquist plot, similar to the one shown in Figure 2-5 [Lvovich, 2012].

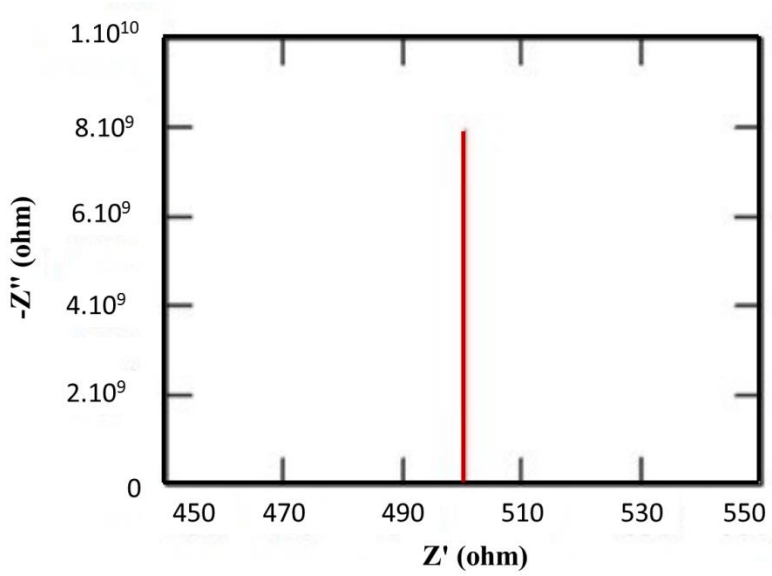

Fig. 3.3. Nyquist plot for an ideal coating (Gamry Instrument).

3.1.3.3. Bode Plot

Another common way to represent EIS data is to use a Bode plot, in which the frequency dependence is shown explicitly (Lvovich, 2012; Loveday et al., 2004). In the Bode plot, the phase angle and the logarithm of the impedance magnitude are plotted against the logarithm of the frequency. Figure 3.4 shows a Bode plot for an ideal coating. The impedance of an ideal coating behaves like a capacitor; it is very high at low frequencies, the impedance plot is a straight line with a slope of -1, and the phase angle is -90° (Gamry Instrument).

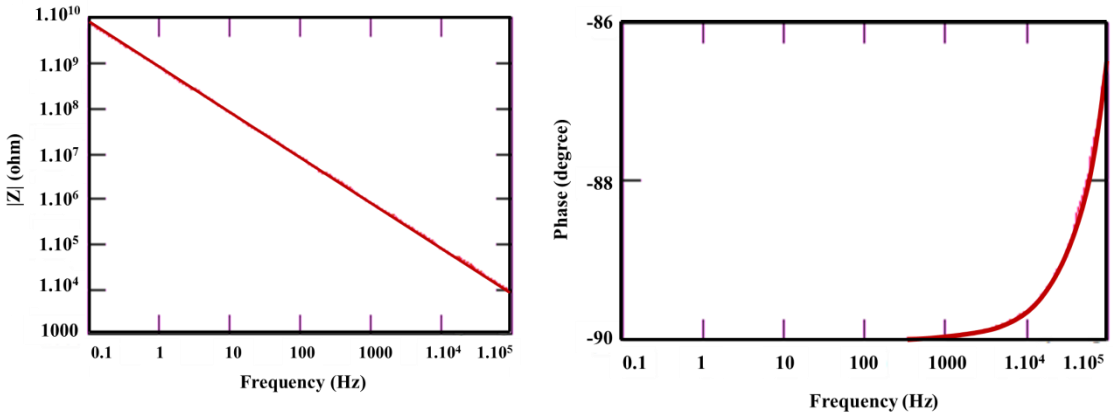

Fig. 3.4. Bode plot of an ideal coating (Gamry Instrument).

3.1.3.4. EIS of coated metals

The system, which consists of a metal covered by an organic film, is generally quite complex and it may consider a large number of different situations. From the complex situation previously described about organic coatings and metal, it clearly emerges that such electrical equivalent circuits will be different with different materials. One of the first works on the EIS characterisation of organic coatings was published by Mansfeld et al. (1982), which suggested a general model of an electrical equivalent circuit from which a large number of other models can be derived. The electrical equivalent circuits for coated metals, which are generally reported in the literature, are shown in Fig. 3.5.

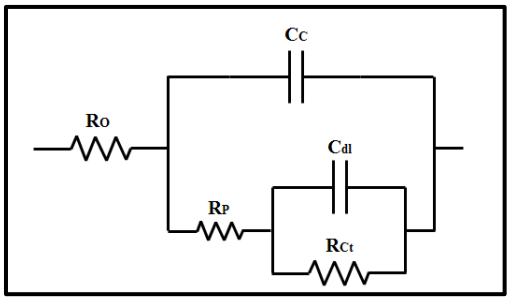

Fig. 3.5. Equivalent circuit model for coated metal (Bonora et al., 1996).

The equivalent circuit model in Fig. 3.5 composed of the electrolyte resistance R_O, coating capacitance C_C, the coating resistance R_p, the double layer capacitance C_{dl}, and the charge transfer resistance R_{ct}.

Numerous works in the area of pyrite electrochemical behavior has been published. Tan et al. (2006) used electrochemical technique to study pyrite oxidation in the presence of carbon coating in cyanide medium. Their results indicate the presence of the carbon coatings significantly increased the oxidation of pyrite and this effect became more pronounced at higher coating thickness. Giannetti et al. (2006) investigated the surface layer growth on natural pyrite in acid medium by using combination of potentiostatic and voltammetric techniques. You et al. (2013) used cyclic voltammogram, Nyquist plot or Tafel test to evaluate the protective effect of polysiloxane coating on pyrite. They conclude that the polyxiloxane coating on pyrite could keep it from oxidation under environmentally relevant conditions.

The final purpose of the EIS characterization of protecting organic coatings is to obtain information about the system properties such as presence of defects, reactivity of the interface, adhesion, barrier properties, etc. In this study, EIS was used to study the surface of pyrite in the presence of a silica-quinone layer.

3.2. Material and methods

3.2.1. Material

Pure crystalline pyrite from the Saimoku mine, Gunma, Japan, was used for electrochemical analysis. The analytical results for the pyrite obtained using inductively coupled plasma atomic emission spectroscopy (ICP-AES Agilent 725, Santa Clara, CA., USA) and X-ray diffraction (XRD Rigaku Ultima IV diffractometer, Tokyo, Japan; Cu

Kα [40 kV, 40 mA] radiation; scanning speed 2 min^{-1}, and scanning step 0.02°), are shown in Chapter 2, Table 2.1 and Fig. 2.1.

For electrochemical analysis, a working electrode was prepared from a pyrite sample by cutting it into cubes with working surfaces of approximately 0.51 cm^2 exposed to the electrolyte. One side of the pyrite electrode was used as the electrode surface and the other side was connected to a copper wire using silver conductive paste and cemented with epoxy resin. The electrode surface was polished with #400 to #4000 emery paper, a Texmet (Buehler, IL, USA) perforated non-woven pad, and a DP-Nap (Struers, Ballerup, Denmark) fine polishing cloth mounted on a plate using 3 μm and 1 μm diamond sprays. After polishing, the electrode was rinsed with ethanol and distilled water to remove polishing residues.

3.2.2. Methods

The pyrite working electrode was immersed in a mixed solution of 2.34 mmol/L sodium metasilicate nonahydrate and 7.00 mmol/L catechol reagents, and also in a solution of Si-HTL (see section 2.2.2.1.), stirred with a magnetic stirrer at 100 rpm for 1 h, air dried for 30 min, and used for electrochemical measurements in 0.10 mol/L sulfuric acid.

The electrochemical measurements were performed using three standard electrode cells consisting of a working electrode, a platinum counter electrode, and a silver/silver chloride electrode (Ag/AgCl; +0.198 V vs. standard hydrogen electrode) as reference electrode. The three electrode cells and sulfuric acid were placed in a glass container. Potential polarization, chronoamperometric, and electrochemical impedance

analysis (EIS) experiments were performed on the untreated and treated pyrite samples (Si–Cat pyrite and Si–HTL pyrite) at room temperature.

The potential polarization and chronoamperometric experiments were performed using an electrochemical analyzer (1205 B, BAS ALS CH Instruments, Tokyo, Japan). Potential polarization was achieved using an open-circuit potential in the anodic direction, at a scan rate of 10 mV/s, and chronoamperometric experiments were performed at 800 mV for 800 s. All the measured potentials were reported with respect to the standard hydrogen electrode. The EIS measurements were performed at an open-circuit potential, using a Solartron Analytical 1280 C instrument (Farnborough, Hampshire, UK), in the frequency range 0.1–20,000 Hz, with a peak-to-peak amplitude of 10 mV. The impedance data were modeled to an equivalent circuit (EC) using the data analysis program Zview® (Scribner Associates, Inc., Southern Pines, NC, USA), using iterative empirical data fitting combined with trial circuit elements chosen based on theoretical considerations.

3.3. Results and discussion

Potential polarization is a change in the equilibrium potential of an electrochemical reaction, and this was used to investigate the oxidation and reduction reactions on the pyrite surface. The potential polarization was determined using the working electrode in a pretreatment solution containing silicate and/or catechol ions, from the open-circuit potential in the anodic direction, at a scan rate of 10 mV/s; the results are shown in Fig. 3.6(a) and 3.6(b).

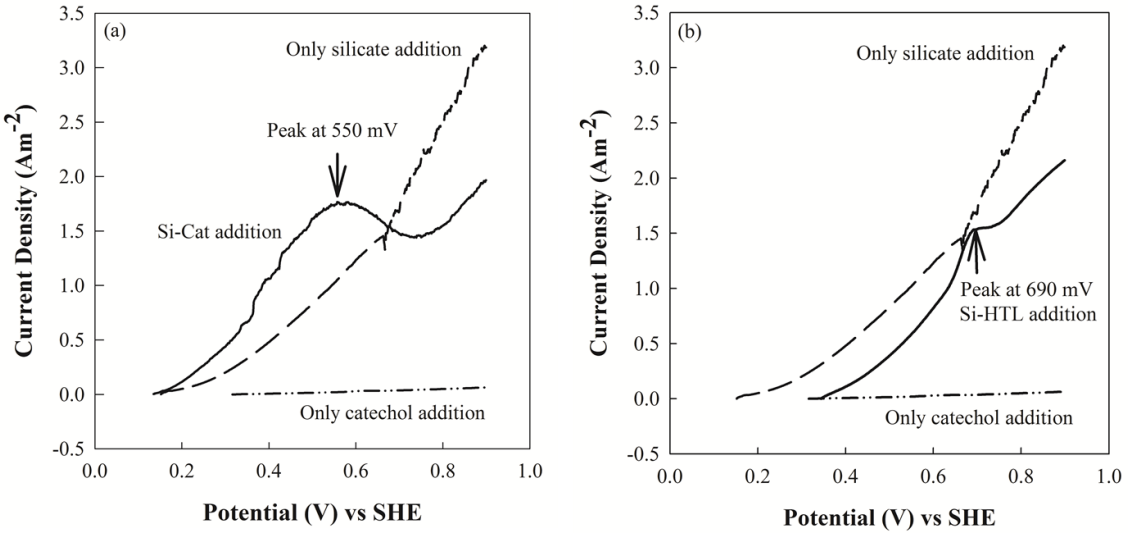

Fig. 3.6. Polarization curves of pyrite electrode in silicate and/or catechol solution: (a) Si–Cat addition, and (b) Si–HTL addition.

Figure 3.6(a) and 3.6(b) show anodic current peaks at 550 mV in the presence of Si-Cat, and at 690 mV in the presence of Si-HTL, respectively. These anodic current peaks were not observed in the absence of the Si-Cat complex. When only silicate solution was used, the current increased with increasing potential, and with catechol solution only, the current was very low. These results suggest that the peaks at 550 and 690 mV correspond to oxidative decomposition of the Si-Cat complex on the pyrite surface as describes in reaction Eqs. 1.16-1.21.

Chronoamperometric experiments were performed to measure the oxidation rates of pyrite with and without pretreatment. These experiments were performed at 800 mV for 800 s. The results are shown in Fig. 3.7 as curves of current density against time. The current density is the anodic current of the working electrode in the working area of 0.51 cm^2. The anodic currents of the treated pyrite samples (Si–Cat pyrite and Si–HTL pyrite) are lower than that of the untreated pyrite. Because the anodic current represents the oxidation rate, the lower anodic currents of the treated pyrite samples mean that the

oxidation rates of these samples are lower than that of the untreated pyrite. These results indicate that pyrite oxidation can be suppressed simply by pretreatment for 1 h with either Si–Cat or Si–HTL.

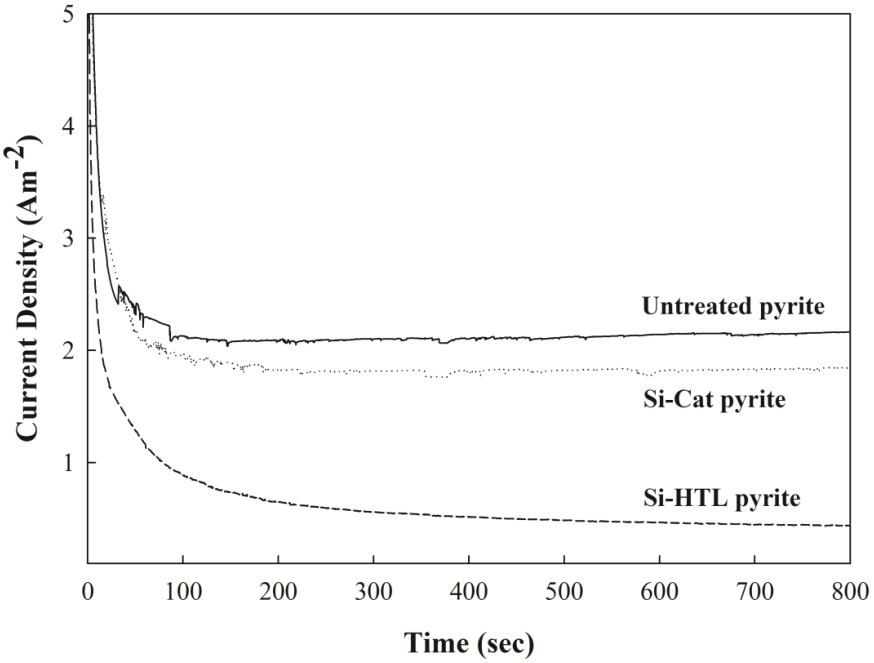

Fig. 3.7. Chronoamperometric curves of untreated pyrite, Si–Cat pyrite, and Si–HTL pyrite in 0.1 M H_2SO_4.

EIS is often used to obtain information on the properties of systems, such as the presence of defects, reactivities of interfaces, adhesion, and barrier properties. In this work, EIS was used to study the surface of pyrite in the presence of a silica-quinone layer.

The impedance is expressed as a complex number, composed of a real part, Z', and an imaginary part, Z''. A Nyquist plot is obtained by plotting the real part on the x-axis and the imaginary part on the y-axis of a chart.

The EIS complex plane plots (Nyquist plots) of the untreated and treated pyrite samples are shown in Fig. 3.8.

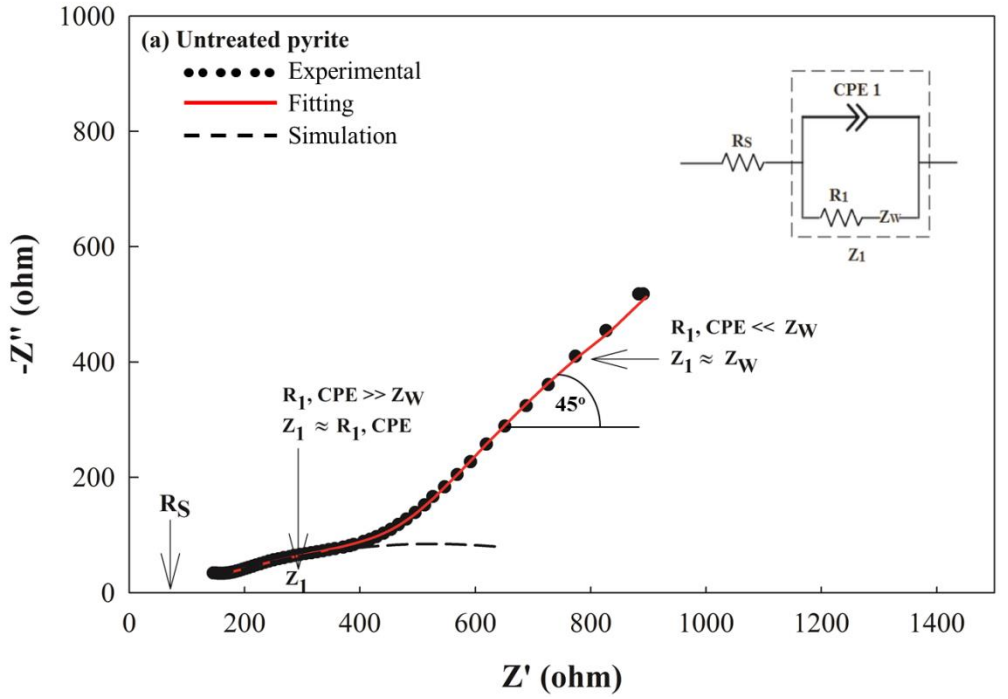
(a) Untreated pyrite
Experimental
Fitting
Simulation
CPE 1
Rs
R1
Zw
Z1
R1, CPE << ZW
Z1 ≈ ZW
45°
R1, CPE >> ZW
Z1 ≈ R1, CPE
RS
Z1
-Z'' (ohm)
Z' (ohm)
0
200
400
600
800
1000
1200
1400

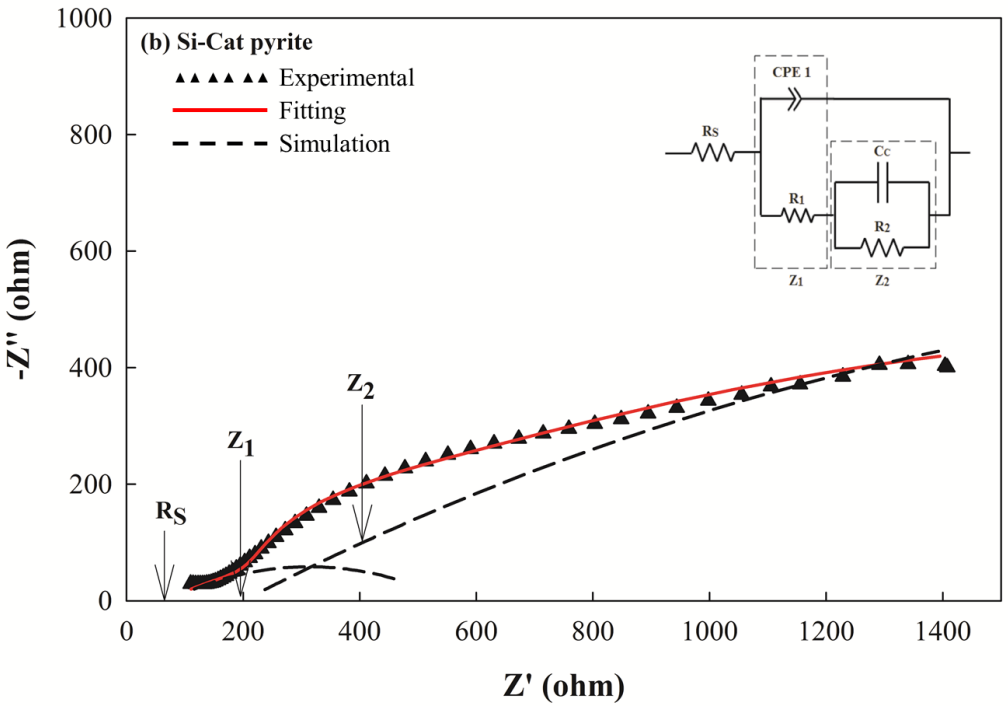
(b) Si-Cat pyrite
Experimental
Fitting
Simulation
CPE 1
Rs
Cc
R1
R2
Z1
Z2
RS
Z1
Z2
-Z'' (ohm)
Z' (ohm)
0
200
400
600
800
1000
1200
1400

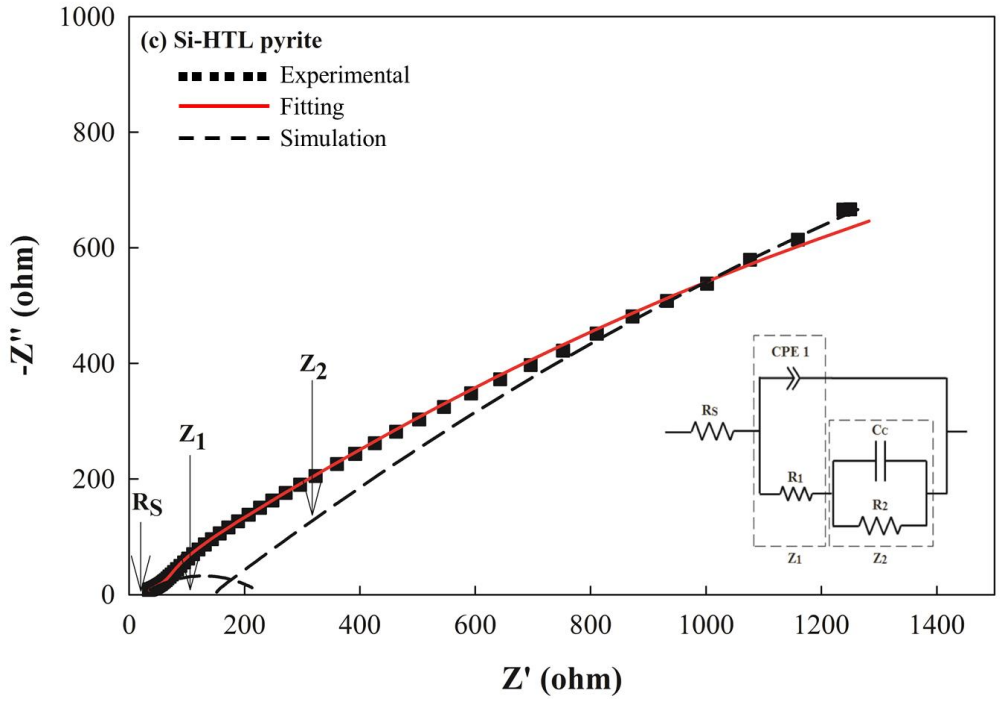

Fig. 3.8. EI spectra of (a) untreated pyrite, (b) Si–Cat pyrite, and (c) Si–HTL pyrite. These Nyquist plots show curves for three types of data: experimental, fitting, and simulation results. Experimental results (black symbols) represent the original data from the EIS measurements. The observed EI spectra were analyzed by fitting to an EC model; the EC models are shown inside the Nyquist plot. The results of fitting to the EC models (solid red lines) were used to simulate the ideal circuit (black dashed lines).

The Nyquist plot for the untreated pyrite has a semi-circular shape characteristic of electrode reactions that are controlled by charge-transfer resistance (Mendiratta et al., 1996), but the plots for the treated pyrite samples (Si–Cat pyrite and Si–HTL pyrite) are almost linear. The semi-linear curve represents the small portion of the semi-circle that is associated with charge transfer resistance; the large portion is related to the resistance of the coating layer. These results suggest that the coating layers on the treated pyrite samples have high resistance values. Because the resistance of the examined coating

layer (in this case the silica–quinone coating) is proportional to its resistivity, a high resistance means that the layer resistivity is also high.

Based on the observations made for all the systems, two ECs were proposed to fit the impedance spectra of the untreated and treated pyrite samples (inset in Fig. 3.8). The EIS experimental data can be fitted and interpreted well based on these two circuits.

The Nyquist plot of the untreated pyrite (Fig. 3.8a) shows a combination of kinetic and diffusion processes (the linear part of the EI spectrum is typical of Warburg impedance). In this case, the oxidizing agents (e.g., O_2 and Fe^{3+}) or products (e.g., Fe^{2+}) diffuse across the electrode interface. At high frequencies, the Warburg impedance is low; at lower frequencies, diffusion occurs deeper into the material and the Warburg impedance causes the Nyquist plot of the EC model to become a straight line at the end of the plot, making an angle of 45° to the real impedance axis (Liu et al., 2011a).

The simplest EC model for characterizing the untreated pyrite (inset in Fig. 3.8a) includes the electrolyte solution resistance (R_s), the charge-transfer resistance of the pyrite (R_1), a constant phase element (CPE), and the Warburg diffusion resistance (Z_w). A CPE was used in this model instead of a capacitor to compensate for the rough and porous electrode.

When this EC model is applied to the treated pyrite samples (a coating immersed in an electrolyte), R_s represents the resistance of the electrolyte solution between the reference electrode tip and the surface of the coating. The resistance of the electrolyte can be observed at the highest frequency data point ($\omega \rightarrow \infty$) in the complex plot. The charge-transfer resistance of the pyrite (R_1) is associated with the resistance (R_2) and capacitance (C_C) of the coating layer; the values vary depending on the composition of the coating.

For the treated pyrite samples, as shown in Fig. 3.8(b) and 3.8(c), after fitting to the EC model and simulation, the Nyquist plot of the impedance consisted of two semi-circles, Z_1 and Z_2 (the plot for the untreated pyrite had only one semi-circle), with higher total impedance values compared with that of untreated pyrite. The higher total impedance values indicate that another product layer has grown on the electrode surface, after either Si–Cat or Si–HTL treatment. It is suggested that this reflects the formation of a silica–quinone layer on the surfaces of the treated pyrite samples.

The calculated parameters of the EC elements for the untreated and treated pyrite samples are listed in Table 3.2. Low chi-squared (χ^2) values, which represent the sum of quadratic deviations between experimental and calculated data divided by the calculated data, are presented, suggesting that the experimental data are fitted well with the proposed circuit models.

Table 3.2. EC element parameters obtained by fitting experimental impedance data for untreated and treated pyrite samples with EC models shown in inset in Fig. 3.8.

Parameter	Untreated pyrite		Si–Cat pyrite		Si–HTL pyrite	
	Value	Error %	Value	Error %	Value	Error %
R_s/ohm	70.16	4.559	66.48	4.904	23.53	1.417
R_1/ohm	911.2	8.139	482.4	3.475	209.3	3.560
CPE1-T	0.0007	5.591	0.0005	3.210	0.0007	0.987
CPE1-P	0.2338	2.994	0.3018	2.612	0.3910	0.568
R_2/ohm	-	-	3247	9.018	5542	4.356
C_C/μF	-	-	5.3436E-6	4.888	3.2023E-6	3.817
$\chi^2/10^{-4}$	1.063		3.191		4.171	

The R_S values of the untreated and treated Si–Cat pyrite samples were similar, but R_S decreased by a factor of 3 when Si–HTL was used instead of Si–Cat. This can be explained based on the hydrothermal treatment process. During hydrothermal treatment, heat and pressure cause decomposition of oxygen functional groups, e.g., by dehydration, reduction, and decarboxylation, resulting in HTL containing soluble organic materials such as catechol and inorganic components such as sodium, potassium, and calcium (Mursito et al., 2010; Favas and Jackson, 2003; Baker et al., 1986). The resistivities of the solutions resulting from the Si–Cat pyrite and Si–HTL pyrite systems were around 25 and 6.67 ohm m, respectively. These results show that the Si–HTL pyrite system gives a more conductive coating, indicating that a much larger amount of inorganic ions was released into the electrolyte solution during the EIS measurements, and this increases the ionic strength of the solution. As the ionic strength of the solution increases, the solution resistance (R_S) decreases.

The R_1 value of the untreated pyrite is much higher than those of the treated pyrite samples. This may be because the R_1 value of the untreated pyrite includes the resistances of the pyrite itself and also of the passivation film (i.e., elemental sulfur, polysulfide, or metal-deficient layers on the surface of the untreated pyrite). The passivation film is normally recognized on the surface of sulfide minerals (Alhberg and Broo, 1996; Liu et al., 2011b; Peters, 1984; Todd et al., 2003). For the treated pyrite samples, in which a silica-quinone coating layer was present, the coating layer may include the passivation film on the pyrite surface, causing R_1 to be lower than that of the untreated pyrite.

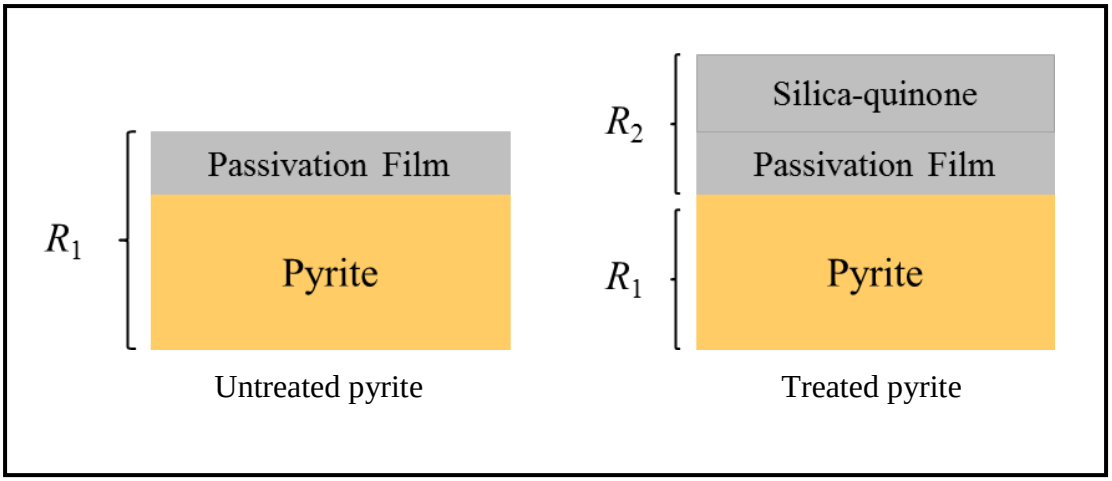

Fig. 3.9. Schematic figure of pyrite passivation film.

The radius of the semi-linear curve and the R_2 value for the Si–HTL pyrite are larger than those for the Si–Cat pyrite. This shows that the Si–HTL coating layer has better barrier properties and confirms the results of the dissolution tests (Chapter 2) and chronoamperometric measurements, which showed that the ability of Si–HTL to suppress pyrite oxidation is higher than that of Si–Cat. This is because HTL contains not only catechol, but also phenol and other phenol derivatives, which increase the reducing, sterilization, and complexation abilities.

Bode plots of untreated pyrite, Si–Cat pyrite, and Si–HTL pyrite are shown in Fig. 3.10; they show the magnitude (in ohms) and phase (in degrees) of the system response as a function of frequency.

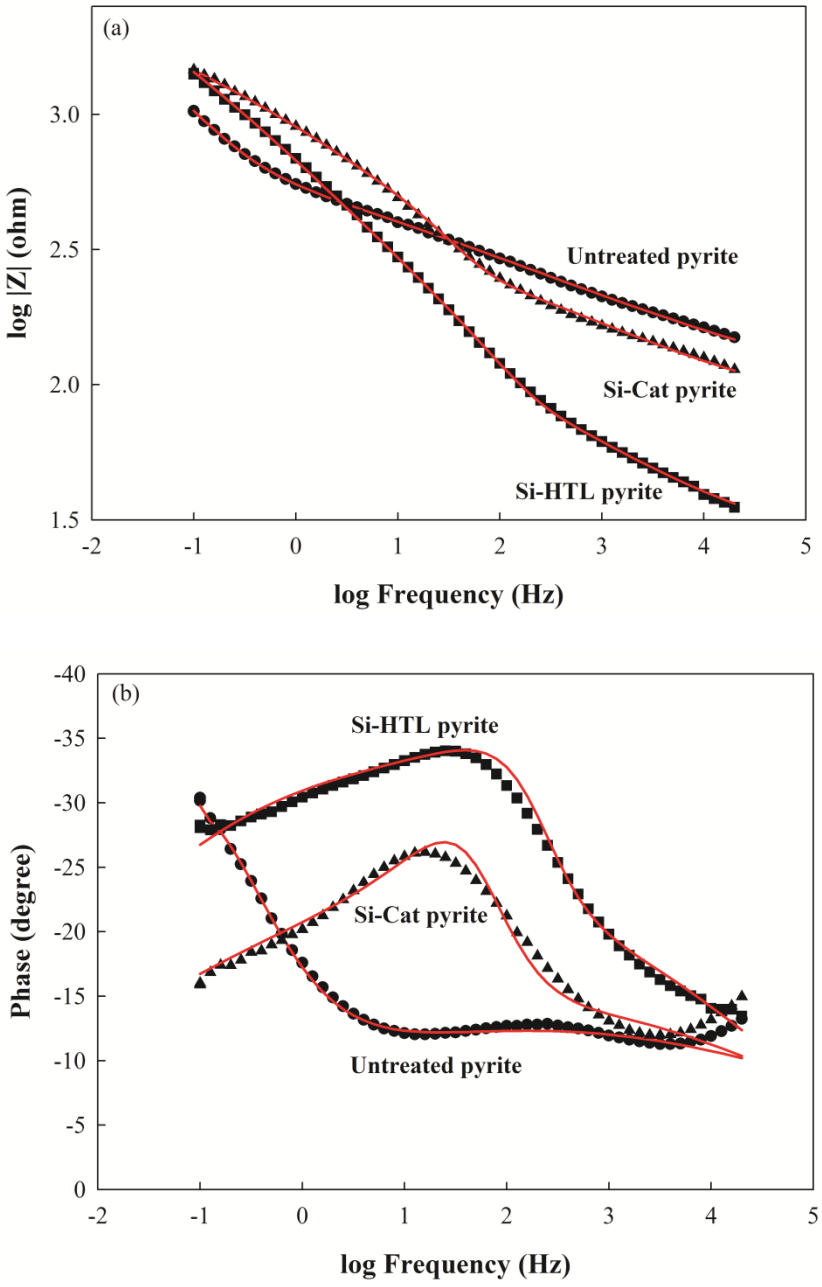

Fig. 3.10. Bode plots of untreated pyrite, Si–Cat pyrite, and Si–HTL pyrite showing system responses as function of frequency: (a) magnitude in ohms, and (b) phase in degrees. These plots show curves for two types of data: experimental results (black symbols) and the results of fitting to the EC models shown inside the Nyquist plots (solid red lines).

The treated pyrite samples have similar $|Z|$ values, of the order of $10^{3.2}$ ohm at low frequency, as shown in the Bode plot in Fig. 3.10(a); this is higher than the value for untreated pyrite. The higher impedance values of the coated samples imply that the coating layer protects the pyrite surface against oxidation.

The quality of the coating is maximum at the point at which the phase angle is maximum (Totten and MacKenzie, 2003). Figure 3.10(b) shows that the phase angle of the time constant of Si–Cat pyrite is lower than that of Si–HTL pyrite and shifted to the lower frequency. As reported by Szczygieł and Kołodziej (2005), the shifting of the phase angle of the time constant to lower frequencies shows an indication of electrolyte diffusion through the coating layer that cause the charge transfer reaction. This means the coating layer produced by Si–HTL treatment has better barrier properties than that produced by Si–Cat. This result is consistent with the explanation given above.

3.4. Conclusions

The electrochemical behaviors of pyrite oxidation suppression in the presence of silicate coating were investigated by using three different electrochemical methods. Potential polarization results of the treated pyrite samples showed the oxidative decomposition of the Si–Cat complex and formation of an encapsulating layer at 690 mV for Si–HTL pyrite and 550 mV for Si–Cat pyrite. It also showed by chronoamperometry results that the anodic currents (represent the oxidation rate) of the treated pyrite samples are lower than that of the untreated pyrite.

Nyquist plot simulations from EIS experiments showed that the treated pyrite samples consisted of two semi-circular curves, Z_1 and Z_2 (the plot for the untreated pyrite had only one semi-circle), with higher total impedance values compared with that

of untreated pyrite. It is suggested that this reflects the formation of a silica-quinone layer on the surfaces of the treated samples that suppress pyrite oxidation. Meanwhile, Bode plot simulations showed the shifting of the phase angle of the time constant of Si–Cat treated pyrite to lower frequencies, indicating electrolyte diffusion occurs through the coating layer. Therefore, coating layer produced by Si–HTL treatment has better barrier properties than that produced by Si–Cat.

References

Alhberg, E., Broo, A.E., 1996. Electrochemical reaction mechanisms at pyrite in acidic perchloric solutions. In: Doyle, F.M., Richardson, P.E.,Woods, R. (Eds.), Electrochemistry in Mineral and Metal Processing IV. The Electrochemical Society, Pennington, New Jersey, pp. 119–130.

Baker, G.G., Sears, R. E., Maas, D.J., Potas, T.A., Willson, W.G., Farn, S.A., 1986. Hydrothermal preparation of low-rank coal-water fuel slurries. Energy 11, 1267-1280. doi:10.1016/0360-5442(86)90064-2

Bard, A.J., Faulkner, L.R., 2001. Electrochemical Methods, Fundamental and Applications, second ed. John Wiley & Sons., Inc., New York.

Bonora, P.L., Deflorian, F., Fedrizzi, L., 1996. Electrochemical impedance spectroscopy as a tool for investigating underpaint corrosion. Electrochim. Acta 41, 1073-1082. doi:10.1016/0013-4686(95)00440-8

Cao, C., Zhang, J., 2002. An Introduction to Electrochemical Impedance Spectroscopy. Science press, Beijing.

Deflorian, F., Miskovic-Stankovic, V.B., Bonora, P.L., Fedrizzi, L., 1994. Degradation of Epoxy Coatings on Phosphatized Zinc-Electroplated Steel. Corrosion 50, 438-446. doi: http://dx.doi.org/10.5006/1.3293522

Favas, G., Jackson, W.R., 2003. Hydrothermal dewatering of lower rank coals. 2. Effects of coal characteristic for a range of Australian and international coals. Fuel 82, 59-69. doi:10.1016/S0016-2361(02)00191-6

Gamry Instruments. Basics of electrochemical impedance sprectroscopy. 18 January 2014. http://www.gamry.com/application-notes/EIS/basics-of-electrochemical-impedance-spectroscopy/

Ghasemi, A., Raja, V.S., Blawert, C., Dietzel, W., Kainer, K.U., 2010. The role of anions in the formation and corrosion resistance of the plasma electrolytic oxidation coatings. Surface & Coatings Technol. 204, 1469-1478.

Giannetti, B.F., Almeida, C.M.V.B, Bonilla, S.H., 2006. Electrochemical kinetic study of surface layer growth on natural pyrite in acid medium. Colloids Surf., A 272, 130-138. doi:10.1016/j.colsurfa.2005.07.018

Jorcin, J.B., Orazem, M.E., Pebere, N., Tribollet, B., 2006. CPE analysis by local electrochemical impedance spectroscopy. Electrochim. Acta 51, 1473-1479. doi:10.1016/j.electacta.2005.02.128

Kerner, Z., Pajkossy, T., 1998. Impedance of rough capacitive electrodes: the role of surface disorder. J. Electroanal. Chem. 448, 139-142. doi:10.1016/S0022-0728(98)00025-4

Kim, C.H., Pyun, S.I., Kim, J.H., 2003.*An investigation of the capacitance dispersion on the fractal carbon electrode with edge and basal orientations.* Electrochim. Acta 48, 3455-3463. doi:10.1016/S0013-4686(03)00464-X

Kocabağ, D., Güler, T., 2007. Two-liquid flotation of sulphides: an electrochemical approach. Miner. Eng. 20, 1246–1254. doi:10.1016/j.mineng.2007.05.005

Lasia, A., 1995. Impedance of porous electrodes. J. Electroanal. Chem. 397, 27-33. doi:10.1016/0022-0728(95)04177-5

Lindsay, M.B.J., Condon, P.D., Jambor, J.L., Lear, K.G., Blowes, D.W., Ptacek, C.J., 2009. Mineralogical, geochemical, and microbial investigation of a sulfide-rich tailings deposit characterized by neutral drainage. Appl. Geochem. 24, 2212-2221. doi:10.1016/j.apgeochem.2009.09.012

Liu, Y., Dang, Z., Lu, G., Wu, P., Feng, C., Yi, X., 2011a. Utilization of electrochemical impedance spectroscopy for monitoring pyrite oxidation in the presence and absence of *Acidithiobacillus ferrooxidans*. Miner. Eng. 24, 833-838. doi:10.1016/j.mineng.2011.03.002

Liu, Y., Dang, Z., Wu, P., Lu, G., Shu, X., Zheng, L., 2011b. Influence of ferric iron on the electrochemical behavior of pyrite. Ionics 17, 169–176. doi:10.1007/s11581-010-0492-4

Loveday, D., Peterson, P., Rodgers, B., 2004. Evaluation of Organic Coatings with Electrochemical Impedance Spectroscopy. Part 1: Fundamentals of Electrochemical Impedance Spectroscopy. Gamry Instruments .

Lvovich, V.F., 2012. Impedance Spectroscopy: Applications to Electrochemical and Dielectric Phenomena. John wiley & Sons. Hoboken, New Jersey.

Macdonald, J.R. (ed.), 1987. Impedance Spectroscopy: Emphasizing Solid Materials and Systems. John Wiley & Sons. Toronto.

Mansfeld, F., Kendig, M., Tsai, S., 1982. Evaluation of corrosion behavior of coated metals with AC impedance measurements. Corrosion 38, 478. doi:10.5006/1.3577363

Mendiratta, N.K., Yoon, R.-H., Richardson, P.E., 1996. Electrochemical impedance spectroscopy of freshly fractured and polished pyrite electrodes, Proceedings of the 189th Electrochemical Society Meeting, May 5-10, Los Angeles, CA, pp. 155-156.

Mursito, A.T., Hirajima, T., Sasaki, K., 2010. Upgrading and dewatering of raw tropical peat by hydrothermal treatment. Fuel 89, 635-641. doi:10.1016/j.fuel.2009.07.004

Orazem, M.E., Tribollet, B., 2008. Electrochemical Impedance Spectroscopy. John Wiley & Sons, Inc., Hoboken, New Jersey.

Peters, E., 1984. Electrochemical mechanisms for decomposing sulfide minerals. In: Richardson, P.E., Srinivasan, S., Woods, R. (Eds.), Electrochemistry in Minerals and Metal Processing. The Electrochemical Society, Pennington, New Jersey, pp. 343–361.

Schiller, C.A., Strunz, W., 2001. The evaluation of experimental dielectric data of barrier coatings by means of different models. Electrochim. Acta 46, 3619-3625. doi:10.1016/S0013-4686(01)00644-2

Seal II, R.R., Hammarstrom, J.M., Johnson, A.N., Piatak, N.M., Wandless, G.A., 2008. Environmental geochemistry of a Kuroko-type massive sulfide deposit at the abandoned Valzinco mine, Virginia, USA. Appl. Geochem. 23, 320–342. doi:10.1016/j.apgeochem.2007.10.001

Szczygieł, B., Kołodziej, M., 2005. Composite Ni/Al_2O_3 coatings and their corrosion resistance. Electrochim. Acta 50. 4188-4195. doi:10.1016/j.electacta.2005.01.040

Tan, H., Feng, D., van Deventer, J.S.J., Lukey, G.C., 2006. An electrochemical study of pyrite oxidation in the presence of carbon coatings in cyanide medium. Int. J. Miner. Process. 80, 153-168. doi:10.1016/j.minpro.2006.03.011

Thompson, I., Campbell, D., 1994. Interpreting nyquist responses from defective coatings on steel substrates. Corr. Sci. 36, 187-198. doi:10.1016/0010-938X(94)90119-8

Todd, E.C., Sherman, D.M., Purton, J.A., 2003. Surface oxidation of pyrite under ambient atmospheric and aqueous (pH = 2 to 10) conditions: electronic structure and mineralogy from X-ray absorption spectroscopy. Geochim. Cosmochim. Acta 67, 881-893. doi:10.1016/S0016-7037(02)00957-2

Totten, G.E., Mackenzie, D.S, 2003. Handbook of Aluminum, Alloy Production and Materials Manufacturing. Marcel Dekker, New York.

You, G., Yu, C., Lu, Y., Dang, Z., 2013. Evaluation of the protective effect of polysiloxane coating on pyrite with electrochemical techniques. Electrochim. Acta 93, 65-71. doi:10.1016/j.electacta.2013.01.098

CHAPTER 4

Mechanism of Pyrite Oxidation Suppression using Silicon-catechol Complex

This chapter describes pyrite oxidation suppression under different conditions via carrier microencapsulation (CME) using Si–Cat complex in order to clarify the mechanism involved in this coating treatment. These treatments resulted in differences in the suppression of pyrite oxidation. The surface characteristics and chemical composition of coating layer was determined by scanning electron microscopy with energy dispersive X-ray spectroscopy (SEM-EDX), Fourier transform infrared spectrometer (FTIR), and X-ray photoelectron spectrometer (XPS). Silica–quinone coating suppression effects were also investigated by chronoamperometry and electrochemical impedance spectroscopy (EIS). In this chapter, possible mechanism of pyrite oxidation suppression is proposed from the results of SEM-EDX, FTIR, and XPS.

4.1. Introduction

Previous study of pyrite oxidation suppression using Si–Cat complex indicated a silica–quinone coating is created and the oxidation rate of pyrite can be suppressed by pretreatment with Si–Cat. However, a more systematic investigation of the silica–quinone coating is needed in order to clarify the mechanisms involved in this coating treatment. To address these issues, the morphological characteristics and chemical composition was determined by scanning electron microscopy with energy dispersive X-ray spectroscopy (SEM-EDX), Fourier transform infrared spectrometer (FTIR), and X-ray photoelectron spectrometer (XPS). Silica–quinone coating suppression effects were also investigated by chronoamperometry and electrochemical impedance spectroscopy (EIS).

4.2. Materials and methods

4.2.1. Materials

4.2.1.1. Pyrite

Crystalline pyrite from Victoria mine, Navajún, La Rioja, Spain was used as experimental material. The analytical results, obtained using X-ray fluorescence (XRF Rigaku ZSX Primus II, Tokyo, Japan) and X-ray diffraction (XRD Rigaku Ultima IV diffractometer, Tokyo, Japan), are shown in Table 4.1 and Fig. 4.1. It can be seen that the sample was identical to pure pyrite.

Table 4.1. Elemental compositions of pyrite sample from Victoria mine, determined using XRF.

Element	Percentage by weight
Fe	47.64
S	49.19
Al	1.46
Cu	0.05
K	0.03
Ni	0.12
Si	1.18

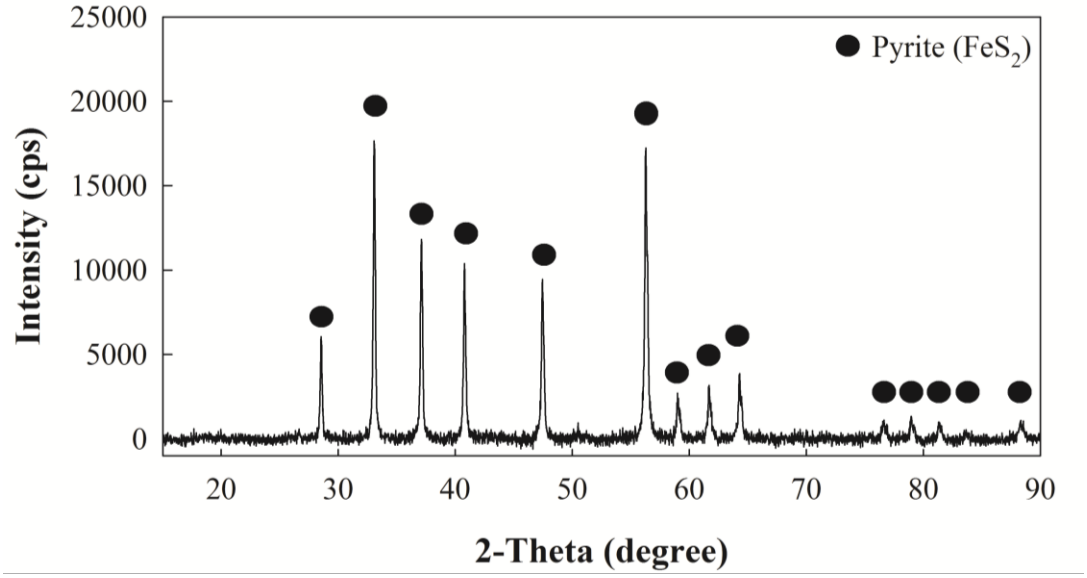

Fig. 4.1. XRD patterns of pyrite sample from Victoria mine.

For surface characteristics (FTIR, SEM-EDX and XPS), a pyrite sample was ground to -38 μm in diameter on an agate mortar in a nitrogen-purged glove. After grinding, the washing method of Sasaki et al. (1995) was adapted to remove the surface oxide. The sample was washed with ethanol in a beaker by an ultrasonic bath for 30 seconds. After removing the supernatant, the pyrite was washed with 1 mol/L nitric acid

solution for one minute, distilled water (two times) and acetone (four times). Finally, the washed pyrite was dried by freeze dehydration.

For electrochemical analysis, a working electrode was prepared from a pyrite sample by cutting it into cubes with working surfaces of approximately 1.10 cm^2 exposed to the electrolyte. One side of the pyrite electrode was used as the electrode surface and the other side was connected to a copper wire using silver conductive paste and cemented with epoxy resin. The electrode surface was polished with #400 to #4000 emery paper, a Texmet (Buehler, Illinois, USA) perforated non-woven pad, and a DP-Nap (Struers, Ballerup, Denmark) fine polishing cloth mounted on a plate using 3 μm and 1 μm diamond sprays. After polishing, the electrode was rinsed with ethanol and distilled water to remove polishing residues.

4.2.1.2. Si–Cat solution

Solution of 7.00 mmol/L catechol ($C_6H_4[OH]_2$) (Wako, special grade) was prepared using ultrapure water. Subsequently, 2.34 mmol/L sodium metasilicate nonahydrate ($Na_2SiO_3 \cdot 9H_2O$) (Wako, special grade) was added to the catechol solution. Solution pH was adjusted to the desired value using HCl and KOH, and used for pyrite surface treatment. This solution referred as silicon–catechol (Si–Cat) complex and used for pyrite treatment

4.2.2. Methods

4.2.2.1. Pretreatment of pyrite and electrochemical analysis

The pyrite working electrode was immersed in the coating solution (see Section 4.2.1.2.), stirred with a magnetic stirrer at 100 rpm. After a predetermined stirring time

(1, 6, and 12 h), the working electrode was air dried for 30 min, and used for electrochemical measurements in 0.10 mol/L sulfuric acid.

The electrochemical measurements were performed using three standard electrode cells consisting of a working electrode, a platinum counter electrode, and an Ag/AgCl reference electrode. The three electrode cells and sulfuric acid were placed in a glass container. Chronoamperometric and electrochemical impedance spectroscopy (EIS) experiments of untreated and treated pyrite samples were performed at room temperature using an electrochemical instrument (Solartron Analytical 1280 C, Hampshire, UK).

Chronoamperometric experiments were carried out at 800 mV for 300 s and all the measured potentials were reported with respect to the standard hydrogen electrode. The EIS measurements were performed at open circuit potential in the frequency range of 0.1–20,000 Hz with peak-to-peak amplitude of 10 mV. The impedance data was modelled to an equivalent circuit (EC) using the data analysis program Zview® (Scribner Associates, Inc., North Carolina, USA), using iterative empirical data fitting combined with trial circuit elements chosen based on theoretical considerations.

4.2.2.2. Pretreatment of pyrite and surface characteristics

In a 250 mL bottle, 10.00 g of washed pyrite sample was added to 100 mL of Si–Cat solution. After predetermined stirring time (1, 6, and 12 h) at 100 rpm and 25°C, the solid residues from each treatment bottle were recovered by filtration and dried by freeze dehydration. Dry solid residue referred as Si–Cat treated pyrite samples.

SEM-EDX analyses were performed using (Keyence VE-9800, Osaka, Japan) and FTIR investigations were performed using FT-IR-670 Plus (JASCO, Tokyo, Japan

[accumulation, 100 times; resolution, 4 cm^{-1}; detector, triglycine sulfate; wave numbers, 400–4000 cm^{-1}]).

XPS analyses were carried out using XPS ESCA 5800F (New York, USA) with Al Kα X-ray source (1486.6 eV) operated at 200 W. The samples were cleaved under vacuum in the sample preparation chamber prior to delivery, without breaking vacuum, to the XPS analysis chamber. The vacuum in the sample preparation chamber is approximately 10^{-8} Torr when the sample is cleaved and the pressure in the analysis chamber is 10^{-9} Torr during the XPS measurements. The samples were first examined in wide scan (80 W of the analyzer pass energy) to identify all the elements present, the various elemental regions were scanned (40 W of the analyzer pass energy) in order to extract information on chemical bonding and oxidation stages. The collected data were analyzed with Casa XPS software (Ver. 2.3.16). Background corrections were made using the Shirley method for the Fe 2p, S 2p, O 1s, and Si 2p spectra (Shirley, 1972). Peak shapes were defined using a Gaussian–Lorentzian function. Binding energy (EB) calibration was based on C 1s at E_B[C1s] = 284.6 eV.

4.3. Results and discussion

4.3.1. Effect of treatment time by silicate coating on pyrite oxidation suppression

Figure 4.2 show chronoamperometric experiments data that completed to measure the oxidation rate of pyrite with and without pretreatment. Pretreatment were conducted initially at pH 9.5 (natural pH of Si–Cat) for 1 h, 6 h, and 12 h. These experiments were measured at 800 mV for 300 s. The average results of two times measurements are shown as curves of current density with time. Current density is the anodic current of the working electrode in the working area of 1.10 cm^2.

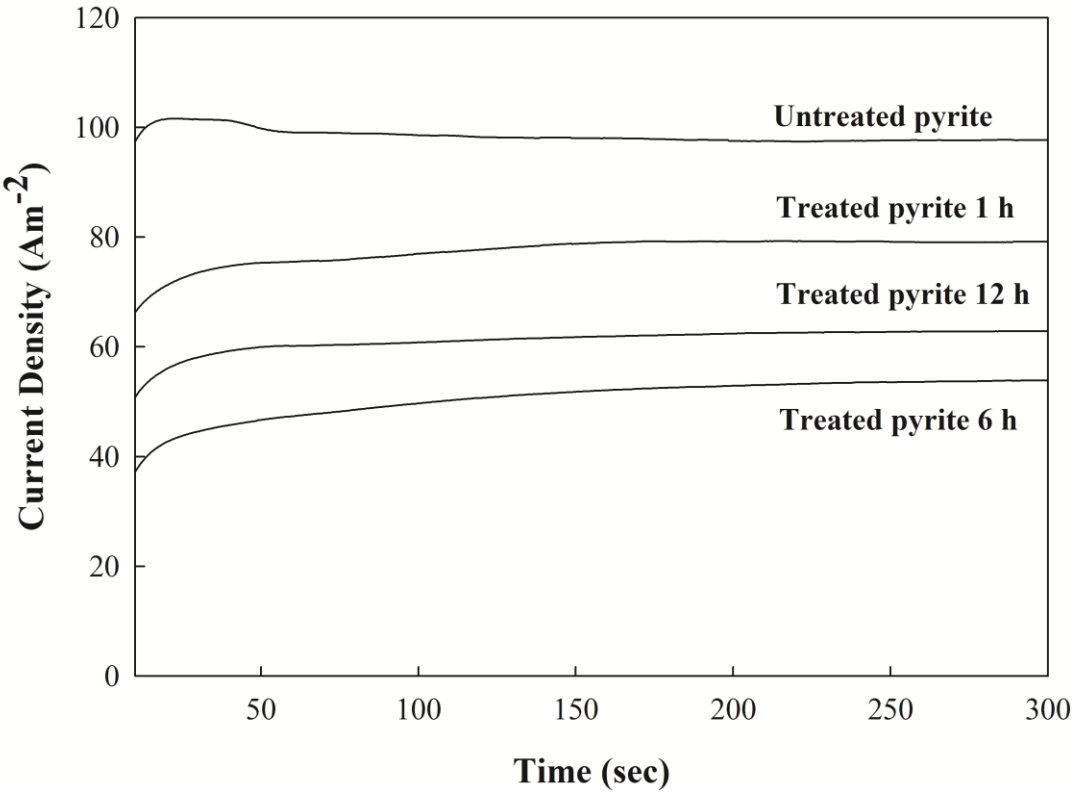

Fig. 4.2. Chronoamperometric curves of untreated and Si–Cat-treated pyrite samples initially pH 9.5 with different treatment time in 0.1 M H_2SO_4.

From these results, the anodic currents of Si–Cat treated pyrite samples (1 h, 6 h, and 12 h) are lower than that of the untreated pyrite. Because the anodic current represents the oxidation rate, the lower anodic currents of Si–Cat treated pyrite samples mean that the oxidation rates of these samples are lower than that of the untreated pyrite. Figure 4.2 show that pyrite sample treated for 6 h has the lowest oxidation rate and largest suppression effect. This result is consistent with the study conducted by Bessho et al. (2011) that showed equilibrium pHs of silica solutions were reached after 6 h of stirring. Pyrite sample treated for 1 h shows the lowest suppression effect. It may be due

to the shorter time that used to complete the coating process. Meanwhile, longer treatment time (12 h) also shows lower suppression effect than 6 h treatment. The reason for this is still unclear. However, after treatment for 12 h, the solution color was darker than it was for the other treatment times. This is possibly caused by the formation of (catecholato)iron(III) complex, $[Fe(C_6H_4O_2)_3]^{3-}$. Catechol can form stable complexes with various di- and tri-valent metal ions such as iron (Schweigert et al., 2001). A basic solution of catechol reacts with iron(III) to give a red (catecholato)iron(III) complex, which becomes black on exposure to air (Anderson et al., 1976). This phenomenon may affect the suppression effect.

4.3.2. Effect of pH in silicate coating on pyrite oxidation suppression

A series of experiments (EIS, SEM-EDX, FTIR, and XPS) was conducted to evaluate the effect of initial pH of Si–Cat complex on pyrite oxidation suppression. EIS is often used to obtain information on the properties of systems, such as the presence of defects, reactivities of interfaces, adhesion, and barrier properties. In this work, EIS was used to study the barrier properties of pyrite surface in the presence of a silica–quinone layer.

Like resistance, impedance is a measure of the ability of a circuit to resist the flow of electrical current. Electrochemical impedance is usually measured by applying an alternating current (AC) potential to an electrochemical cell and then measuring the current through the cell. The technique is based on the measurement of current through an electrode when a sinusoidal potential is applied. The impedance is therefore expressed in terms of magnitude, Z_o (ratio of voltage to current) and a phase shift, ϕ;

composed of a real part, *Z*', and an imaginary part, *Z*". A Nyquist plot is obtained by plotting the real part on the *x*-axis and the imaginary part on the *y*-axis of a chart.

The EIS complex plane plots (Nyquist plots) of pyrite samples are shown in Fig. 4.3.

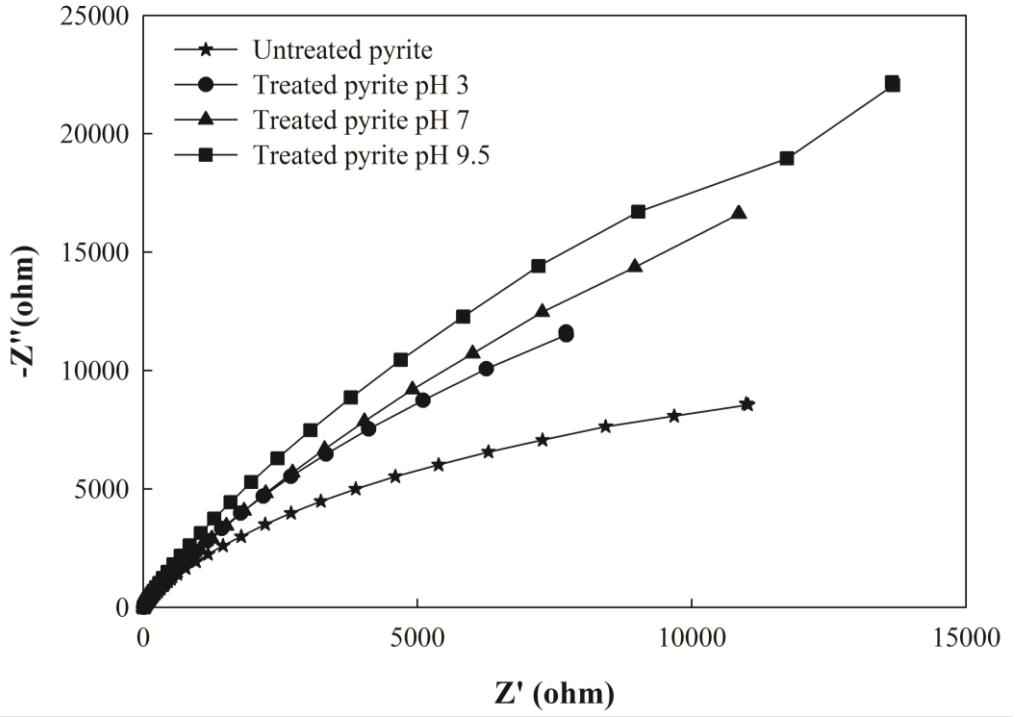

Fig. 4.3. EI spectra of 6 h Si–Cat-treated pyrite samples initially pH 3, 7, and 9.5; compared with untreated pyrite.

The Nyquist plot for the untreated pyrite is a semicircle, and those of treated pyrite samples have larger radius than that of untreated pyrite. The *Z*' value at the starting point of each semicircle indicates solution resistance, and a semicircle shape indicates the impedance of electrode, including both electrode resistance and capacitance (Lvovich, V.F., 2012). The radius of the semicircle represents the resistance of the electrode. The flat semicircle shape indicates that the electrode surface is rough

and contains defects, so for this fitting we used a constant phase element (CPE) instead of a capacitor.

Based on the observations made for all the systems, EC models were proposed to fit the impedance spectra of pyrite samples. The EIS experimental data can be fitted and interpreted well based on the EC models shown in Fig. 4.4. These EC models are same with EC models that used in the previous chapter.

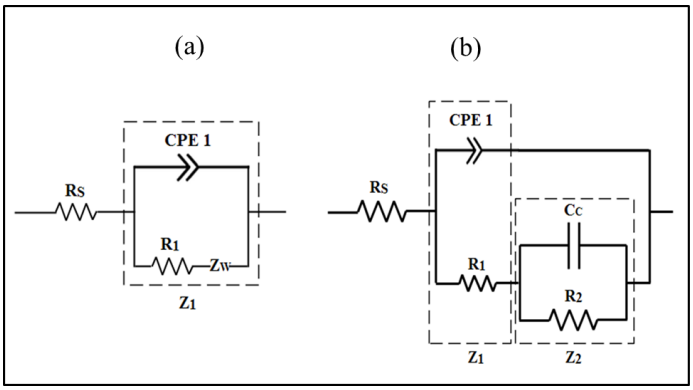

Fig. 4.4. EC models of (a) untreated pyrite, and (b) Si–Cat pyrite.

The simplest EC model for characterizing pyrite samples include the electrolyte solution resistance (R_s), the resistance of the pyrite (R_1), and a constant phase element (CPE). The R_1 is associated with the resistance (R_2) and capacitance (C_C) of the coating layer and their values vary depending on the composition of the coating.

The calculated parameters of the EC elements for untreated and Si–Cat-treated pyrite samples are listed in Table 4.2.

Table 4.2. EC element parameters obtained by fitting experimental impedance data for untreated and 6 h Si–Cat-treated pyrite samples with EC models shown in Fig. 4.4.

Pyrite	R_S, ohm	R_1, ohm	R_2, ohm
Untreated	9.59	1078	-
Treated pH 3	9.35	2.98	58290
Treated pH 7	7.20	4.24	99192
Treated pH 9.5	8.53	2.87	103620

The R_1 value of the untreated pyrite is much higher than those of the treated pyrite samples. As an explanation in Chapter 3, this phenomenon may be because the R_1 value of the untreated pyrite includes the resistances of the pyrite itself and also of the passivation film (i.e., elemental sulfur, polysulfide, or metal-deficient layers on the surface of the untreated pyrite). For the treated pyrite samples, in which a silica-quinone coating layer was present, the coating layer may include the passivation film on the pyrite surface (Fig. 3.9), causing R_1 to be lower than that of the untreated pyrite.

The treated pyrite samples, after fitting to the EC model, show higher total impedance values compared with that of untreated pyrite. These results indicate the coating layer is created on the surface of treated pyrite samples. From the listed R_2 values, 6 h Si–Cat-treated pyrite initially pH 9.5 has larger R_2 value than other treatment conditions which confirm the results of chronoamperometric measurements (effect of treatment time). At pH lower than 9 the formation of Si–Cat complexes might be incomplete as reported by Bartels (1964) and simple hydrolysis may predominate (Correns, 1961). Based on those reports, silica covering layer was not created

completely and the suppression effect was lower than that of Si–Cat-treated pyrite initially pH 9.5. These data also supported by Ultraviolet-visible (UV) absorption spectra studies conducted by Sever and Wilker (2004) that showed that at low pH (<7), catechol is reduced and coordination complexes are dissolved instead of cross linked.

Figure 4.5 show SEM-EDX images of 6 h Si–Cat-treated pyrite samples initially pH 3, 7 and 9.5 compared with untreated pyrite.

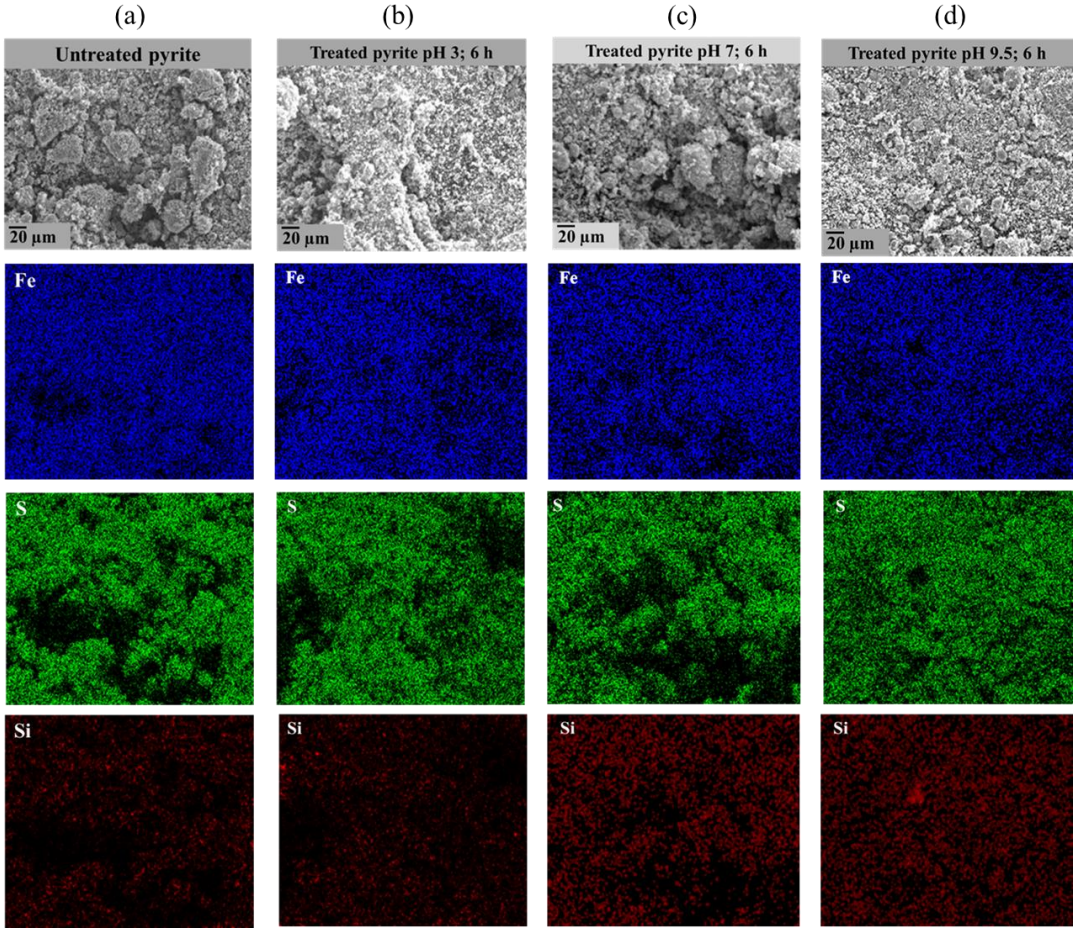

Fig. 4.5. SEM-EDX element mapping of (a) untreated pyrite; 6 hr Si–Cat-treated pyrite initially pH (b) 3, (c) 7, (d) 9.5.

All figures show that silica is present on pyrite surface of untreated and three treated pyrite samples, but the silica densities of the treated pyrite samples are much

higher than that of the untreated sample. Si contents of the untreated pyrite, Si–Cat-treated pyrite initially pH 3, 7 and 9.5 were 0.34%, 0.71%, 1.56% and 2.59%, respectively. These results confirm that silica adsorption occurred, and silica coatings were formed on the surfaces of the treated pyrite samples.

The high silica density of treated pyrite initially pH 7 and 9.5 was probably caused by the formation of a silica polymer, as reported by Zhang and Evangelou (1998) and Fytas and Bousquet (2002). At pH > 4, the ferric hydroxide precipitated on the pyrite surface reacts with Si-containing species to form a ferric hydroxide–silica barrier.

Attenuated total reflectance Fourier transfer infrared spectroscopy (ATR-FTIR) has been used to study the adsorption of Si–Cat complex onto pyrite surface (Fig. 4.6). The presence of quinone was confirmed from the previous study (Yuniati et al., 2014). In the present study, the presence of polymerization (via Si–O–Si linkages) was investigated. Peaks observed at 955–960 cm^{-1} are present in the treated pyrite samples. These absorption peaks correspond to Fe–O stretching of the Fe–O–Si bond (Schwertmann and Thalmann, 1976). The occurrence of Fe–O–Si bonds indicates that Si–OH groups (silanol) reacted with FeOOH on the surface of pyrite. FeOOH is produced on the surface of pyrite from released ferric ion as follows:

$$Fe^{3+} + 2H_2O \rightarrow FeOOH + 3H^+ \quad (4.1)$$

The bonding mode near 1065 cm^{-1} is for the Si–O–C asymmetric stretching mode in a ring link (Bellamy, 1975). This bond shows that the aromatic ring attach to Si–O bond. Besides, significant peaks are observed at 1154–1190 cm^{-1}. According to Carlson and Schwertmann (1981), the peaks observed at 1154–1160 cm^{-1} were assigned to a shift of Si–O–Si in polymerized Si. As the Si–O–Si (siloxanes) chains become

longer or branched, the Si–O–Si absorption becomes broader and more complex. As surface coverage increases with the pH, the presence of polymerized species becomes evident and the peak intensity due to adsorbed silicate shows the highest absorbance for Si–Cat treated pyrite initially pH 9.5.

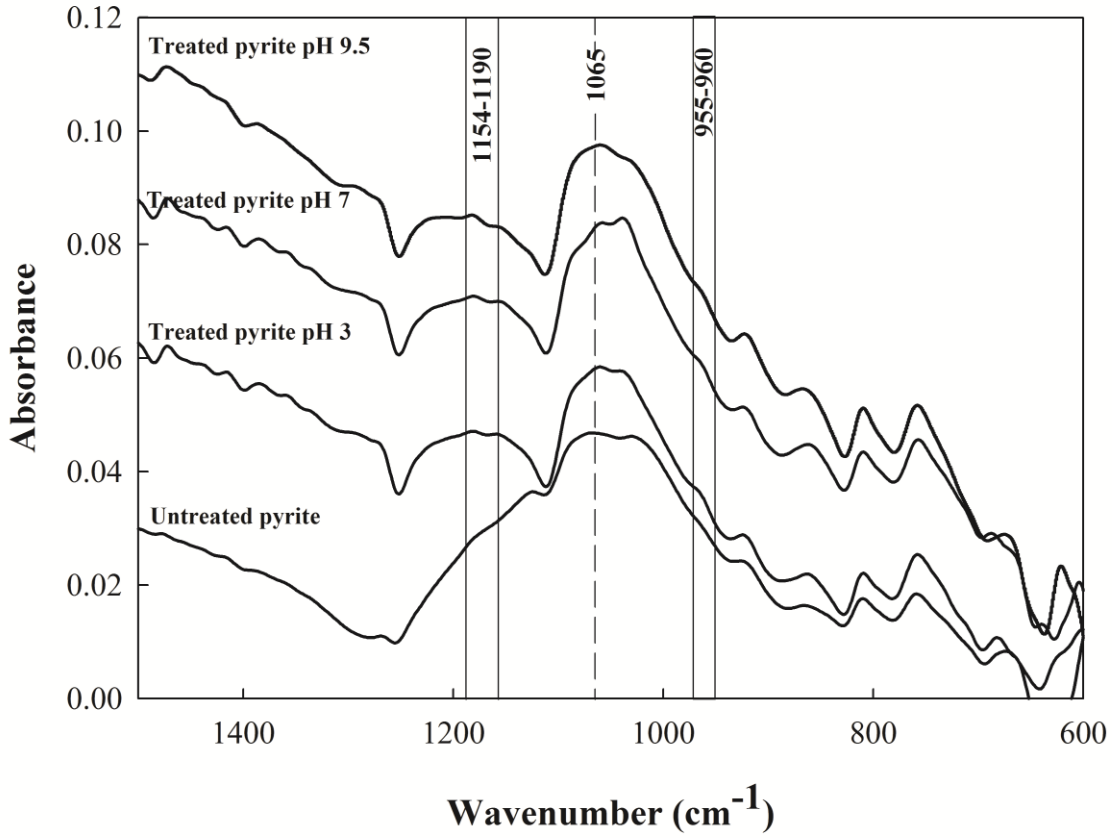

Fig. 4.6. ATR-FTIR spectra of untreated and 6 h Si–Cat treated pyrite samples.

To confirm the surface product, XPS analysis of pyrite samples have been conducted before and after 6 h Si–Cat treatment initially at pH 3, 7 and 9.5. The narrow scanned and corresponding decomposed of Fe 2p, S 2p, and O 1s spectra are shown in Fig. 4.7.

XP-spectra of Fe 2p, S 2p, O 1s, and Si 2p for untreated pyrite and treated pyrite samples were analyzed by peak separation and the results are summarized in Table 4.3.

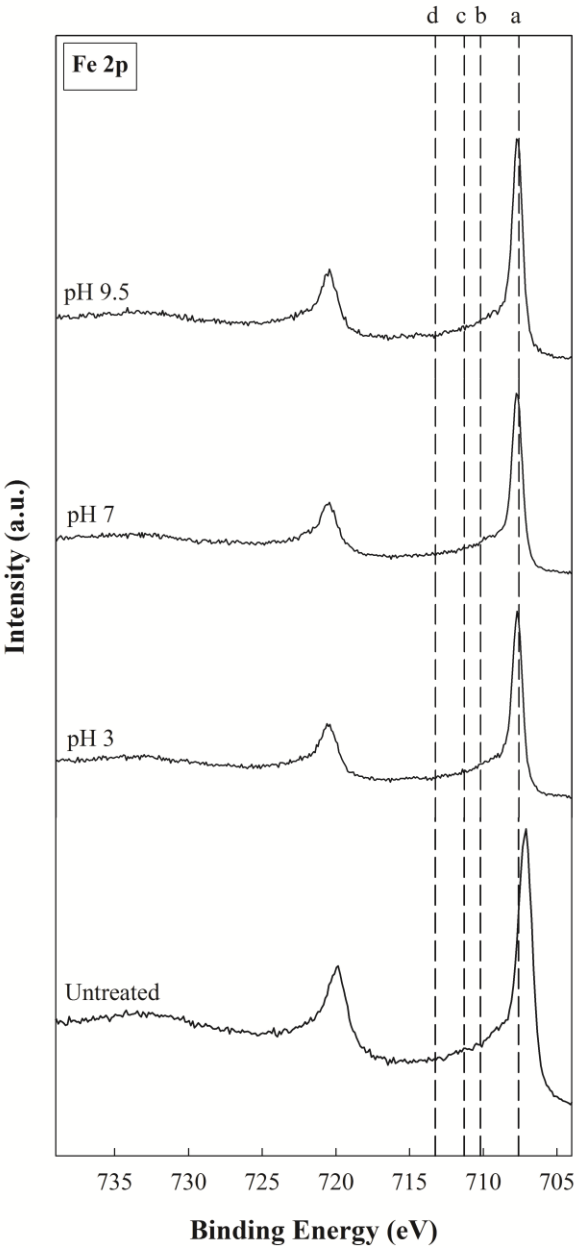

Fig. 4.7. XP spectra of untreated and 6 h Si–Cat-treated pyrite samples with Fe 2p peaks
a: 707.6 eV pyrite (Nesbitt et al., 1998)
b: 710.2 eV iron oxyhydroxide (Grosvenor et al., 2004)
c: 711.3 eV iron/silicon dioxide (Gettings and Kinloch, 1977)
d: 713.25 eV $Fe_2(SO_4)_3$ (Descostes et al., 2000)

The Fe 2p spectra of the four samples are presented in Fig. 4.7. This Fe 2p figure indicates that Si–Cat treatment decreased iron in pyrite peaks at 707.6 eV (Nesbit et al., 1998) and covered the treated pyrite surfaces with silicate coating as the peaks at around 711.3 eV attributable to iron/silicon oxide (Gettings and Kinloch, 1977) were observed. As the pH increased, the peak area associated with iron/silicon dioxide increases in the Fe $2p_{3/2}$ spectra (Table 4.3). The shared peaks confirm the formation of Fe–O–Si in the treated pyrite samples, which are consistent with analysis of the FTIR spectra (Fig. 4.6). The peak observed at 710.0 ± 0.03 eV correspond to iron oxyhydroxide (Grosvenor et al., 2004).

The presented S 2p spectra consist of two major doublets representing bulk mono sulfide and disulfide (Sasaki et al., 2010). S 2p data (Fig. 4.8 and Table 4.3) are fitted with two S 2p doublets based on prior research on pyrite, which is the peaks at 162.9 eV and 163.78 were assigned to the disulfide group (Brion, 1980) and the peaks at 161.65 eV and 162.83 eV feature to a monosulfide group (Nesbit and Muir, 1994). For S 2p peaks, sulfate peaks at 168.25 and 169.43 eV (Nesbit and Muir, 1994) can be seen on the untreated pyrite which we believed were produced during exposure of the sample to air because untreated pyrite sample was not covered by coating layer. This result also supported by iron(III) sulfate peak at 713.25 eV (Descostes et al., 2000) that can be seen only on untreated pyrite. Natural oxidation of untreated pyrite might cause the following oxidation reaction to produce iron sulfate.

$$2FeS_2 + 7O_2 + 2H_2O \rightarrow Fe_2(SO_4)_3 + 4H^+ + SO_4^{2-} \quad (4.2)$$

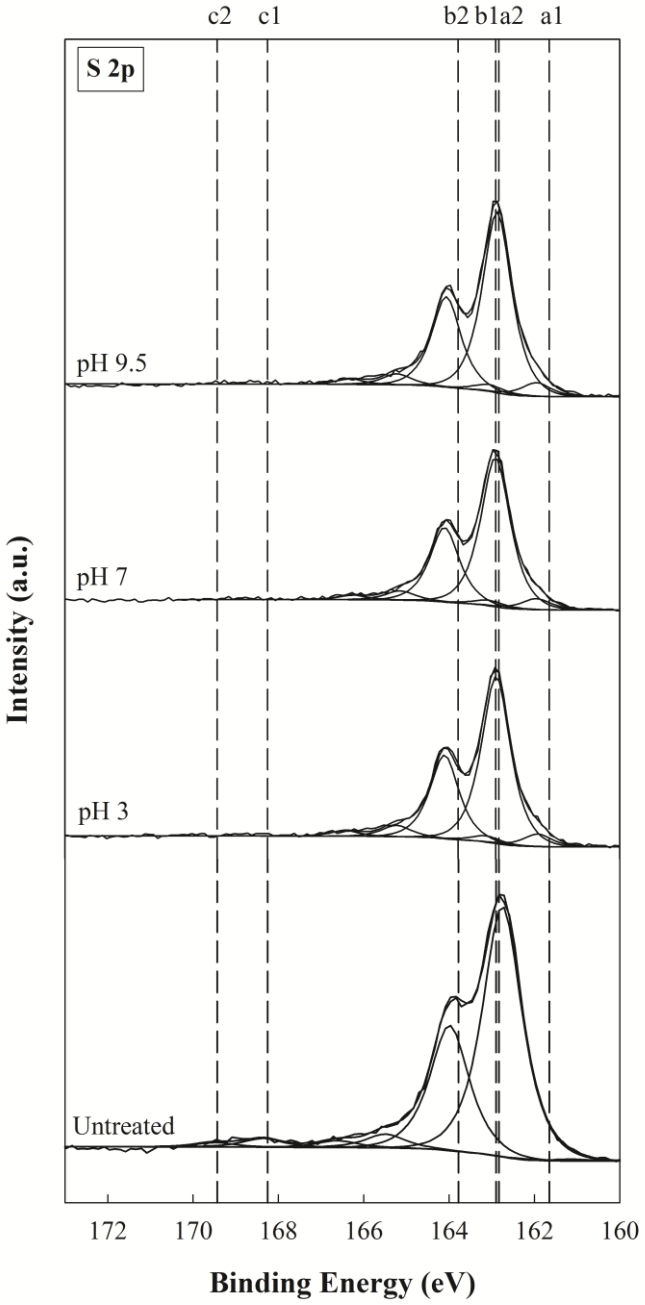

Fig. 4.8. XP spectra of untreated and 6 h Si–Cat-treated pyrite samples with S 2p peaks
a1: $2p_{3/2}$ 161.65 eV, a2: $2p_{1/2}$ 162.83 eV S^{2-} (Nesbit and Muir, 1994)
b1: $2p_{3/2}$ 162.9 eV, b2: $2p_{1/2}$ 163.78 eV S_2^{2-} (Brion, 1980)
c1: $2p_{3/2}$ 168.25 eV, c2: $2p_{1/2}$ 169.43 eV SO_4^{2-} (Nesbit and Muir, 1994)

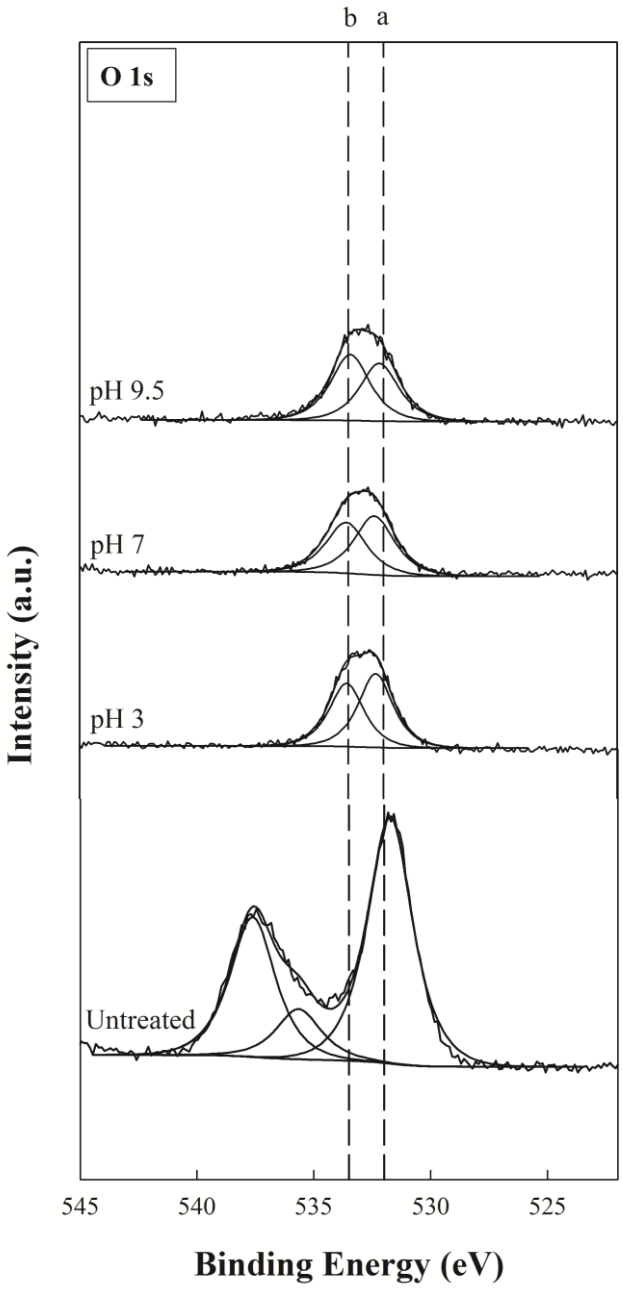

Fig. 4.9. XP spectra of untreated and 6 h Si–Cat-treated pyrite samples with O 1s peaks
a: 532.0 eV $Fe_2(SO_4)_3$ (Brion, 1980)
b: 533.5 eV iron/silicon dioxide

In the O 1s region (Fig. 4.9), there are two main components at E_B[O 1s] = 532.2 ± 0.30 eV, 533.5 ± 0.1 eV assigning to sulfate, and iron/silicon dioxide, respectively. As shown from the figure, it is clear that relative intensities of sulfate decreased around 78% by Si–Cat treatment at all pH values tested. From these results, it is might be caused by the silica–quinone layers that cover the surface of treated pyrite samples and inhibit pyrite oxidation. The peaks observed at around 533.5 eV only present in the Si–Cat treated pyrite samples and it is possibly from iron/silicone dioxide peaks. Other two peaks which give rise to high energy peak observed at E_B[O 1s] = 535.6 and 537.6 eV on untreated pyrite sample are not completely clear. The most rational explanation is that these oxygen species correspond to molecular oxygen occluded in intergrain of the metal oxide interface layer (Stadnichenko et al., 2007).

Variation of the Si 2p XPS binding energies among the various samples is considered to correlate with the Si–O bonds. The energy difference between the Si $2p_{3/2}$ and Si $2p_{½}$ levels is ~0.5 eV causing the two peaks to overlap (Pleul et al., 2003). The Si 2p spectra of pyrite samples are illustrated in Fig. 4.10. The peaks observed at 103 eV and 103.8 eV are attributed to silicon dioxide (Diao et al., 2013) and siloxanes (Paparazzo, 1996), respectively. From the present study, the position of the Si 2p peaks of treated pyrite samples shift from 103.5 to 103.8 eV as the silicate surface concentration increases with pH and show the formation of polymerization via siloxanes bonding. Also, the Si peak shifted to higher binding energy, which means that the binding energy of Si-O increased after treatment and also increased with pH. This observation supports the results of impedance analysis, which indicated that coating layer resistance increased with increasing pH. These Si 2p peak positions correlate with

the Si–O bands in the FTIR spectra in which polymeric silicate species are present via siloxanes bond. In Table 4.3, the fitted data for silicon dioxide and siloxanes bonds are shown. The siloxanes surface area for Si–Cat treated pyrite initially pH 3 is lower than those for Si–Cat treated pyrite initially pH 7 and 9.5 clearly indicating a lower degree of silicate polymerization.

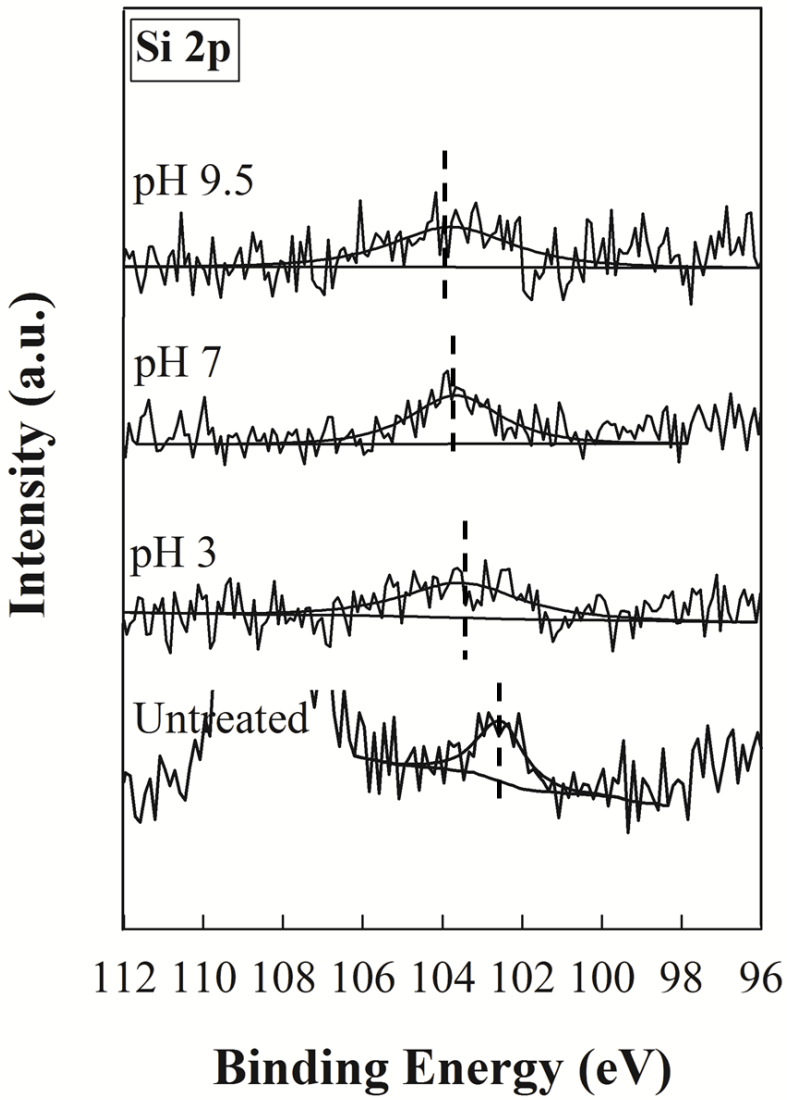

Fig. 4.10. XP spectra of untreated and 6 h Si–Cat-treated pyrite samples with Si 2p peaks.

Table 4.3. Comprehensive atomic allocation based on the measurement of narrow scan of Fe, S, O, and Si spectra of untreated and 6 h Si–Cat-treated pyrite samples.

Pyrite		Fe $2p_{3/2}$ a	Fe $2p_{3/2}$ b	Fe $2p_{3/2}$ c	Fe $2p_{3/2}$ d	S $2p_{3/2}$ a1	S $2p_{1/2}$ a2	S $2p_{3/2}$ b1	S $2p_{1/2}$ b2	S $2p_{3/2}$ c1	S $2p_{1/2}$ c2	O 1s a	O 1s b	Si 2p SiO_2	Si 2p Si–O–Si
Untreated	E_B/eV	707.2	710.0	-	713.8	161.1	162.2	162.8	164.0	168.4	169.5	531.7	-	102.5	-
	AREA	6966.2	529.4		146.8	37.1	18.5	5276.9	2638.4	185.8	92.9	5399.0		75.8	
Treated pH 3	E_B/eV	707.7	710.0	711.1	-	161.9	163.1	162.9	164.1	-	-	532.3	533.6	-	103.5
	AREA	3625.7	366.9	207.0		194.0	97.0	2585.7	1292.9			1244.6	1071.2		110.8
Treated pH 7	E_B/eV	707.7	710.0	711.2	-	162.0	163.1	162.9	164.1	-	-	532.4	533.6	-	103.7
	AREA	3514.5	384.2	248.7		174.8	87.4	2350.2	1175.1			1162.8	1005.0		117.3
Treated pH 9.5	E_B/eV	707.7	710.0	711.2		161.9	163.0	162.9	164.1	-	-	532.2	533.4	-	103.8
	AREA	4230.4	442.8	291.3		215.4	107.7	2827.3	1413.7			1099.9	1258.3		130.8
Average	E_B/eV	707.6	710.0	711.1	713.8	161.7	162.9	162.9	164.1	168.4	169.5	532.2	533.5	102.5	103.7
STDEV		0.28	0.03	0.01	-	0.42	0.42	0.07	0.05	-	-	0.30	0.10	-	0.13

Based on the analysis of SEM-EDX, FTIR, and XPS of the treated pyrite samples described above, a tentative mechanism of pyrite oxidation suppression by Si–Cat is proposed. The coating behavior may be explained in terms of the reaction between pyrite and silicate ions, as shown in Fig. 4.11.

The first step involves the hydrolysis of the Si–Cat complex, which yields reactive Si–OH group (silanol) and quinone (Eq. 4.1).

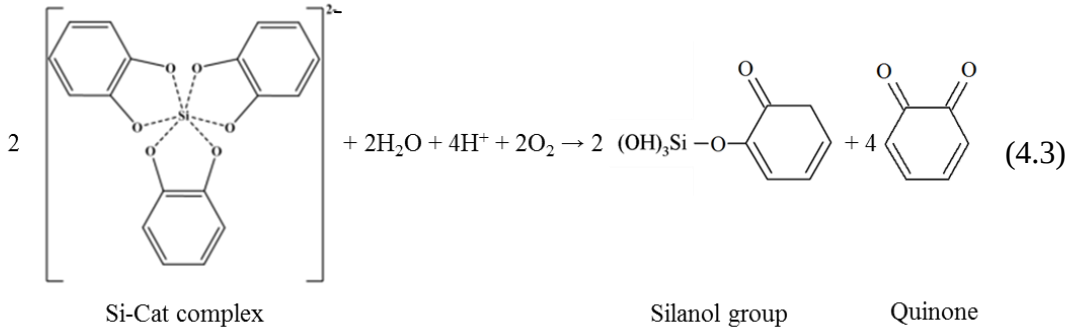

(4.3)

The next step of the process (Fig. 4.11a) is that pyrite surface is oxidized by air, and water. Resulting Fe^{3+} is hydrolyzed to form iron oxyhydroxide (Fig. 4.11b) on the surface of pyrite. Silanol groups then react with hydroxyl groups on the pyrite surface (Fig. 4.11c). The hydrogen bonds between silanol groups and hydroxyl groups converted into Fe–O–Si bonds, releasing water. This is consistent with analysis of FTIR whereas peaks at 955–960 cm^{-1} attribute to Fe–O stretching of the Fe–O–Si bonds (Fig. 4.6). In the last step, residual free silanol groups can further condense with each other, resulting Si–O–Si bonds (Fig. 4.11d), which is consistent with observed FTIR peaks at 1154–1160 cm^{-1} assigned to a shift of Si–O–Si in polymerized Si. This step occurs during drying after CME treatment. The drying conditions induce dehydration in this step.

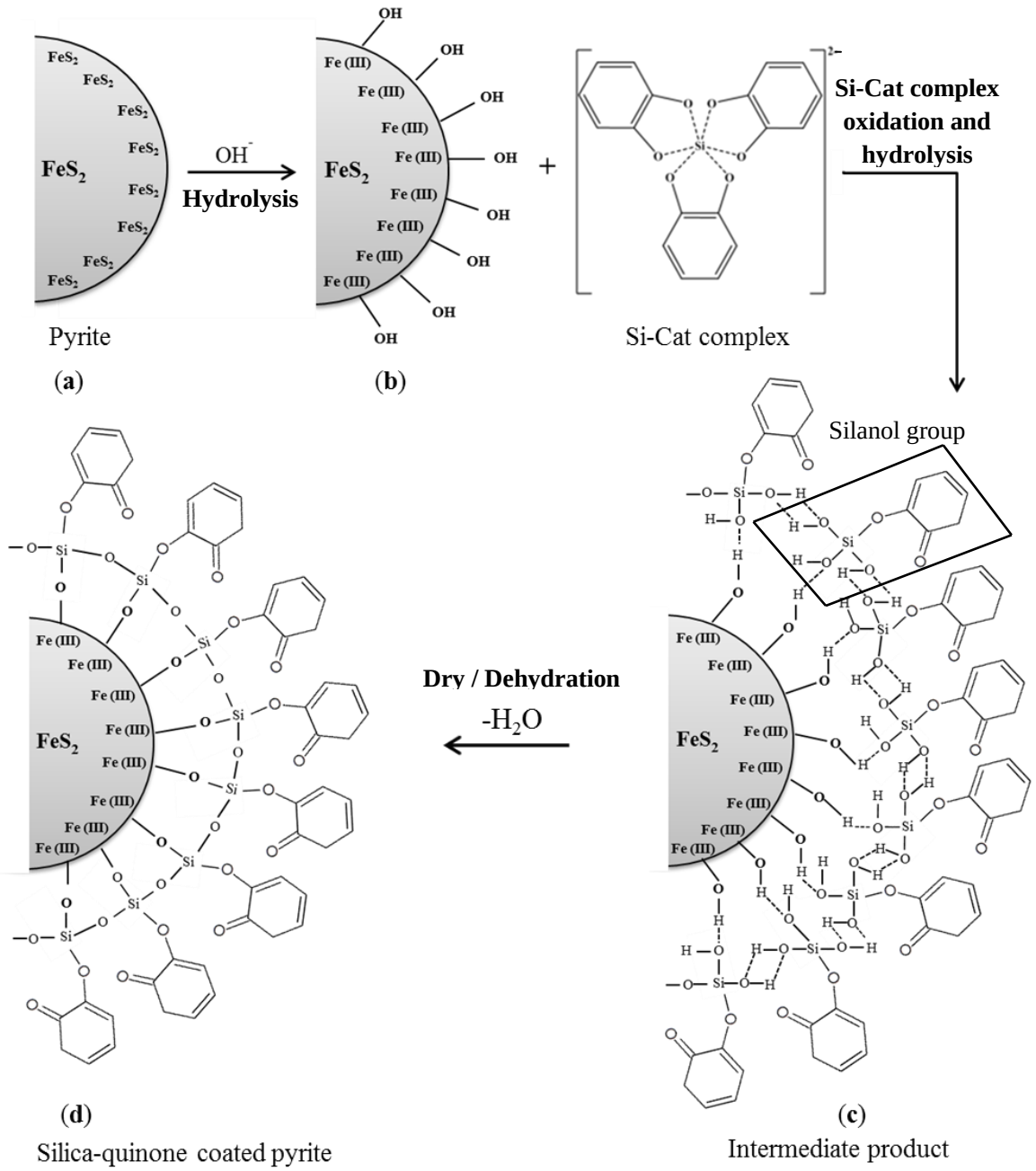

Fig. 4.11. Proposed mechanism of pyrite oxidation suppression by Si–Cat complex.

The proposed mechanism shows similar pathway with Diao et al. (2013) whereas the formation of covalent bonds (Fe–O–Si and Si–O–Si) were occur on the pyrite surface by using tetraethyorthosilicate (TEOS) and n-propyltrimethoxysilane (NPS). In Si–Cat treatment, the coating layer much more bulky than TEOS and NPS treatment. It caused by the attachment of 1 quinone molecule on the silanol group (Eq. 1). With this structure, the resulting coating layer probably could give bigger oxidation suppression effect.

4.4. Conclusions

In this chapter, Si–Cat adsorption and polymerization on the pyrite surface were examined systematically. Treatment by Si–Cat under different conditions resulted in differences in the suppression of pyrite oxidation.

Electrochemical behaviors demonstrated that treatment with Si–Cat for 6 h at an initial pH 9.5 gave the best barrier properties and pyrite oxidation suppression effect. The coating formed was shown by SEM-EDX to be silica rich. Evidence provided by FTIR and XPS analyses demonstrated that the coating layers on treated pyrite samples consist of a network of Fe–O–Si and Si–O–Si units bonded to the surface of pyrite. The Si–O–C asymmetric stretching mode was also shown by FTIR.

Detailed FTIR and XPS data show that (i) silicate polymerization occurs on the treated pyrite samples, (ii) Si–Cat treated pyrite initially pH 9.5 shows the highest polymerization degree based on the intensity and peak area of Si–O–Si bonds. These results show that the Si-Cat complex is selectively oxidized on the surface of pyrite to produce silanol groups, followed by hydrolysis with hydroxide on the surface of pyrite, then formation of a protective layer by dehydration during drying. Overall

results confirm the formation of silicate polymerization on the silica–quinone layer on treated pyrite samples that suppresses pyrite oxidation.

References

Anderson, B.F., Buckingham, D.A., Robertson, G.B., Webb, J., Murray, K.S., Clark, P.E., 1976. Models for the bacterial iron-transport chelate enterochelin. Nature 262, 722-724. doi: 10.1038/262722a0

Bartels, H., 1964. Stabilität von silicium-komplexen. Helv. Chim. Acta 47, 1605-1609. doi:10.1002/hlca.19640470623

Bellamy, L.J., 1975. The infrared spectra of complex molecules. Chapman and Hall Ltd., London. p. 9 and p. 92.

Bessho, M., Wajima, T., Ida, T., Nishiyama, T., 2011. Experimental study on prevention of acid mine drainage by silica coating of pyrite waste rocks with amorphous silica solution. Environ. Earth Sci. 64, 311-318. doi:10.1007/s12665-010-0848-0

Brion, D., 1980. Etude par spectroscopie de photoelectrons de la degradation superficielle de FeS_2, $CuFeS_2$, ZnS et PbS a l'air et dans l'eau. Appl. Surf. Sci. 5, 133-152. doi:10.1016/0378-5963(80)90148-8

Carlson L., Schwertmann, U., 1981. Natural ferrihydrites in surface deposits from Finland and their association with silica. Geochim. Cosmochim. Acta 45, 421-429. doi:10.1016/0016-7037(81)90250-7

Correns, C.W., 1961. The experimental chemical weathering of silicates. Clay Miner. Bull. 4, 249-265.

Descostes, M., Mercier, F., Thromat, N., Beaucaire, C., Gautier-Soyer, M., 2000. Use of XPS in the determination of chemical environment and oxidation state of iron and sulfur samples: constitution of a data basis in binding energies for Fe and S reference compounds and applications to the evidence of surface species of an oxidized pyrite in a carbonate medium. Appl. Surf. Sci. 165, 288-302. doi:10.1016/S0169-4332(00)00443-8

Diao, Z., Shi, T., Wang, S., Huang, X., Zhang, T., Tang, Y., Zhang, X., Qiu, R., 2013. Silane-based coatings on the pyrite for remediation of acid mine drainage. Water Res. 47, 4391-4402. doi:10.1016/j.watres.2013.05.006

Fytas, K., Bousquet, P., 2002. Silicate micro-encapsulation of pyrite to prevent acid mine drainage, CIM Bulletin 95, pp. 1063.

Gettings, M., Kinloch, A.J., 1977. Surface analysis of polysiloxane/metal oxide interfaces. J. Mater. Sci. 12, 2511-2518. doi:10.1007/BF00553938

Grosvenor, A.P., Kobe, B.A., Biesinger, M.C., McIntyre, N.S., 2004. Investigation of multiplet splitting of Fe 2p XPS spectra and bonding in iron compounds. Surf. Interface Anal. 36, 1564-1574. doi:10.1002/sia.1984

Lvovich, V.F., 2012. Impedance Spectroscopy, Application to Electrochemical and Dielectric Phenomena. John Wiley & Sons, Inc., Hoboken, New Jersey. pp. 26-34.

Nesbitt, H.W., Bancroft, G.M., Pratt, A., Scaini, M., 1998. Sulfur and iron surface states on fractured pyrite surfaces. Am. Mineral., 83, 1067-1076.

Nesbitt, H.W., Muir, I.J., 1994. X-ray photoelectron spectroscopic study of a pristine pyrite surface reacted with water vapour and air. Geochim. Cosmochim. Acta 59, 4667–4679. doi:10.1016/0016-7037(94)90199-6

Paparazzo, E., 1996. On the XPS analysis of Si–OH groups at the surface silica. Surf. Interface Anal. 24, 729-730. doi:10.1002/(SICI)1096-9918(19960930)24:10<729::AID-SIA183>3.0.CO;2-P

Pleul, D., Frenzel, R., Eschner, M., Simon, F., 2003. X-ray photoelectron spectroscopy for detection of the different Si–O bonding states of silicon. Anal. Bioanal. Chem. 375, 1276-1281. doi: 10.1007/s00216-003-1811-7.

Sasaki, K., Tsunekawa, M., Ohtsuka, T., Konno, H., 1995. Confirmation of a sulfur-rich layer on pyrite after oxidative dissolution by Fe(III) ions around pH 2. Geochim. Cosmochim. Acta 59, 3155-3158. doi: 10.1016/0016-7037(95)00203-C

Sasaki, K., Takatsugi, K., Ishikura, K., Hirajima, T., 2010. Spectroscopic study on oxidative dissolution of chalcopyrite, enargite and tennantite at different pH values. Hydrometallurgy 100, 144–151. doi:10.1016/j.hydromet.2009.11.007

Schweigert, N., Zehnder, A.J.B., Eggen, R.I.L, 2001. Chemical properties of catechols and their molecular modes of toxic action in cells, from microorganisms to mammals. Environ. Microbiol. 3, 81-91. doi: 10.1046/j.1462-2920.2001.00176.x

Schwertmann, U., Thalmann, H., 1976. The influence of [Fe(II)], [Si], and pH on the formation of lepidocrociite and ferrihydrite during oxidation of aqueous $FeCl_2$ solution. Clays and Clay Miner. 11, 189-200.

Sever, M.J., Wilker, J.J., 2004. Visible absorption spectra of metal-catecholate and metal-tironate complexes. Dalton Trans. 7, 1061–1072. doi: 10.1039/B315811J

Shirley, D.A., 1972. High resolution X-ray photoelectron spectrum of the valence bands of gold. Phys. Rev. B5, 4709–4714. doi: http://dx.doi.org/10.1103/PhysRevB.5.4709

Stadnichenko, A.I., Koshcheev, S.V., Boronin, A.I., 2007. Oxidation of the polycrystalline gold foil surface and XPS study of oxygen states in oxide layers. Moscow University Chemistry Bulletin 62, 343-349.

Yuniati, M.D., Hirajima, T., Miki, H., Sasaki, K., 2014. Proceedings of International Symposium on Earth Science and Technology (CINEST 2014), pp. 108-111.

Zhang, Y.L., Evangelou, V.P., 1998. Formation of ferric hydroxide–silica coatings on pyrite and its oxidation behavior. Soil Sci. 163, 53-62. doi:10.1097/00010694-199801000-00008

CHAPTER 5

Application of a Silicate Coating on Chalcopyrite, Molybdenite, and Arsenopyrite

Although pyrite is the most common sulfide mineral on earth, some other important mineral sulfides that occur in mining regions may also produce AMD, i.e., chalcopyrite ($CuFeS_2$), molybdenite (MoS_2), and arsenopyrite (FeAsS). This chapter describes the application of a Si–Cat complex to other sulfide minerals to suppress their oxidation rate. The effect of a silicate covering layer on treated minerals' surfaces was evaluated by potential polarization, chronoamperometry, electrochemical impedance spectroscopy (EIS), and scanning electron microscopy with energy dispersive X-ray spectroscopy (SEM-EDX).

5.1. Introduction

Acid mine drainage (AMD) occurs when certain sulfide minerals are exposed to oxidizing conditions. Although pyrite is the most common sulfide mineral on earth, some other important mineral sulfides that occur in mining regions may also produce AMD, i.e., chalcopyrite ($CuFeS_2$), molybdenite (MoS_2), and arsenopyrite (FeAsS). (Simate and Ndlovu, 2014).

Chalcopyrite is the main copper sulfide ore, which also contains varying amounts of non-valuable and undesired pyrite (Bulatovic, 2007). Another mineral species associated with copper sulfide ores is molybdenite, which has high commercial value. Copper production has recently increased. The enormous amount of ore processing could potentially have continuous environmental effects through the release of huge amounts of solid waste, such as tailings. Based on copper cycle assessment, all of the steps of mineral processing are highly energy-intensive and generate hazardous waste materials (McLellan and Corder, 2012; Memary et al., 2012; Moors et al., 2005). Therefore, the mining industry requires new environmentally friendly reagents for processing and to control the effects of sulfide mineral exposure.

Arsenopyrite is the most abundant arsenic-containing mineral on earth, and it is normally associated with many other minerals of economic importance. Therefore, it is involved in the environmental effects of mining activities, especially sulfide mineral oxidation.

Because CME using a Si–Cat complex can suppress pyrite oxidation by creating a coating layer on the pyrite surface (Jha et al. 2008, 2012; Satur et al.,

2007), application of the Si–Cat complex to suppress the oxidation of other sulfide minerals is reported in this chapter.

The effect of a silicate covering layer on treated minerals' surfaces was evaluated by potential polarization, chronoamperometry, electrochemical impedance spectroscopy (EIS), and scanning electron microscopy with energy dispersive X-ray spectroscopy (SEM-EDX).

5.2. Materials and methods

5.2.1. Materials

5.2.1.1. Chalcopyrite, molybdenite, and arsenopyrite

Three sulfide mineral samples, chalcopyrite (Miyatamata mine, Japan), molybdenite (Hirase mine, Japan), and arsenopyrite (Magome mine, Japan), were used as experimental samples in this study.

For surface characteristic, sulfide mineral samples were ground to +38–75 μm on an agate mortar in a nitrogen-purged glove box. After grinding, the washing method reported by Sasaki et al. (1995) was used to remove the surface oxide. Finally, the washed minerals were dried by freeze dehydration.

For electrochemical analyses, sulfide mineral samples were used as working electrodes. The mineral was cut into cubes with working surface area of approximately 0.39, 0.88, and 0.64 cm^2 for chalcopyrite, molybdenite, and arsenopyrite, respectively. One side of the mineral surface was used as the electrode surface and the other side was connected to a copper wire using silver conductive paste and cemented with epoxy resin. The chalcopyrite and arsenopyrite electrodes surfaces were polished with #400 to #4000 emery paper, a Texmet (Buehler, IL,

USA) perforated non-woven pad, and a DP-Nap (Struers, Ballerup, Denmark) fine polishing cloth mounted on a plate using 3 μm and 1 μm diamond sprays. For molybdenite, the working electrode was wiped with 3 μm, 1 μm, and 0.25 μm diamond spray. After polishing, the polishing residues on the electrodes were removed by ethanol and distilled water.

5.2.1.2. Si–Cat solution

Solution of 7.00 mmol/L catechol ($C_6H_4[OH]_2$) (Wako, special grade) was prepared using ultrapure water. Subsequently, 2.34 mmol/L sodium metasilicate nonahydrate ($Na_2SiO_3 \cdot 9H_2O$) (Wako, special grade) was added to the catechol solution. This solution referred as silicon-catechol (Si–Cat) complex and used for mineral surface treatment.

5.2.2. Methods

5.2.2.1. Pretreatment of chalcopyrite, molybdenite, and arsenopyrite

Washed chalcopyrite (10.00 g) was added to Si–Cat solution (100 mL) in a 250 mL bottle, and the mixture was shaken at 100 rpm for 1 h at 25 °C. The same procedure also used for molybdenite and arsenopyrite. The solid residues were recovered from each bottle by filtration and dried by freeze dehydration. These three treated samples are denoted Si–Cat chalcopyrite, Si–Cat molybdenite and Si–Cat arsenopyrite.

5.2.2.2. Surface characteristics of coating layer on chalcopyrite, molybdenite, and arsenopyrite

The surface characteristics of chalcopyrite, molybdenite, and arsenopyrite samples, prepared as described in Section 5.2.2.1, were investigated using scanning electron microscopy with energy dispersive X-ray spectroscopy (SEM-EDX, Keyence VE-9800, Osaka, Japan). The data were compared with those for untreated minerals.

5.2.2.3. Pretreatment and electrochemical analysis of chalcopyrite, molybdenite, and arsenopyrite

Each working electrodes, prepared in Section 5.2.1.1, were immersed in Si–Cat complex solution, stirred with a magnetic stirrer at 100 rpm for 1 h at 25 °C, air dried for 30 min, and used for electrochemical measurements in 0.10 mol/L sulfuric acid.

The electrochemical measurements were performed using three standard electrode cells consisting of a working electrode, a platinum counter electrode, and a silver/silver chloride electrode (Ag/AgCl; +0.198 V vs. standard hydrogen electrode) as reference electrode. The three electrode cells and sulfuric acid were placed in a glass container. Potential polarization, chronoamperometric, and electrochemical impedance analysis (EIS) experiments were performed on the untreated and treated sulfide mineral samples at room temperature.

The potential polarization and chronoamperometric experiments were performed using an electrochemical analyzer (1205 B, BAS ALS CH Instruments, Tokyo, Japan). Potential polarization was achieved using an open-circuit potential in the anodic direction, at a scan rate of 10 mV/s, and the chronoamperometric

experiments were performed at 800 mV for 800 s. All the measured potentials were reported with respect to the standard hydrogen electrode. The EIS measurements were performed at an open-circuit potential, using an electrochemical instrument (Solartron Analytical 1280 C, Hampshire, UK), in the frequency range 0.1–20,000 Hz with a peak-to-peak amplitude of 10 mV. The impedance data were modeled to an equivalent circuit (EC) using the data analysis program Zview® (Scribner Associates, Inc., Southern Pines, NC, USA), using iterative empirical data fitting combined with trial circuit elements chosen based on theoretical considerations.

5.3. Results and discussion

5.3.1. Surface characteristics of coating layer on chalcopyrite, molybdenite, and arsenopyrite.

The surface characteristics of the untreated and treated mineral samples are shown in Figs. 5.1, 5.2, and 5.3 for chalcopyrite, molybdenite, and arsenopyrite, respectively.

Figures 5.1–5.3 show that silica was present on both the untreated and treated mineral samples, but the silica density of the treated minerals was higher than that of the untreated minerals. The Si contents of the untreated and treated chalcopyrite samples were 0.15% and 0.87%, respectively. The Si contents of the untreated and treated molybdenite samples were 0.00% and 3.10%, respectively. The Si contents of untreated and treated arsenopyrite samples were 2.65% and 3.13%, respectively. These results are similar to the surface characteristics of the coating layer on the pyrite samples, and confirm the adsorption of silica on the surface of the treated minerals.

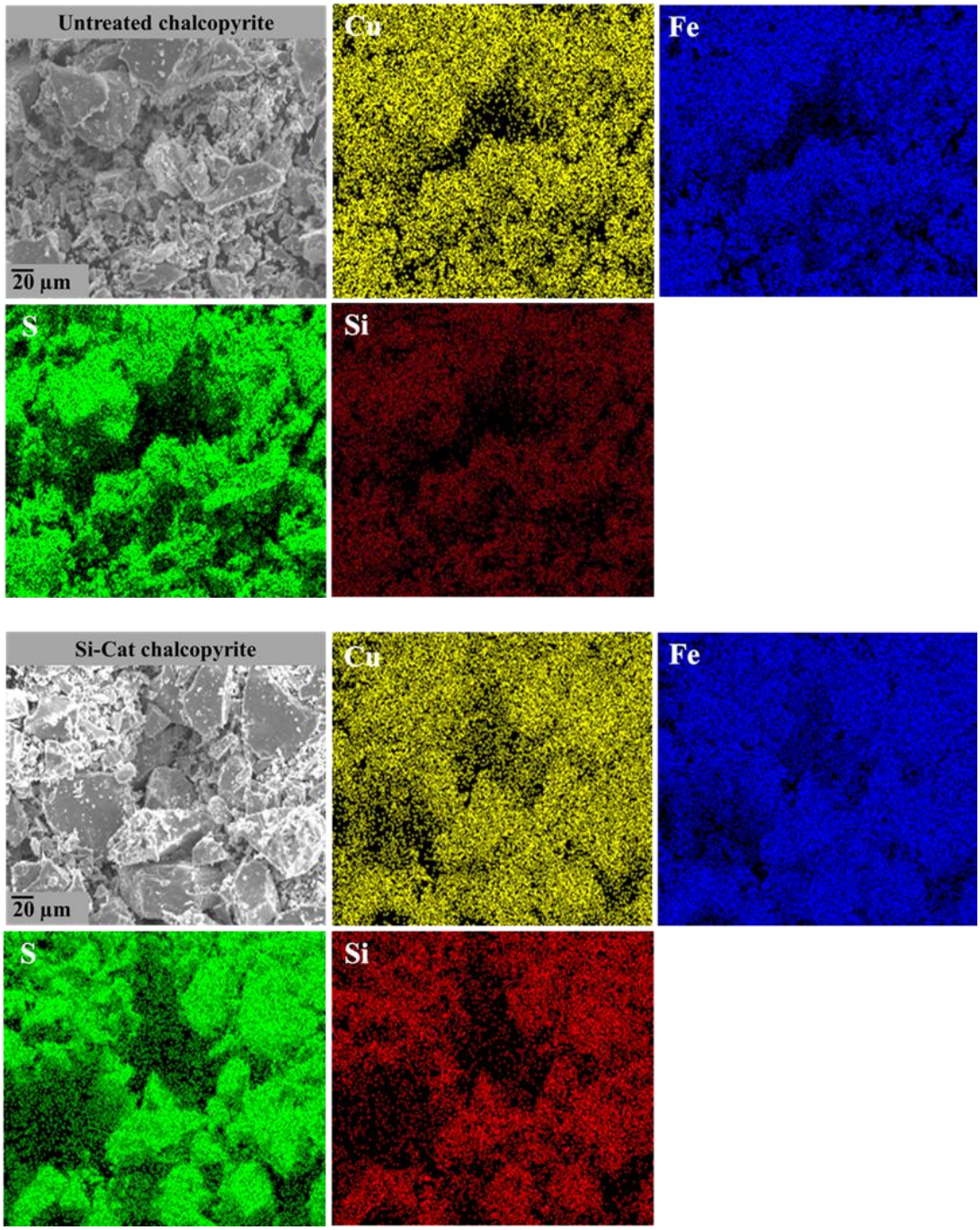

Fig. 5.1. SEM-EDX element mapping of untreated and Si–Cat chalcopyrite.

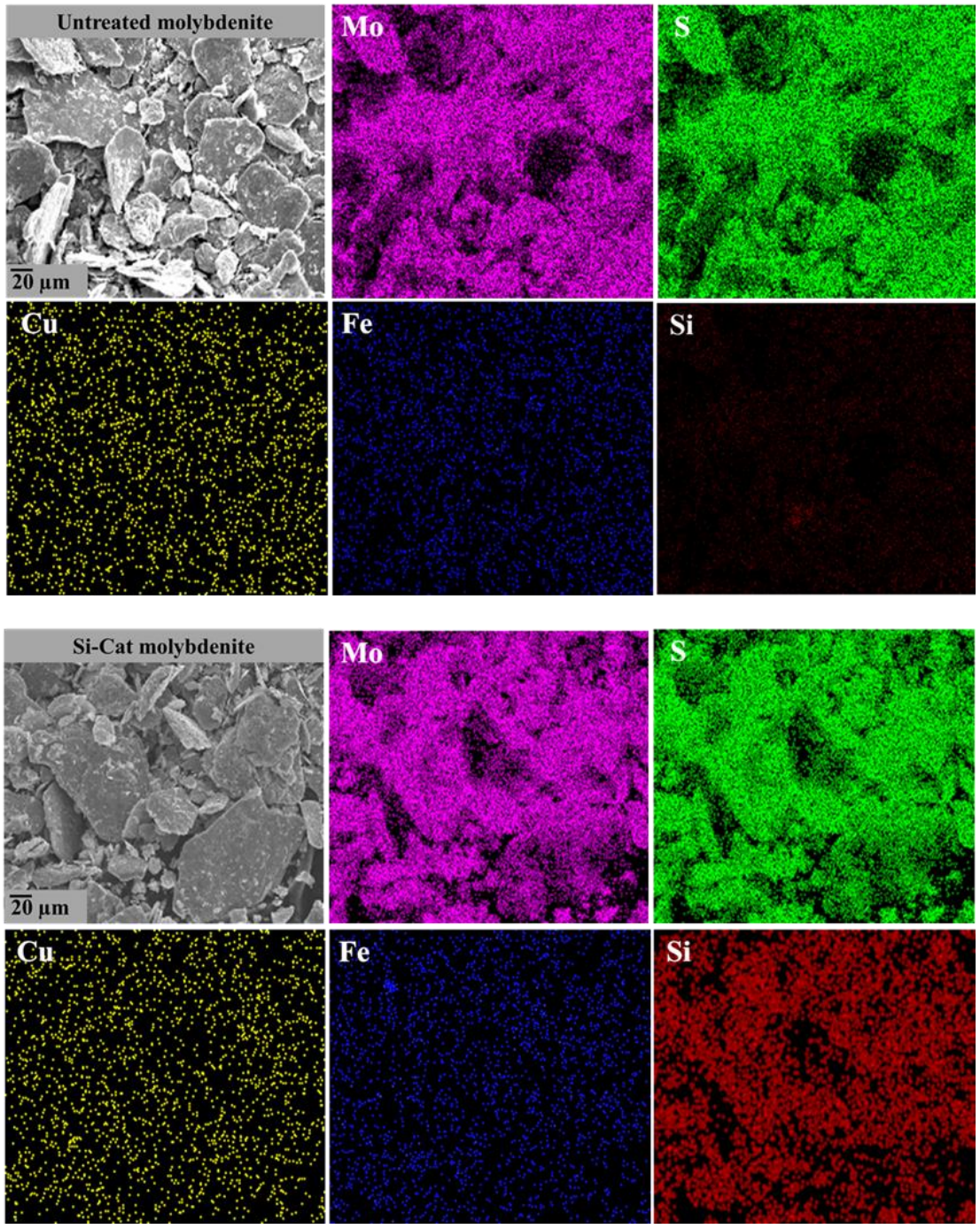

Fig. 5.2. SEM-EDX element mapping of untreated and Si–Cat molybdenite.

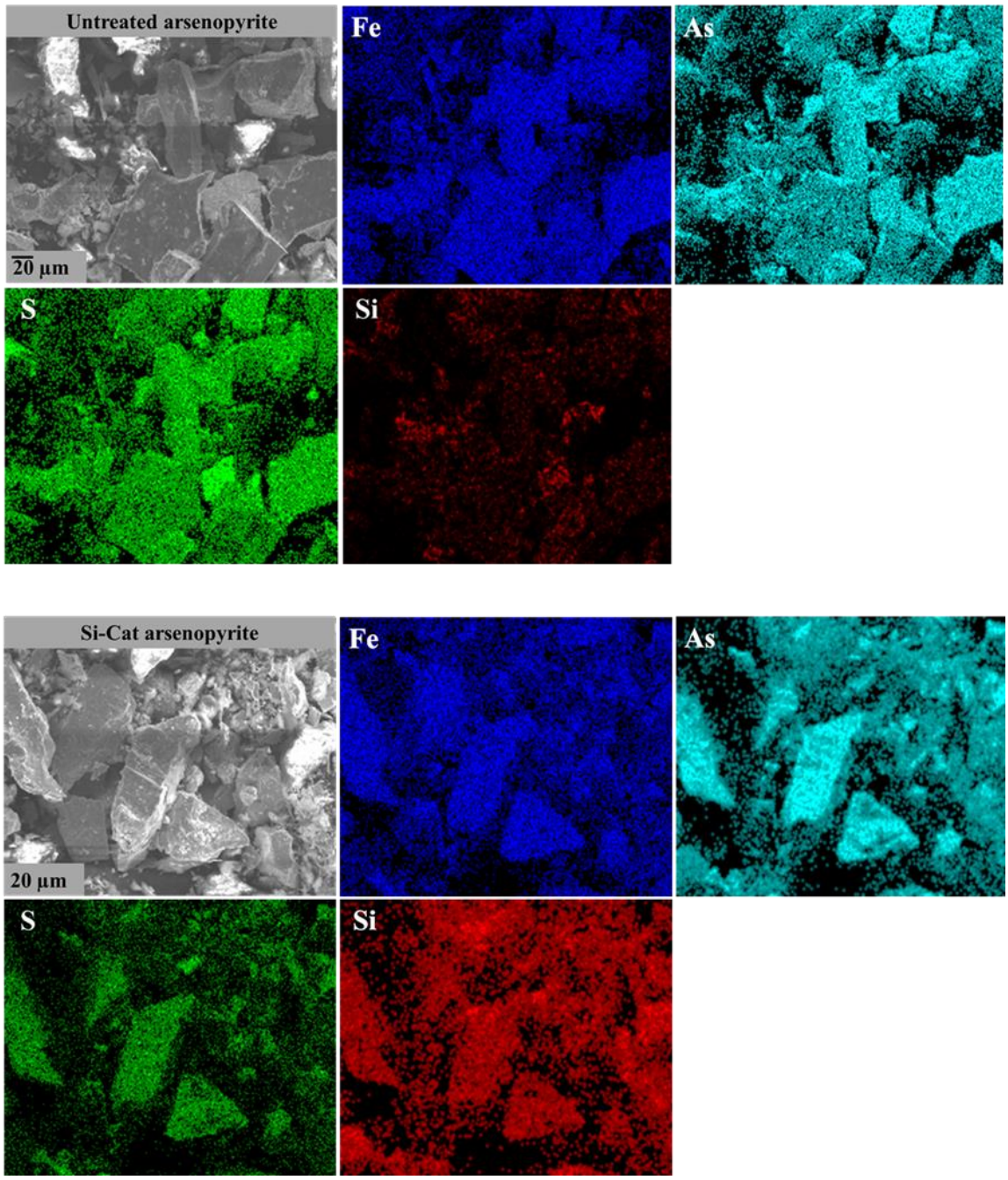

Fig. 5.3. SEM-EDX element mapping of untreated and Si–Cat arsenopyrite.

5.3.2. Electrochemical analysis

To investigate the oxidation and reduction reactions on the sulfide minerals surfaces, potential polarization and chronoamperometric analyses were conducted by using chalcopyrite, molybdenite, and arsenopyrite working electrodes. Potential polarization is the change of potential of an electrode from its equilibrium potential of an electrochemical reaction. The potential polarization was determined using the working electrodes in a pretreatment solution containing silicate and/or catechol ions, from the open-circuit potential in the anodic direction, at a scan rate of 10 mV/s; the results are shown in Fig. 5.4.

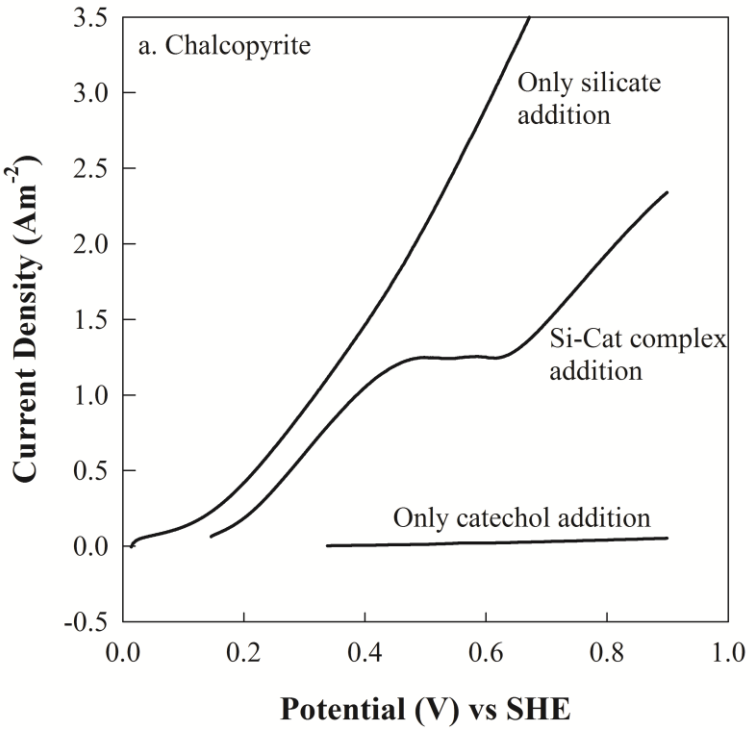

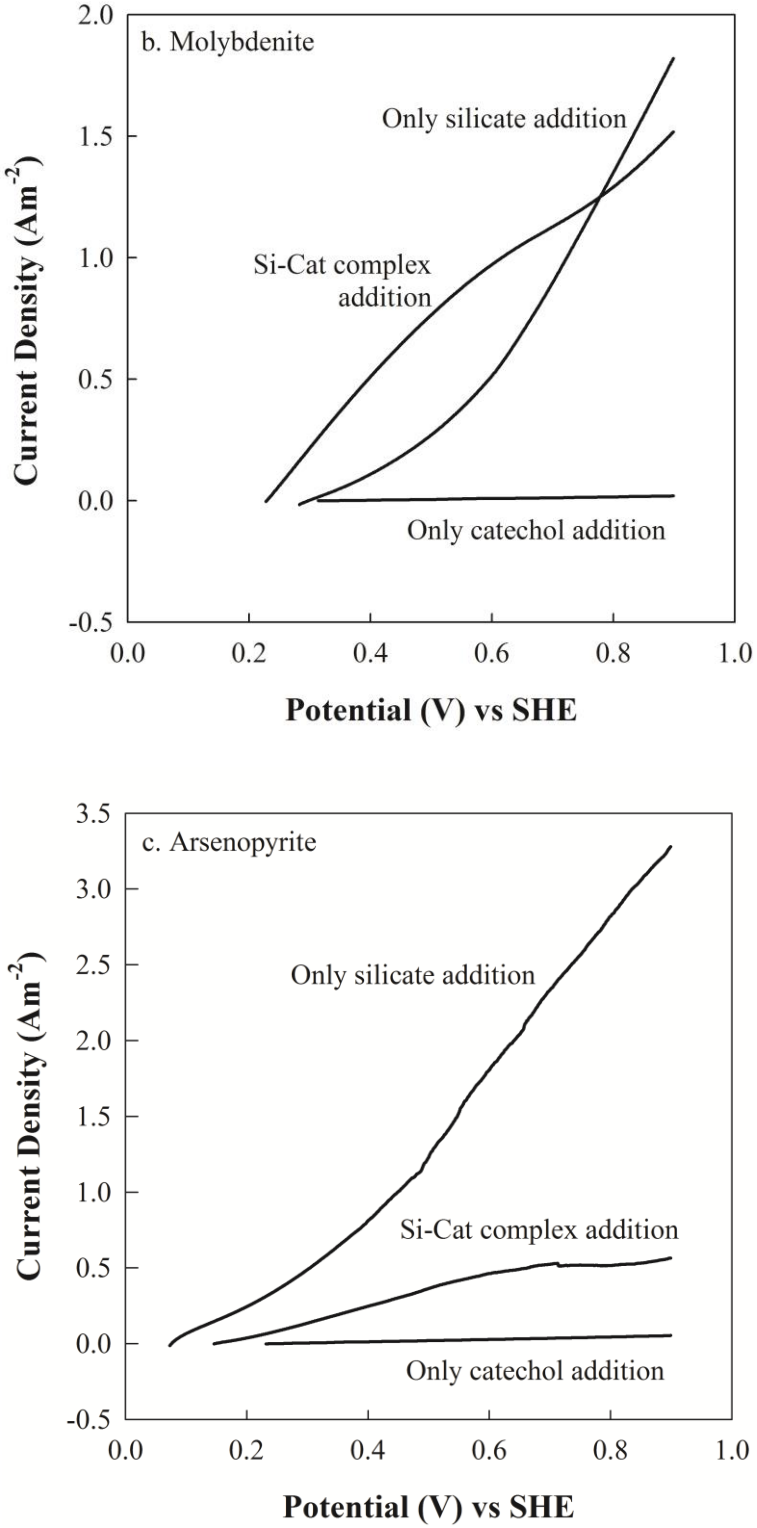

Fig. 5.4. Polarization curves of minerals working electrode in silicate and/or catechol solution for (a) chalcopyrite, (b) molybdenite, and (c) arsenopyrite.

In the presence of Si–Cat, Fig. 5.4 show anodic current shoulder lines at around 470–640, 520–660, and 690–840 mV for chalcopyrite, molybdenite, and arsenopyrite, respectively. These anodic current shoulder lines were not observed in the absence of the Si–Cat complex. The current increased with increasing potential when silicate solution only was used, and with catechol solution only, the current was very low. These results suggest that the shoulder lines correspond to oxidative decomposition of the Si–Cat complex on the minerals' surfaces, and show the insulation effect of the coating layer on the working electrode surfaces formed by the reaction products. The potential values that show oxidative decomposition of the Si–Cat complex on the sulfide minerals indicate the potential required to suppress the oxidation rate. From the results in Fig. 5.4, decomposition of the Si–Cat complex on the surface of arsenopyrite is much more difficult than on chalcopyrite and molybdenite.

The anodic currents for chalcopyrite, molybdenite, and arsenopyrite (Fig. 5.4) were 1.24, 0.90, and 0.53 Am^{-2}, respectively. The anodic current represents the oxidation rate of oxidative decomposition of the Si–Cat complex on the sulfide mineral surfaces. This means that the Si–Cat complex oxidation rate on the chalcopyrite surface is higher than that on molybdenite and arsenopyrite. In comparison with pyrite (Chapter 3, Fig. 3.6), pyrite shows the highest value (1.77 Am^{-2}) than other sulfide minerals that investigated in this chapter.

Chronoamperometric experiments were performed to measure the oxidation rates of sulfide minerals with and without pretreatment. These experiments were performed at 800 mV for 800 s. The results are shown in Fig. 5.5, as curves of current density against time. The current density is the anodic current of the working

electrode in the working area of 0.39, 0.88, and 0.64 cm^2 for chalcopyrite, molybdenite, and arsenopyrite, respectively. The anodic currents of the treated samples (Si–Cat chalcopyrite, Si–Cat molybdenite and Si–Cat arsenopyrite) are lower than those of the untreated samples. Because the anodic current represents the flow of electrical charge (usually carried by electrons) into a working electrode (as a result of oxidation of one or more species in the electrolyte solution), the lower anodic current of the treated samples mean that the oxidation rates of these samples are lower than those of the untreated samples. These results indicate that formation of a coating layer on the treated minerals' surfaces lowers the oxidation rate.

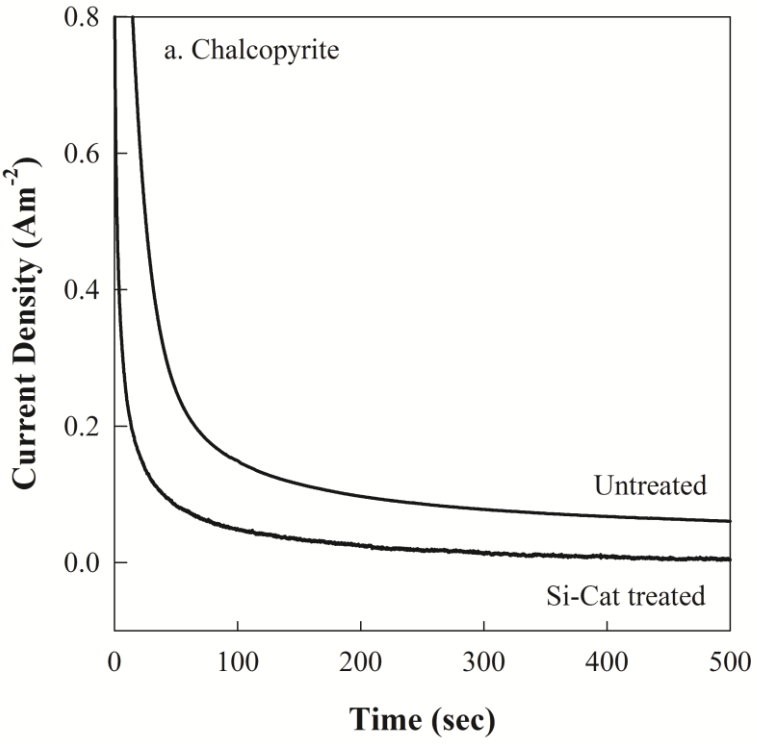

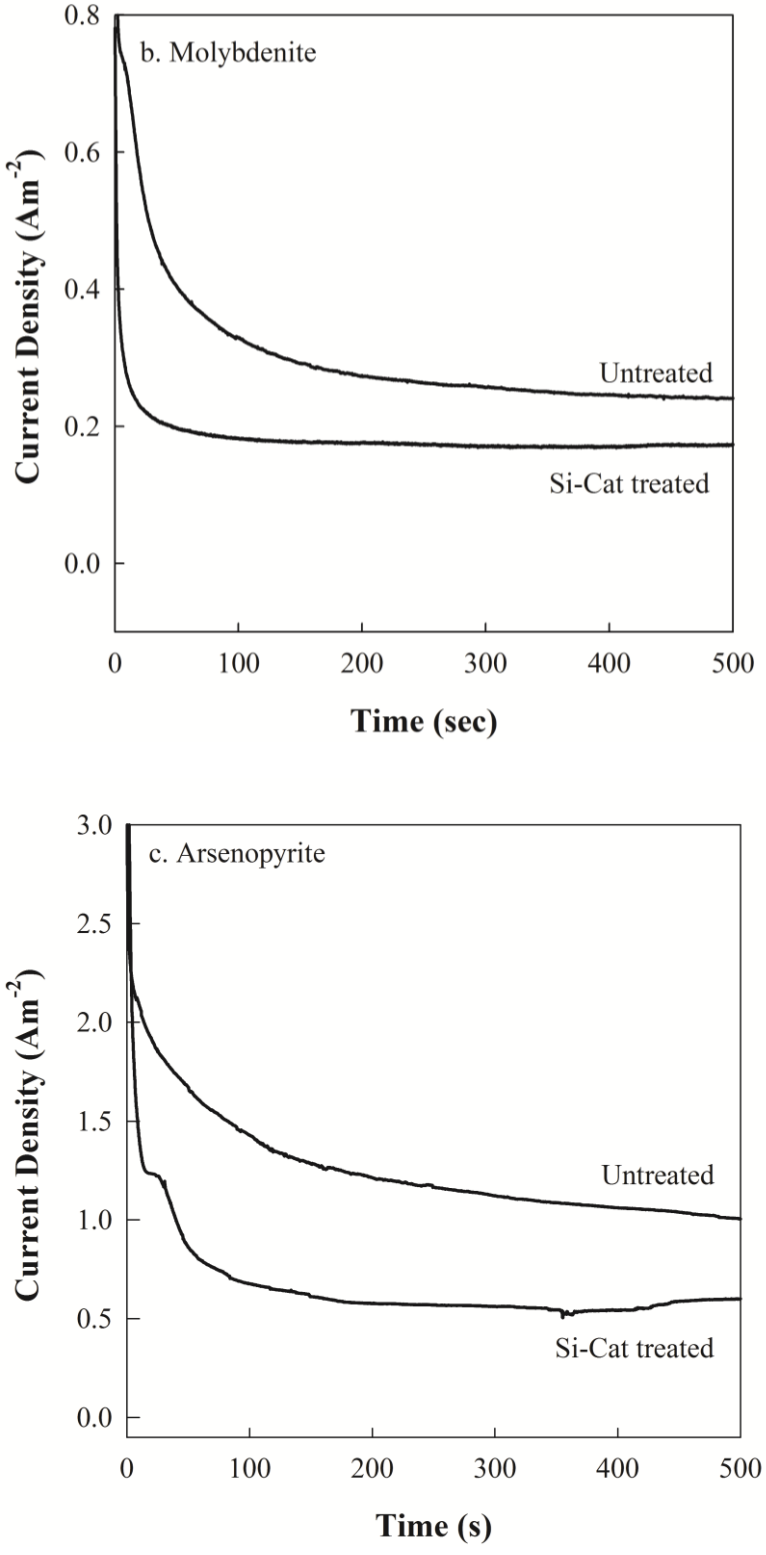

Fig. 5.5. Chronoamperometric curves of untreated and Si–Cat-treated minerals in 0.1 M H_2SO_4 for (a) chalcopyrite, (b) molybdenite, and (c) arsenopyrite.

The chronoamperometric curves (Fig. 5.5) show that the anodic currents of the untreated and treated sulfide minerals decrease with time and are almost stable after 500 s at different values. The values are shown in Table 5.1. From Table 5.1, Si–Cat treatment resulted in a better suppression effect for chalcopyrite than for molybdenite and arsenopyrite.

Table 5.1. Anodic currents of untreated and Si–Cat-treated sulfide minerals calculated from Fig. 5.5.

Sulfide mineral	Anodic currents (Am^{-2})		
	Chalcopyrite	Molybdenite	Arsenopyrite
Untreated	0.045	0.242	1.016
Si–Cat treated	0.007	0.173	0.605

To study the effect of silica-quinone layer as a barrier on the surface of chalcopyrite, molybdenite, and arsenopyrite, electrochemical impedance spectroscopy (EIS) analyses of untreated and treated sulfide mineral samples were conducted. The EIS complex plane plots (Nyquist plots) of the untreated and treated sulfide mineral samples are shown in Fig. 5.6.

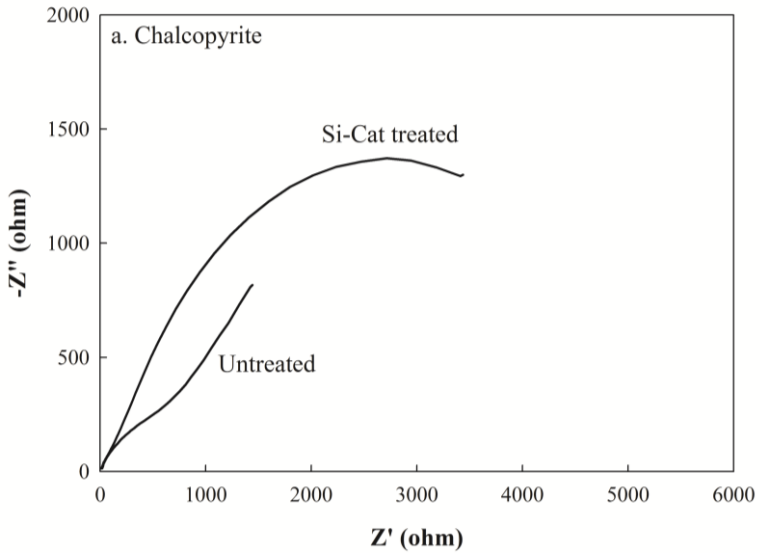

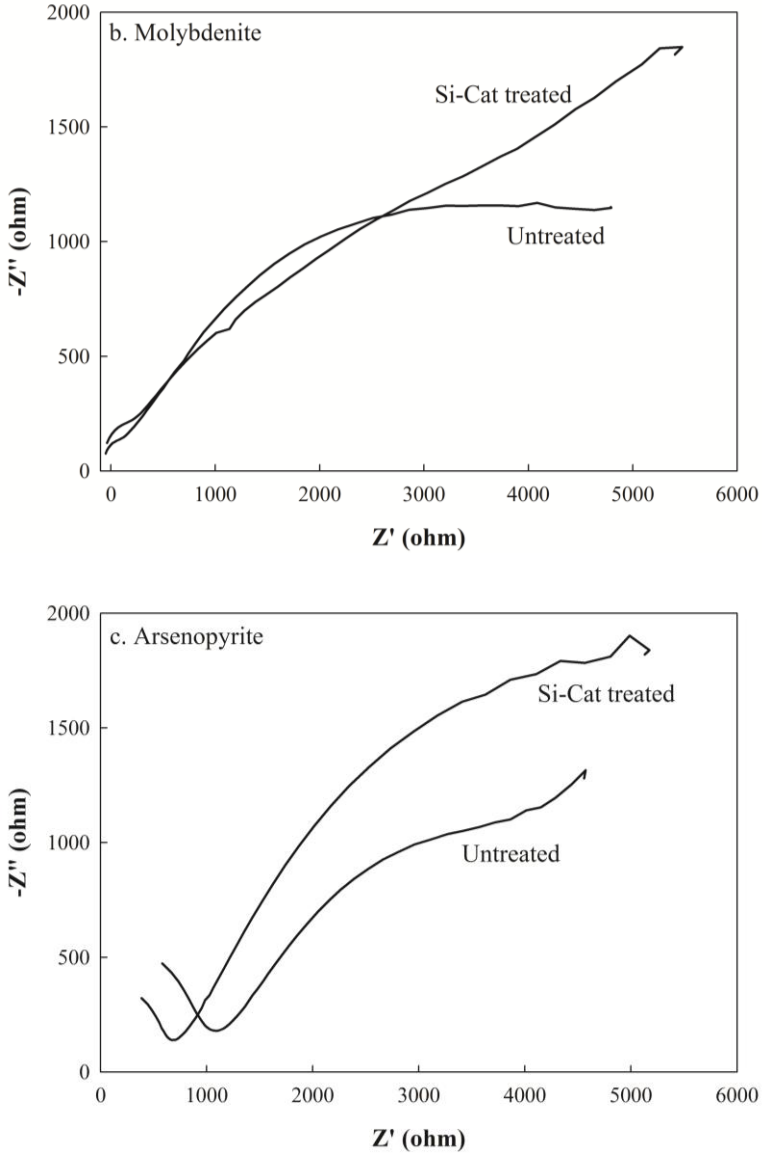

Fig. 5.6. EI spectra of untreated and Si–Cat-treated minerals for (a) chalcopyrite, (b) molybdenite, and (c) arsenopyrite.

Based on the observations made for all the systems, the Nyquist plots for untreated and treated sulfide mineral samples show similar pattern with untreated and treated pyrite samples (Chapter 3, Section 3.3). From these results, the EIS experimental data are fitted using the same EC model of pyrite as shown in Fig. 5.7.

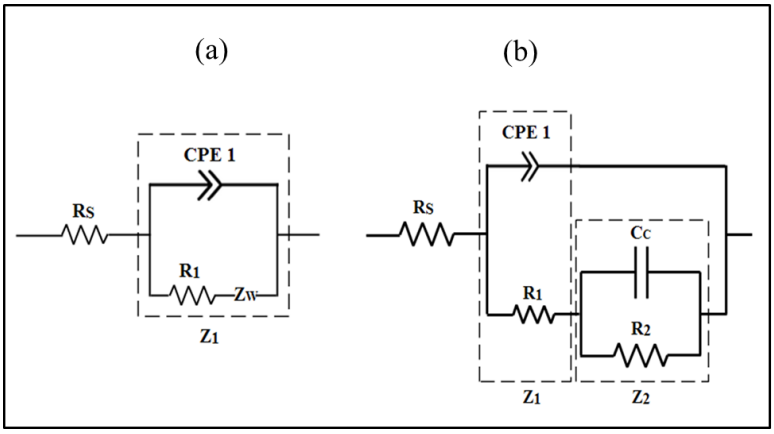

Fig. 5.7. EC models of (a) untreated sulfide minerals, and (b) Si–Cat-treated sulfide minerals.

The simplest EC model for characterizing the untreated sulfide minerals (Fig. 5.7a) includes the electrolyte solution resistance (R_s), the charge-transfer resistance of the sulfide mineral (R_1), a constant phase element (CPE), and the Warburg diffusion resistance (Z_w). A CPE was used in this model instead of a capacitor to compensate for the rough and porous electrode (Jorcin et al., 2006). The untreated molybdenite sample (Fig. 5.6b) did not show the Warburg diffusion phenomenon, which causes the Nyquist plot of the EC model of the untreated mineral to become a straight line at the end of the plot (Liu et al., 2011). This means that in molybdenite, diffusion at lower frequencies did not occur. This might be caused by molybdenite being a cleavage mineral with piling thin layer construction. The surface of molybdenite is composed of sulfur atoms and has hydrophobic properties.

Similar to treated pyrite sample, Fig. 5.7b shows the EC model for the treated minerals. When this EC model is applied to the treated sulfide mineral samples (a coating immersed in an electrolyte), R_s represents the resistance of the electrolyte solution between the reference electrode tip and the surface of the coating. The

charge-transfer resistance of the sulfide mineral samples (R_1) is associated with the resistance (R_2) and capacitance (C_C) of the coating layer.

The capacitance (C_C) of the arsenopyrite coating layer was mathematically modelled using a constant phase element that shows a slow adsorption reaction (Jorcin et al., 2006). This is consistent with the potential polarization results that showed decomposition of the Si–Cat complex on the surface of arsenopyrite was much more difficult than on chalcopyrite and molybdenite.

The calculated parameters of the EC elements for the untreated and treated sulfide mineral samples are listed in Table 5.2. The low chi-squared (χ^2) values, which represent the sum of quadratic deviations between the experimental and calculated data divided by the calculated data, indicate that the experimental data are fitted well with the proposed circuit models.

Table 5.2.

EC element parameters obtained by fitting experimental impedance data for untreated and Si–Cat-treated sulfide minerals with EC models shown in Fig. 5.7.

Parameter	Chalcopyrite		Molybdenite		Arsenopyrite	
	Untreated	Treated	Untreated	Treated	Untreated	Treated
R_1/ohm cm^{-2}	1100.00	1418.99	9920.56	7339.25	2116.67	1693.33
R_2/ohm cm^{-2}	-	5659.49	-	9106.54	-	26052.78
$\chi^2/10^{-3}$	6.31	5.81	3.53	1.04	0.43	0.41

From Figure 5.6 and Table 5.1, the total impedances of the treated mineral samples were higher than those of the untreated mineral samples. These phenomena are similar to the untreated and Si–Cat-treated pyrite, indicating that another product has grown on the electrode surface. It is suggested that this reflects the formation of a

silica–quinone layer on the surfaces of the treated sulfide mineral samples against oxidation.

5.4. Conclusions

The use of Si–Cat complex to suppress oxidation of other sulfide minerals was investigated. From analysis of the electrochemical behavior, theoretical evaluation, and microscopic observations

1. The Si–Cat complex can be used to suppress the oxidation of chalcopyrite, molybdenite, and arsenopyrite.
2. The electrochemical behavior showed that oxidative decomposition of the Si–Cat complex and formation of an encapsulating layer on the surface of treated sulfide mineral samples lowered the oxidation rate.
3. The microscopy results showed that the encapsulating layers on the treated sulfide mineral samples were silica-rich, and suggested that these layers were the same coating layer that formed on the pyrite surface after Si–Cat treatment.
4. The rates of oxidative decomposition of the Si–Cat complexes on the sulfide mineral surfaces are in the order chalcopyrite > molybdenite > arsenopyrite.
5. The Si–Cat complex had a better suppression effect for chalcopyrite than for molybdenite and arsenopyrite.

References

Bulatovic, M., 2007. Handbook of flotation reagents: chemistry, theory and practice: volume 1: flotation of sulfide ores, first ed. Elsevier Science, The Netherlands.

Jha, R.K.T., Satur, J., Hiroyoshi, N., Ito, M., Tsunekawa, M., 2008. Carrier-Microencapsulation using Si–catechol complex for suppressing pyrite floatability. Miner. Eng. 21, 889-893.

Jha, R.K.T., Satur, J., Hiroyoshi, N., Ito, M., Tsunekawa, M., 2012. Suppression of Pyrite Oxidation by Carrier Microencapsulation using Silicon and Catechol. Miner. Process. Extr. M. 33, 89-98.

Jorcin, J-B., Orazem M.E., Pébère, N., Tribollet, B., 2006. CPE analysis by local electrochemical impedance spectroscopy. Electrochim. Acta 51, 1473-1479. doi: doi:10.1016/j.electacta.2005.02.128

Liu, Y., Dang, Z., Lu, G., Wu, P., Feng, C., Yi, X., 2011. Utilization of electrochemical impedance spectroscopy for monitoring pyrite oxidation in the presence and absence of *Acidithiobacillus ferrooxidans*. Miner. Eng. 24, 833-838. doi:10.1016/j.mineng.2011.03.002

McLellan, B.C., Corder, G.D., 2012. Risk reduction through early assessment and integration of sustainability in design in the minerals industry. J. Clean. Prod. 53, 37–46. doi:10.1016/j.jclepro.2012.02.014

Memary, R., Giurco, D., Mudd, G., Mason, L., 2012. Life cycle assessment: a time series analysis of copper. J. Clean. Prod. 33, 97–108. doi:10.1016/j.jclepro.2012.04.025

Moors, E.H.M., Mulder, K.F., Vergragt, P.J., 2005. Towards cleaner production: barriers and strategies in the base metals producing industry. J. Clean. Prod. 13, 657–668. doi:10.1016/j.jclepro.2003.12.010

Sasaki, K., Tsunekawa, M., Ohtsuka, T., Konno, H., 1995. Confirmation of a sulfur-rich layer on pyrite after oxidative dissolution by Fe(III) ions around pH 2. Geochim. Cosmochim. Acta 59, 3155-3158. doi: 10.1016/0016-7037(95)00203-C

Satur, J., Hiroyoshi, N., Tsunekawa, M., Okamoto, H., 2007. Carrier-Microencapsulation for preventing pyrite oxidation. Int. J. Miner. Process. 83, 116-124.

Simate, G.S., Ndlovu, S., 2014. Acid mine drainage: Challenges and opportunities. J. Environ. Chem. Eng. 2, 1785-1803. doi:10.1016/j.jece.2014.07.021

CHAPTER 6

Conclusions and Recommendations

A comprehensive study has been conducted in this study. Several analytical methods were also applied to investigate the covering layer characteristic formed from Si-Cat complex. In this chapter, conclusions for this research are presented along with further study need to be conducted for future improvements.

6.1. Conclusions

Acid mine drainage (AMD) resulting from the oxidation of pyrite and other sulfide minerals has caused significant environmental problems, including the acidification of rivers and streams, and the leaching of toxic metals. The oxidation process has therefore been widely studied under various conditions to investigate effective approaches and controlling factors to inhibit the oxidation process. The process is complex because it involves chemical, biological, and electrochemical reactions, and varies with environmental conditions.

Several methods have been investigated for the treatment and abatement of AMD. The limited effectiveness of some controlling methods has led to further study of methods to inhibit pyrite oxidation. To successfully control and prevent AMD, clear and thorough understanding of the chemistry, mechanisms, and all reactants involved in AMD is important. It is known that oxygen, the water content, and iron-oxidizing bacteria have a significant effect on the pyrite oxidation rate. Reduction of any of these factors can contribute to a remarkable reduction of the oxidation rate. Passivation of sulfide minerals involving formation of a surface barrier through formation of a coating layer is a potential way to control AMD generation. In passivation, a thin organic or inorganic protective coating is formed on the surface of pyrite to prevent its contact with the atmosphere, water, and bacteria that promote oxidation.

One of the promising methods is carrier microencapsulation (CME) by using silicon–catechol complex. However, the details mechanism and the coating layer properties are not yet confirmed. Thus, further studies on pyrite oxidation suppression by using silicon-catechol complex are discussed in this study.

This thesis consists of six chapters. **Chapter 1** presents the background and objectives of this study. In addition, an overview of AMD and its prevention are presented to provide a basic understanding of pyrite oxidation suppression. Previous studies related to the present study are also discussed in this chapter. Pyrite oxidation suppression by CME with silicon (Si) and an organic carrier is presented in **Chapter 2**. It was found that waste water collected from hydrothermal treatment (HT) of low-rank coal contains organic carbon compounds, such as phenol and catechol. The use of HT liquid (HTL) produced from low-rank coal as a carrier in CME was investigated. In dissolution tests for 51 days with pyrite and iron-oxidizing bacteria, treatment with a mixture of HTL and a silicon reagent (Si–HTL) lowered the ferric ion concentration and limited bacterial attachment compared with untreated pyrite. These results indicate that pyrite oxidation can be suppressed simply by pretreating with Si–HTL for 1 h. This might be caused by catechol present in the HTL. A mixture of catechol and a silicon reagent (Si–Cat) was also used, and the coatings obtained using Si–HTL and Si–Cat were compared. Based on dissolution tests, the Si–HTL coating layer showed better barrier properties than the Si–Cat coating layer. Microscopic observations showed a silica-rich deposit on the surface of the treated pyrite. Fourier-transform infrared (FTIR) spectroscopy indicated that a quinone compound adsorbed on the treated pyrite surface. These results showed that silica and quinone were both adsorbed on the pyrite surface in a silica–quinone layer, which can suppress pyrite oxidation.

In addition to chapter 2, most of the protection effect of coatings on pyrite was evaluated by chemical method. Very little studies are available on the evaluation of coating layer on the pyrite surface with electrochemical methods. In **Chapter 3**,

three different electrochemical methods, namely, potential polarization, chronoamperometry, and electrochemical impedance spectroscopy (EIS), were used to investigate the electrochemical behavior of pyrite oxidation suppression in the presence of a silicate coating. Anodic current peaks corresponding to oxidative decomposition of the Si–Cat complex on the pyrite surface were observed at 550 mV in the presence of Si–Cat, and at 690 mV in the presence of Si–HTL. The anodic currents of the treated pyrite samples (Si–Cat pyrite and Si–HTL pyrite) were lower than that of the untreated pyrite. Because the anodic current represents the oxidation rate, the lower anodic currents of the treated pyrite samples mean that the oxidation rates of these treated samples are lower than that of the untreated pyrite. The two flat semi-circular curves in the Nyquist plots showed that the total impedances of the treated pyrite samples increased. It is suggested that this is a silica–quinone coating, which can decrease the pyrite oxidation rate. It also showed that the coating resistance produced by Si–HTL treatment is higher than that produced by Si–Cat. Bode plots showed the shift of the phase angle of the time constant of Si–Cat-treated pyrite to lower frequencies, indicating electrolyte diffusion occurs through the coating layer. This indicates that the coating layer produced by Si–HTL treatment has better barrier properties than that produced by Si–Cat and confirms the results of the dissolution tests and chronoamperometric measurements.

In order to support the findings in chapter 2 and 3, a more systematic investigation of the silica–quinone coating layer is presented in **Chapter 4**. Furthermore, the mechanism involved in this coating treatment is proposed. Pyrite treatment using Si–Cat under different conditions resulted in differences in the suppression of pyrite oxidation. The electrochemical behavior of treated pyrite

samples showed that Si–Cat treatment for 6 h with initial pH 9.5 gave better barrier properties and a higher suppression effect than that of other treatment conditions. FTIR and XPS analyses demonstrated that the coating layers on the treated pyrite samples consisted of a network of Fe–O–Si and Si–O–Si units on the pyrite surface. The Si–O–C asymmetric stretching mode is also present in the FTIR spectra. These results confirm that silicate polymerization in the silica–quinone layer on the treated pyrite samples suppressed pyrite oxidation.

The findings on pyrite oxidation suppression by the Si–Cat complex were applied to other sulfide mineral samples: chalcopyrite ($CuFeS_2$), molybdenite (MoS_2), and arsenopyrite (FeAsS). These are presented in **Chapter 5**. Effect of silicate covering layer on treated minerals surfaces were evaluated by potential polarization, chronoamperometry, EIS, and SEM-EDX. Similar to pyrite, the results indicate the formation of a coating layer on the treated sulfide mineral samples that lowered the oxidation rate. The Si–Cat complex showed a better suppression effect for chalcopyrite than for molybdenite and arsenopyrite.

6.2. Recommendations

Sulfide minerals microencapsulation by using Si–Cat complex is still in the laboratory scale, and has not been tested in the natural environment. Nevertheless, it represents sulfide minerals oxidation control and in some cases future improvements on the technology and its application may prove to be most effective in controlling long-term sulfide minerals oxidation. Moreover, the proposed carrier microencapsulation using Si-HTL is economical due to the utilization of wastewater product.

From the results obtained in this study, there are some works that will be beneficial to be conducted, as followed:

1. Although the passivation by using Si–Cat treatment are predicted to be very stable, no long term data are available to predict treatment lifetime. Further kinetic study on pyrite oxidation suppression by using Si–Cat complex need to be conducted.
2. The effect of Si–Cat concentration is also one of the important factors that will be conducted in the future to optimize the oxidation suppression effect.
3. Quality parameter of coating layer, such as layer thickness should be determined by an independent technique, i.e., ellipsometry analysis.

Acknowledgements

It gives me great pleasure in expressing my gratitude to all those people who have supported me and had their contributions in making this thesis possible.

Although only my name appears on the cover of this PhD thesis, a great many people have contributed and given their support in this challenging journey. To say "thank you" to all of you is not even enough to express my gratitude.

First and foremost, I would like to express my profound sense of reverence to my supervisor Prof. Tsuyoshi Hirajima, for his continuously guidance, support, motivation and untiring help during the course of my PhD. He has always been caring, a source of wisdom and motivation. It is my honor to be his student.

Besides my supervisor, I would like to thank Prof. Hiroaki Nakano from Department of Materials Science and Engineering, Kyushu University as part of my thesis committee for his encouragement and insightful comments.

I express my deepest gratitude to Prof. Keiko Sasaki and Assoc. Prof. Naoko Okibe for their supports and valuable discussions, as well as to be members of my thesis committee. I always find their comments, questions and suggestions in my research very challenging and I always felt very relaxed after answering their concerns.

I would like to thank Assistant Prof. Hajime Miki for helping and being available to guide me in all my research especially in electrochemistry. This research topic was quite new for me and I learnt from the very basic. Thank you so much for the challenging research that lies behind it.

My sincere thank also goes to the Assistant Prof. Moriyasu Nonaka. He has helped me greatly and been a source of knowledge with real world of research skills, specifically in analytical instruments.

I am also grateful to the Professors and lecturers at International Special Course on Environmental Systems Engineering (ISC) for teaching me on related topics that helped me to improve my knowledge in the area.

I am also greatly indebted to many teachers at Japanese Language Course (JLC) who taught me not only Japanese language, but also Japanese life, culture and many things that always made me interested in.

One person who has always been ready to help me was our secretary Makiko Semba. She took care of all non-scientific works, including official procedure of PhD. Thank you Semba-san for all your support!

I would like to especially thank Atsunori Tayaoka for teaching me about electrical things, for helping me to solve many problems and for the excellent discussions during my research.

It is my pleasure to acknowledge all laboratory members in Mineral Processing, Recycling and Environmental Remediation Laboratory. The list of names would take pages, nevertheless I feel the need to mention some names: Dr. Mohsen M. Farahat, Dr. Ahmed M. Elmahdy, Dr. Dewi Agustina Iryani, Dr. Limsy Pilasinee, Dr. XinHong Qiu, Widi Astuti, Wuhui Luo, Xiangchun Liu, Gde Pandhe Wisnu Suyantara, Keitaro Kitagawa, Yusei Masaki, Masanori Mori, Hisaya Tsuji, Masashi Maki, Osamu Ichikawa, Taichi Momoki, Mari Yoshida, Shiori Morishita, Masahito Tanaka, Akinobu Iguchi, Hidekazu Matsuoka, Kenta Toshiyuki, Yu Takaki, Yuken Fukano, Daisuke Nakayama, Keishi Oyama, Kazuyoshi Oka, and many others whose name is not mentioned here for their enormous support and providing a good atmosphere in the lab. Thank you for the laughter, cheerful, togetherness, and memories that gave to me in their own unique way. I have learnt a lot from all of them and I am very grateful about the fruitful time to have spent together. I thank for making life fun while working. And the most important is for becoming lifelong friends. It is a time to remember.

During my stay in Fukuoka, Sunday was usually the time I recharged myself by travelling around and taking many photos as my hobby. It is very important to have a nice social environment and involved in activities outside the lab. The city, Fukuoka, itself has taught me several good lessons and also has given me many good friends, not only Japanese but also foreigners. Thank you to the many people and organizations who let me in to the dozens of cultural events. Also in Fukuoka, very

rarely I have felt that I am staying away from my home. In this regard, I would like to thank all Indonesian students for creating a wonderful social platform in the name of PPIF (Indonesian Student Association in Fukuoka).

I am grateful to my office and college researches at Research Centre for Geotechnology-Indonesian Institute of Sciences (LIPI), who support, laid seeds of enthusiasm and passion in pursuit of knowledge. To my friends scattered around the country, thank you for your thoughts, well-wishes/prayers, phone calls, e-mails, texts, and being there whenever I needed a friend.

I acknowledge to the scholarship provided by the Ministry of Education, Culture, Sports, Science and Technology, Japan (MEXT) and also financial and other supports from a Grant-in-Aid for Scientific Research Nos. 24246149 and 15H02333 from Japan Society for the Promotion of Science (JSPS).

Last but not the least, I can't imagine my current position without the love and support from my family. A million thanks to my parents and sister. I strongly believe that their prayers played very important role in my life.

Fukuoka, September 2015

Mutia Dewi Yuniati